THE UNIVERSITY OF CHICAGO

DISTINGUISHING THE ROLE OF STRUCTURE, VIBRATIONAL DYNAMICS, AND COMPOSITION IN ELECTRON-PHONON COUPLING OF NB(100) SURFACES

A DISSERTATION SUBMITTED TO

THE FACULTY OF THE DIVISION OF THE PHYSICAL SCIENCES

IN CANDIDACY FOR THE DEGREE OF

DOCTOR OF PHILOSOPHY

DEPARTMENT OF CHEMISTRY

BY

CALEB JOSEPH THOMPSON

CHICAGO, ILLINOIS

AUGUST 2024

"He who is not bold enough to be stared at from across the abyss is not bold enough to stare into it himself." – Silent Hill 2

Table of Contents

List of Figures

List of Tables

Acknowledgments

Thank you to my parents Mike and Juanita Thompson who's love always overflows... I doubt I will ever be able to understand all you have given me.

Thank you to my dear friends Becky Burch, Jerran Miller, Josh Pearson, Moriah Schneider, and Devin Caplow who have been lifelong friends and partners... I do not know where or who I would be without you.

Thank you to Steve Sibener for investing in and backing me… in our long talks I felt challenged, intellectually stimulated, and enlightened by your wisdom and experience. Your fingerprints will be on my brain for the rest of my life and I am better off for it.

Thank to my mentors Jacob Graham, Rachel Farber, and Ali McMillan for enduring my questions, hearing out my fountain of ideas, and discussion about what a PhD means to each of you.

Thank you to my lab-partner Michael Van Duinen for trusting me, being self-motivated, and accommodating my melodrama… I'll be watching what you do next and cheering you on.

Thank you to Team Nb (Sarah Willson, Van Do, Michael Van Duinen) for our insightful discussions and comradery through collaboration.

Thank you to the Sibener Group for thinking that it's ok to be a scientist and have a life as well as providing a safe space of community.

Abstract

Niobium is the current material of choice for superconducting radiofrequency (SRF) cavities in particle accelerators. Nb found its ubiquitous use and extensive study in SRF cavities due to both its normal and superconducting state properties. Experimental and theoretical studies have documented and studied mechanisms in which even local hot spots from inhomogeneities, defects, and topographical variations can heat and quench entire SRF cavities. Thus, optimal preparation of Nb SRF cavity surfaces are required to prepare energetically efficient SRF cavities and keep costs of operation from being prohibitively high. In other words, the relationship between atomic-scale surface structure and the resulting superconducting properties at the surface is critical in improving and developing next generation SRF cavity materials. While well-studied, the formation and evolution of surface defects and compositional inhomogeneities remains a challenging part of SRF cavity treatment design and implementation. Such an understanding of the role of surface structure and chemical composition as well as their resulting effects on superconductivity at the surface remains elusive. This thesis seeks to make a start to this foundational understanding with *in situ* high temperature measurement of atomic scale surface structure, vibrational dynamics, and surface EPC on the metallic Nb(100) surface and its surface oxide reconstruction (3x1)-O/Nb(100).

These measurements begin with the discovery of the (3x1)-O/Nb(100)'s high temperature stability and structural/ compositional persistence under SRF cavity preparation conditions. Then, a key driving force for the unusual stability of the (3x1)-O/Nb(100) was elucidated with inelastic HAS TOF measurements and *ab initio* density-functional theory (DFT) calculations, revealing abnormally strong Nb-O and Nb-Nb bonds that make up the characteristic ladder

structure. This means the ladder crests of the (3x1)-O/Nb(100) not only introduces new, relatively strong Nb-O interactions, but it significantly strengthens the Nb-Nb interactions. In this way the (3x1)-O/Nb(100) passivates and stabilizes the surface. These results demonstrate the significant role niobium oxides play in the optimization of growth strategies and coating procedures for next–generation SRF materials.

Next the atomic-scale structure's effect on the superconductivity was investigated using HAS's sensitivity to EPC. HAS simultaneously measured the surface electron-phonon coupling (EPC, SEPC) constant (λ, λ_S) and *in situ* high temperature atomic-scale surface structure of the unreconstructed, metallic Nb(100) surface as well as the (3x1)-O/Nb(100) oxide reconstruction. *Ab initio* DFT with local averaging agrees well with the HAS data. Furthermore, some variations in subsurface C and O and their effect on the SEPC are discussed. The Nb(100) surface λ_S is 0.50 ± 0.08 while that of the (3x1)-O/Nb(100) surface oxide reconstruction is λ_S is 0.20 ± 0.06. The λ_S measured for the Nb(100) surface is ~1/2 the reported bulk Nb λ values. The significance of Nb(100)'s diminished EPC was elucidated by estimating relevant superconducting properties from the measured λ_S, surface Debye temperature, known material parameters, and well-established equations. These results indicate that the Nb(100) surface has decreased superconducting properties relative to the bulk. This study shows that these effects may be due also to the interface itself even without oxygen. Additionally, the λ_S measured for the (3×1)-O surface reconstruction is further diminished from the metallic, unreconstructed Nb(100) value and the reported bulk Nb λ values. Furthermore, varying subsurface O has no significant effect on the λ_S of the (3×1)-O reconstruction. While the metallic, unreconstructed Nb(100) surface is significantly affected by accumulated subsurface C and O, the (3×1)-O reconstruction stabilizes its λ_S against the effects of subsurface O. These results contain the first λ measured for the

metallic Nb(100), (3x1)-O/Nb(100), and any Nb surface. These measurements begin a fundamental understanding of atomic-scale surface structure's effect on EPC and superconductivity in Nb.

Chapter 1

Introduction

Interfaces and surfaces are ubiquitous. Where a phase ends or meets another there will be an interface.[1] In fact interfacial properties exhibit unique and critical chemical processes, such as many environmental reactions in our atmosphere, the Haber-Bosch process that feeds the modern world, adhesives, and the processing of fuels. In other words interfaces modify the properties of the bulk material in startling and fascinating ways. These can lead to altered reactivities, electronic properties, and reconstructions. This thesis reports surface science studies of niobium surfaces, elucidating the role of niobium surfaces in particle accelerators around the world. In our *in situ* ultra-high vacuum (UHV) scattering instrument, one may exert careful control over a material's surface and measure atomic scale structure, dynamics, and electron-phonon coupling. Such careful fundamental research provides a foundational understanding of niobium surfaces for their applications and technological developments.

The niobium surface in a particle accelerator is a solid-gas interface. In order to study the surface one must isolate the solid surface from unwanted gases. Surface scientists do this with a vacuum. Additionally this vacuum allows probes to reach the surface, interact with it, and leave without contaminating the surface by ambient gas particles. Such techniques include low-energy electron diffraction (LEED), Auger Electron Spectroscopy (AES), scanning tunneling microscopy (STM), and atomic force microscopy (AFM).[2] Scattering techniques had been developed for both bulk and surface; however atomic or molecular scattering probes did not come about until crossed-beam experiments.[3,4] In crossed-beam experiments, multiple supersonic beams of chosen atoms or molecules were crossed allowing unique control over

reaction dynamics. This was transferred to surfaces where helium atoms became the probe of choice due to helium atoms being neutral, non-destructive, strictly surface sensitive, and well matched range of energies and wavelengths.[2,5]

Niobium found its ubiquitous use and extensive study in SRF cavities due to both its normal and superconducting state properties.[6] Experimental and theoretical studies have documented and studied mechanisms in which even local hot spots from inhomogeneities, defects, and topographical variations can heat and quench entire SRF cavities.[7] Thus, optimal preparation of niobium SRF cavity surfaces is required to prepare energetically efficient SRF cavities and keep costs of operation from being prohibitively high[6]. This thesis seeks to make a start to this foundational understanding with *in situ* high temperature measurement of atomic scale surface structure, vibrational dynamics, and surface EPC on the metallic Nb(100) surface and its surface oxide reconstruction (3x1)-O/Nb(100).

Chapter 2 covers the necessary theoretical background and experimental methods necessary to use the scattering instrument and perform necessary analysis. This includes a brief description of crystal theory, electrons, phonons, electron-phonon coupling, and atomic beam scattering. The instrument used in this thesis is described in full detail as well as the resulting data analysis, crystal preparation, and typical experimental parameters.

In **Chapter 3** the high temperature stability of the (3x1)-O/ Nb(100) surface oxide reconstruction is reported with *in situ* high temperature HAS diffraction and AES. The (3x1)-O/ Nb(100) surface oxide reconstruction is stable up to 1130 K in terms of the surface structure, order, and composition. This revealed the state of oxidized Nb surfaces under SRF cavity preparation conditions, enabling new SRF cavity materials and treatments.

In **Chapter 4** the (3x1)-O/ Nb(100)'s stability was investigated with inelastic HAS time-of-flight (TOF) measurements and *ab initio* DFT calculations. HAS's capability to map surface phonon dispersions allowed rigorous comparison with theory through mean-squared-displacements and phonon dispersion curves. The synergy of experiment and theory identified the ladder crests of the (3x1)-O/ Nb(100) as introducing abnormally strong Nb-O interactions and significantly strengthening the Nb-Nb interactions. This has leverage HAS to identify the specific atomic-scale surface structure with its effect on (3x1)-O/ Nb(100)'s stability, suggesting the ladder crests as barriers to SRF cavity treatments.

Next, in **Chapter 5** the metallic, unreconstructed Nb(100)'s atomic-scale structure and its effect on superconductivity was investigated using HAS's sensitivity to EPC and *ab initio* DFT calculations There is excellent agreement between HAS data and *ab initio* DFT theory. This study revealed the EPC of the metallic Nb(100) surface (0.50 ± 0.08) is more than halved relative to that of the bulk (~1). The impact of this significant diminishing of EPC by the metallic Nb(100) interface is elucidated by estimating benchmark superconducting properties with established equations. Additionally, accumulating subsurface C and O impurities further diminishes EPC of the metallic Nb(100) surface.

Following the EPC study of the metallic Nb(100) surface the effects of the (3x1)-O/ Nb(100) on EPC was investigated and is reported in **Chapter 6**. Similarly there is excellent agreement between HAS data and *ab initio* DFT calculations, determining the EPC of the (3x1)-O/Nb(100) surface oxide reconstruction's EPC (0.20 ± 0.06). This revealed that the (3×1)-O surface reconstruction further diminishes EPC from the metallic, unreconstructed Nb(100) value and the reported bulk Nb λ values. Furthermore, the results showed that varying subsurface O has no significant effect on the λ_S of the (3×1)-O reconstruction unlike the metallic surface.

These results contain the first λ measured for the metallic Nb(100), (3x1)-O/Nb(100), and any Nb surface. These measurements begin a fundamental understanding of atomic-scale surface structure's effect on EPC and superconductivity in Nb.

Chapter 2

Theoretical Background and Experimental Methods

Helium atom scattering (HAS) utilizes fundamental surface science, gas-surface scattering theory, and ultra-high vacuum (UHV) techniques to measure surface structure, dynamics, and electron-phonon coupling.[2] This chapter reviews essential concepts, describes the scattering apparatus, and explains data analysis techniques. The review begins with crystalline surfaces and reciprocal lattices then establishes a necessary foundation in electrons, phonons, and electron-phonon coupling. Next, the necessity of supersonic beams and relevant HAS measurements – elastic diffraction, inelastic time of flight, thermal attenuation of specular intensity – are covered. After HAS is covered, superconductivity and niobium superconducting radio frequency cavities will be introduced and connected to HAS measurables. Before covering data analysis, the UHV scattering instrument and its three primary sections – beamline, scattering chamber, and rotatable detector – are described and explained with scattering theory equations.

2.1 Crystal Lattice, Reciprocal Lattice

Crystals are solids with periodic structure. This periodic structure is called a lattice. A lattice is composed of repeating unit, the unit cell.[8] The unit cell is described by a collection of unit cell vectors. From a defined origin, each point $\vec{r}$ in the crystal is the same as the point,

$$\vec{r}' = \vec{r} + n_1 \cdot \vec{a} + n_2 \cdot \vec{b} + n_3 \cdot \vec{c}, \tag{2.1}$$

where n_1, n_2, and n_3 are integers and ($\vec{a}$, $\vec{b}$, $\vec{c}$) are unit cell vectors.[8] However, the lattice can be described by reciprocal lattice vectors, giving the lattice in reciprocal space.[8] The surface generated from terminating this lattice with a planar cut is described with Miller indices of the

plane.[9] When referring to a surface the unit cell becomes two dimensional and is described by only two unit cell vectors:[8]

$$\vec{r}' = \vec{r} + n_1 \cdot \vec{a} + n_2 \cdot \vec{b}. \tag{2.2}$$

There is a plethora of crystal and surface lattices, however this thesis is focused on the body-centered cubic (BCC) structure of Nb and it's Nb(100) surface.[9] For BCC, $|\vec{a}| = |\vec{b}|$ and the angle between the two vectors is $\gamma = 90°$.[8,9]

Another useful description of lattices is the reciprocal lattice. For a surface, the reciprocal lattice also two dimensional. Thus, the surface reciprocal lattice vectors $\vec{a}^*$ and b^* are defined in terms of the surface real-space lattice vectors, $\vec{a}$ and $\vec{b}$, as

$$\vec{a}^* = 2\pi \frac{\vec{b}\times\vec{n}}{\vec{a}\cdot(\vec{b}\times\vec{n})},\ \vec{b}^* = 2\pi \frac{\vec{n}\times\vec{a}}{\vec{a}\cdot(\vec{b}\times\vec{n})}, \tag{2.3}$$

where $\vec{n}$ is the surface-normal unit vector.[4] Any point in the reciprocal lattice, maybe described by a translation vector

$$\vec{G}_{hk} = h\vec{a}^* + k\vec{b}^*, \tag{2.4}$$

where *h* and k are integers know as Miller indices.[3] Within HAS diffraction peaks are labeled with Miller indices. While the physical significance of the real space lattice vectors is self-apparent, that of the reciprocal lattice is not. While being literally "inverted space" the reciprocal lattice vector also is analogous to a wavevector of a wave.[8] Wavevector directly gives the momentum of a wave, meaning that reciprocal space is also momentum space. This is useful when considering how waves move through the lattice, specifically electrons and phonons.[10] Plotting the energy of electrons and phonons throughout the reciprocal lattice yields many significant insights into material and transport properties.[8] Furthermore, at the surface the lattice is terminated, leaving a surface that may reconstruct to relieve any produced stress.[2] This can

cause lattice compression or expansion as well as entire surface lattice reconstructions.[2] In this way the surface often modifies the lattice, electronic states, phonon states, electron-phonon coupling, and many other material properties.[2,5]

Within the reciprocal lattice, the periodic nature of the reciprocal lattice unit cell means that it's behavior repeats when starting at a reciprocal lattice point and traveling beyond the reciprocal lattice unit cell.[8] These repeating zones are called Brillouin zones (BZ), where the first BZ is an area or volume that is closest to a single reciprocal lattice point.[8,9] This area or volume can be drawn with a simple procedure. Pick your single reciprocal lattice point, draw lines between between the chosen reciprocal lattice point and each of its nearest neighbor reciprocal lattice points, bisect these lines in half with perpendicular lines, and then color in the contained region. The colored region will be the first BZ. Often it is said that the behavior across the first, second, third, etc. BZ is "folded" into the first BZ. Doing so rigorously and mathematically allows one to completely describe the reciprocal space within the first BZ.[8] Various conventions have arose labeling key, high-symmetry points in the first BZ. Specifically, the center of the first surface BZ is labeled as $\bar{\Gamma}$, with other high symmetry points labeled as $\bar{X}$, $\bar{M}$ ect. In Bulk BZ there is a similar notation without the bars[8]. In this way people plot certain paths between these high symmetry points, such as $\overline{\Gamma X}$, $\overline{\Gamma M}$, ect.[2] We will see later that diffraction peaks only occur when the change in wavevector of the helium is equal to that of a reciprocal lattice vector. This means that the diffracted helium is plotted in reciprocal space along these high-symmetry paths while its peaks are reciprocal lattice points[8,11]. This means the conversion between the diffraction peak location in units of change in surface parallel wave vector, $\Delta\vec{K}$, and the real-space distance, a, is[9]

$$a = \frac{2\pi}{\Delta\vec{K}}. \tag{2.5}$$

2.2 Electrons, Phonons, and Electron-Phonon Coupling

In dealing with phonons and electron-phonon coupling (EPC) the content of this thesis touches upon electrons. However, in all cases the free electron model is applied. Thus, a relevant introduction to this topic covers the free electron model. In the free electron model all electron-electron interactions are neglected.[8] Thus, when considering free electrons in a crystal of some arbitrary volume, *V*, of a cube with sides of length, *L*, the problem can be framed as a particle in a box problem. This results in the typical eigenvalue problem with a kinetic energy operator.[8] This along with invoking Bloch wave for the wave functions in a periodic potential (crystal lattice) or invoking periodic boundary conditions at the edges of the volume, results in the following expressions for free electron wave function, ψ_k, energy, *E*; momentum, *p*; velocity, *v*; and DeBroglie wavelength, λ_{DB}, in terms of the electron wavevector, *k*,[8]

$$\psi_k(r) = \frac{1}{\sqrt{V}} e^{ikr}, \tag{2.6}$$

$$E = \frac{\hbar^2 k^2}{2m}, \tag{2.7}$$

$$p = \hbar k, \tag{2.8}$$

$$v = \frac{\hbar k}{m}, \tag{2.9}$$

$$\lambda_{DB} = \frac{2\pi}{k}. \tag{2.10}$$

Now we will use the previously mentioned, periodic boundary conditions, and the wave function, ψ_k to define the allowed values for and components of the wavevector. By invoking the periodic boundary condition

$$e^{ik_x L} = e^{ik_y L} = e^{ik_z L} = 1, \tag{2.11}$$

and noting that e^z = 1 only if $z = 2\pi i n$ (where n is an integer), it becomes apparent that the components of the wave vectors must satisfy:[8]

$$k_x = \frac{2\pi n_x}{L}, k_y = \frac{2\pi n_y}{L}, k_z = \frac{2\pi n_z}{L}, \tag{2.12}$$

where n_x, n_y, and $n_z$are integers. Defining these are useful, allowing one to also define the k-space density of levels which in turn helps define the Fermi surface, and the number of conduction electrons. First, upon examining the requirements on the allowed wavevector components, one sees that there is a k-space volume, $V/8\pi^3$, associated with each allowed k-value.[8,9] Thus one may define some arbitrary k-space volume, Ω, so that it will have $\Omega V/8\pi^3$ allowed k-values within it. Now we will consider placing electrons into the states corresponding to these allowed k-values. We know from the Pauli exclusion principle and the two electrons allowed in each state due to spin, that there will be two electrons per allow k-value. As one places N electrons in the lowest available state available, one would assemble a collection of occupied k-space values that would occupy some k-space volume, called the Fermi sphere.[8] It is well approximated by a sphere since the energy of an electron has already been shown to be directly proportional to the square of its wavevector. Substituting the Fermi sphere in for the arbitrary volume, Ω, one obtains $\Omega = 4\pi k_f^3/3$, where k_f is the radius of the Fermi sphere in k-space and defined as the Fermi wavevector.[8] Allowing one to calculate the number of free electrons per unit volume, *N*, occupying the allow k-values in the Fermi sphere as[8]

$$N = \frac{2}{V}\left(\frac{4\pi k_f^3}{3}\right)\left(\frac{V}{8\pi^3}\right) = \frac{k_f^3}{3\pi^2}. \tag{2.13}$$

Similarly there are definitions for Fermi energy, Fermi momentum, and Fermi velocity where the value for *k* is replaced with k_f in equations 2.6 – 2.10.[8]

Phonons are defined in analogy to photons but are effectively normal modes of a crystal lattice.[2,8,12] For a 3D crystal with N atoms there are 3N phonon modes.[8] From writing expressions for the total force exerted on atoms in the lattice, we obtain mass balance equations by writing out the force exerted on each atom in terms of derivatives of the chosen

potential.[2,5,8,12] These equations form a series of equations that can be described within a single linear algebra equation that is an eigenvalue problem. Upon examination of the eigenvalue problem, useful matrices can be defined such as the force constant matrix and the dynamical matrix.[8] The force constant matrix elements are the sum of the second derivative of the potential between atoms and the dynamical matrix is the Fourier transform of the force constant matrix.[2,8] The dynamical matrix becomes the key to solving the eigenvalue problem, obtaining the phonon dispersions (eigenvalues) and their displacement vectors (eigenvectors).[5,8,12] Thus, diagonalizing the dynamical matrix gives the phonon dispersions and phonon displacement vectors, while its elements contain the interatomic forces.[2,12] Phonon mode displacements can be along the direction of travel or perpendicular to it, being categorized as longitudinal and transverse phonons respectively.[8,9] However often phonon modes have elliptical phonon displacements that have both longitudinal and transverse components.[2] Furthermore, the displacements of neighboring atoms can be in-phase or out-of-phase with each other yielding acoustic or optical phonon modes respectively.[8,9] Acoustic modes are sound waves and typically lower in energy, while optical phonon modes often induce a dipole, making them interact with photons and are typically higher in energy.[2,12]

These explanations have been general and apply to phonons in bulk crystals. However, as previously established phonons at or near a surface are modified.[2,12] Surfaces exhibit surface waves that only occur at the surface and bulk phonon modes that induce appreciable displacements at the surface.[2,5,12] Early on Lord Reyleigh documented acoustic waves propagating along a surface with displacements perpendicular to the surface.[2] Whether it's a wave in an ocean or land this term, Reyleigh Wave, emerged to describe acoustic waves propagating along the surface with transverse polarization perpendicular to the surface.[2] In fact,

within inelastic HAS theory the helium atoms couple to phonon modes via primarily surface perpendicular displacements.[2,5] Furthermore, the kinetic energy of helium atoms is most resonant with low energy phonon modes.[2,4] Thus, inelastic HAS most often excites or annihilates acoustic surface modes with transverse displacements perpendicular to the surface, specifically most of all Reyleigh waves.[2] However bulk phonons that occur close enough to the surface to induce appreciable displacements at the surface are called surface resonances.[2,5] In projecting a three-dimensional phonon mode dispersion onto a two-dimensional surface, a surface resonance band is generated.[2,12] One must consider the effects of compressing a three-dimensional phonon dispersion on a two-dimensional reciprocal lattice of the surface. The axis perpendicular to the surface is compressed resulting in a phonon dispersion band instead of a curve. The surface exclusive phonon mode dispersions can lie below or inside these surface resonance phonon bands.[3]

The electron–phonon coupling (EPC) constant (λ) is a dimensionless constant that quantifies the effective strength of electron–phonon interactions in a material.[10] It has various definitions,[2,13]

$$\lambda = \sum_{q,v} \lambda_{q,v} = 2 \int \frac{\alpha^2 F(\omega)}{\omega} d\omega \tag{2.14}$$

where q is the wavevector of a particular mode v, $\lambda_{q,v}$ is the electron-phonon interaction of mode v with wavevector q, and $\alpha^2 F(\omega)$ is known as the spectral function. The spectral function describes the probability that a particle with momentum k has a specific frequency, ω.[8] The first definition of EPC constant in equation 2.14 is used by the theory that extracted EPC constants from HAS data.[14,15] When referring to EPC definition, the first definition with the sum is the one this thesis is referring too. The EPC of a conventional superconductor like niobium causes the superconducting state to form. In fact the λ of a material has been related to superconducting

material properties such as critical temperature, superheating field, and superconducting gap.[6,16] These superconducting material properties are discussed by SRF cavity scientists in literature, allowing discourse on the potential effectiveness of new SRF cavity materials.[17] This means that EPC constants allows one to estimate important benchmark superconducting properties. This will be explored and use in more depth in chapters 5 and 6.

2.3 Supersonic Beams

Supersonic beams allow one to generate a well collimated beam with a low energy resolution relative to effusive beams with a Maxwell Boltzmann distribution.[3,18] To generate a supersonic beam, one must generate a specific type of gas expansion out of the beam nozzle into a sufficiently low-pressure region.[3] In fact, for this expansion to occur the mean free path of the particles inside the nozzle must be significantly less than the beam hole diameter.[18] This causes the number of collisions between particles to be near infinite as the gas expands through the nozzle, generating a reversible, adiabatic expansion.[18] This causes the sum of kinetic energy and total entropy of the gas.[3,18] In other words, in an ideal supersonic expansion all entropy is converted into directed kinetic energy, causing random kinetic energy of the gas inside the nozzle to be directed, narrowing the velocity spread along the beam and diminishing the average transverse velocity. Since He is monoatomic, it's well approximated as an ideal gas with a constant heat capacity ratio $\gamma = C_p/C_v$, where C_p and C_v are the specific heat capacities at constant pressure and volume, respectively (γ = 5/3 for He).[18] In this adiabatic expansion the sum of the beam's enthalpy and kinetic energy along the beamline is conserved, limiting the beam velocity (v_{max}) and kinetic energy (E_B) to[3]

$$v_{max} = \sqrt{\frac{2k_B T_0}{m}\left(\frac{\gamma}{\gamma-1}\right)} \text{ and } E_B = \left(\frac{\gamma}{\gamma-1}\right) k_B T_0, \tag{2.15}$$

where m is the mass of a He atom, k_B is Boltzmann's constant, and T_0 is the nozzle stagnation temperature. The Mach number, M, of a gas is the ratio of the average speed of the expanding gas, v, to the local speed of sound of the gas, v_b. Using ideal gas approximation and assuming an internal beam temperature of T, M can be written as[3,18]

$$M = \frac{v}{v_b} = \sqrt{\frac{mv^2}{\gamma k_B T}}. \tag{2.16}$$

As M increases, T decreases and narrows the internal velocity distribution. This is the conversion of random kinetic energy to a directed kinetic energy. The beam becomes supersonic when $M > 1$; this requirement written in terms of the chamber and backing pressure is[18]

$$\frac{P_0}{P_b} \geq \left[\frac{1}{2}(\gamma + 1)\right]^{\frac{\gamma}{\gamma - 1}}. \tag{2.17}$$

A higher the Mach number means a beam narrower in velocity and close to complete conversion of enthalpy to kinetic energy as described in equation 2.7. As this gas expands into the low-pressure region, the number of collisions decreases until there are effectively no collisions, reaching free molecular flow.[18] This section of free molecular flow within the supersonic expansion is called the zone of silence. It is called this because when there are no atomic collisions, sound waves cannot propagate, and the speed of sound is 0. Eventually this zone of silence reaches a shock wave formed when the expanding gas collides with the background gasses in the low-pressure region.[3,18] Here the conversion of random kinetic energy to directed kinetic energy is scrambled producing a Maxwell-Boltzmann distribution. However, the supersonic beam is extracted from the zone of silence by inserting a μm-sized skimmer through the shock wave, allowing a small portion of the zone of silence to proceed past the shock wave and into a second chamber without the directed kinetic energy being scrambled by a shock

wave.[3,18] Thus, these collimated beams with a narrow velocity spread extracted from the zone of silence with a skimmer are called a supersonic beam.

It is useful to define the energy and De Broglie wavelength of a beam traveling with momentum p, mass m, velocity v, and energy E may be treated as a wave, with wavelength, λ,

$$\lambda = \frac{h}{p} = \frac{h}{mv} = \frac{h}{\sqrt{2mE}}, \tag{2.18}$$

where h is Planck's constant.[3,18] Additionally, the wavevector, $\vec{k}_i$, of a beam is related to its wavelength via $k_i = 2\pi/\lambda$. Now, using the beam energy after expansion (Equation 2.7) with T_N representing beam temperature, the incident energy, E_i, and velocity, v, of a beam may be written as:[3]

$$E_i = \frac{1}{2}mv^2 = \frac{\hbar^2}{2m}k_i^2 = \frac{5}{2}k_B T_N; \tag{2.19}$$

$$v = \sqrt{\frac{5k_B T_N}{m}}. \tag{2.20}$$

2.4 Helium Atom Scattering

Helium atom scattering (HAS) has been utilized since 1930 when Estermann and Stern reported the first helium atom diffraction from NaCl and LiF surfaces.[3,19] Supersonic helium beams are suited to study surfaces due to their lack of penetration into the bulk, chemical inertness, and remarkably narrow velocity distributions.[2,3,5] As the helium atom is repelled by the electron density at metal surfaces, its turning point is on the order of 3 Angstroms.[2,20] The de Broglie wavelength and narrow momentum distribution of Helium atoms allow for precise measurements of the atomic-scale structure.[5,21] Furthermore, the momentum and energy of helium atoms are well-matched to those of surface phonons, giving HAS a unique ability to measure and resolve low-energy phonon modes.[2,5,12] Recently, the role of surface electron-phonon coupling (SEPC) in the helium-surface scattering event has been elucidated and

theoretically described for single phonon modes and thermally excited phonons in the high-temperature limit of many types of surfaces.[22] These developments in HAS theory add a new capability to measure and study SEPC.

2.4.1 Elastic Diffraction and Surface Structure

Upon impulsively scattering from a surface, a supersonic helium beam has sufficient wave-particle duality that it diffracts from atomic-scale periodic structures as a photon would from a diffraction grating.[5,21] However, upon impulsively scattering from a surface, a supersonic helium beam may elastically or inelastically scatter.[2] In inelastic scattering, the helium beam exchanges its kinetic energy with the surface, while in elastic scattering it does not.[23] This section will focus on the measurables, data analysis, and interpretation of elastically scattered helium. To this end, let us define the convention surrounding scattering event variables in Figure 2.1.

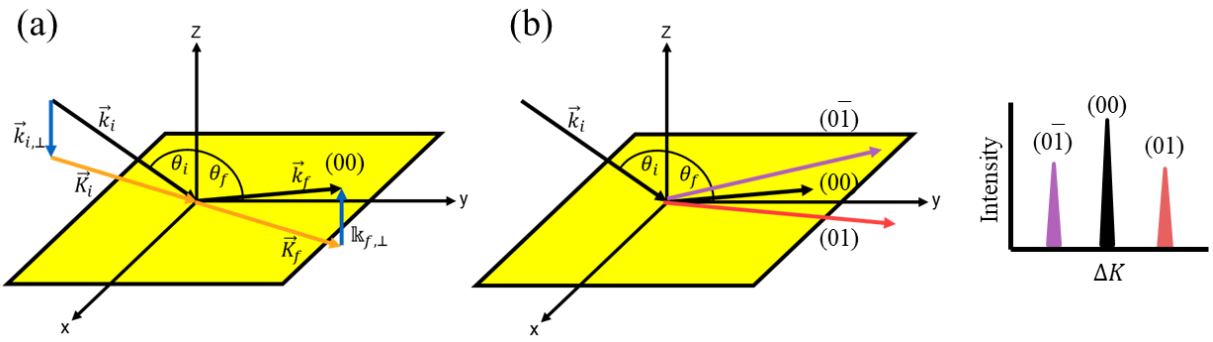

Figure 2.1: Schematic detailing the scattering geometry, vector components, and angle labels. The scattering wavevector components in (a) are define with the capital *K* indicating surface parallel components. In (b) the relative angles of a set of arbitrary forward (red, 01) and backward (purple, $0\bar{1}$) diffraction peaks relative to specular (black, 00).

Upon elastic diffraction a helium wave packet will exhibit quantum mechanical uncertainty.[5,11,21] In other words, the possible scattering pathways will interfere with one another,

producing a wave interference pattern via constructive and destructive interference. The condition at which diffraction peaks are evident can be deduced from the surface's lattice. This relationship is known as, the Von Laue's diffraction requirement.[8] Von Laue's diffraction requirement connects the change in momentum of scattered helium to the reciprocal lattice of the surface.[8] Consider a helium wave packet scattering from a surface (Fig. 2.1). We can use the fact that constructive interference occurs when the path difference of scattering atoms is an integral multiple of the beam wavelength.[9] We can also use the fact that this path difference is a real-space lattice vector of the surface. This means that diffraction peaks occur at angles in a diffraction for changes in the scattered helium's surface parallel wavevector that are equal to reciprocal lattice vectors at the surface.[8] This means that for every diffraction peak there is a corresponding periodic structure on the surface and the change in momentum of the helium atom of the diffraction peak is equal to the reciprocal distance of that periodic structure.[11,21] The diffraction peak momentum can be converted into the real space lattice distance, a, with[1–4]

$$a = \frac{2\pi}{\Delta K_{hk}}. \tag{2.21}$$

Thus, elastic diffraction measures the surface structure from the change in momentum of elastically diffracted helium. Additionally, with similar reasoning, varying the surface perpendicular component of the beam's wave vector, vertical steps between terraces and vicinal surface steps are determined as well.[3]

Beyond diffraction peak location there is much information within a diffraction scan. The full-width-half-max of the specular reflection gives – within good approximation – the domain size of the surface, quantifying surface order.[3,24] Furthermore, the width of diffraction peaks also indicates the relative order of that periodic structure.[11] In fact, even the intensity of the diffraction peaks gives electronic corrugation at the surface.[21] If the specular peak is ~50 times

larger than the diffraction peak the electron density at the surface is relatively flat indicating a metallic surface. Additionally large diffraction peaks relative to the specular reflection indicates large electronic corrugation and a nonmetallic surface. Random distributed defects will produce a diffuse scattering background that will increase as the quantity of random defects increase.[11]

In an elastic scattering event, the incident and final energies of the beam are equal: $E_i = E_f$. Assuming a crystalline surface, the Von Laue diffraction requirement states the change in momentum between the final, $\vec{k}_f$, and incident, $\vec{k}_i$, beams must equal a reciprocal lattice vector, $\vec{g}$:[3,8,9,21]

$$\Delta\vec{k} = \vec{g} \Rightarrow \vec{k}_f = \vec{k}_i + \vec{g}. \tag{2.22}$$

Convention defines the surface as the $x-y$ plane with surface normal along the z-axis. Wavevector components parallel to the surface are labeled with capital letters, e.g. $\vec{k}_i = (\vec{K}_i, k_{iz})$. In-plane diffraction, where the beam diffracts in-plane (defined by the z-axis and the incident wavevector), is illustrated in Figure 2.2. The Von Laue diffraction requirement for in-plane diffraction becomes:[5]

$$\Delta\vec{K} = \vec{K}_f - \vec{K}_i = \vec{G}_{hk}, \tag{2.23}$$

where $\vec{G}_{hk}$ is the sum of reciprocal surface lattice vectors with Miller indices h and k, as in Equation 2.4. Using the angles and wavevector components defined in Figure 2.2(a), the parallel momentum transfer ΔK can be written:[3,4,21]

$$\Delta K = K_f - K_i = k_i\big(\sin\theta_f - \sin\theta_i\big) = G_{hk}. \tag{2.24}$$

Helium diffraction peaks occur when Von Laue diffraction requirement is satisfied, and peaks are labeled with the Miller indices corresponding to their respective reciprocal surface lattice vectors, (hk). Using the known total flight path from the chopper to the post-collisional detector,

L_{CD}, elastic travel time t_0, and beam temperature T_N, Equations 2.11 and 2.12 can be rearranged to determine the incident wavevector of a beam:[4]

$$k_i = \frac{mL_{CD}}{\hbar t_0}; \tag{2.25}$$

$$t_0 = \sqrt{\frac{mL_{CD}^2}{5k_B T_N}}. \tag{2.26}$$

HAS is very sensitive to surface disorder, and indeed the specular peak, where $\theta_i = \theta_f$, can be used to determine the average domain size of a particular crystal.[25] The domain size broadening, $\Delta\theta_w$, is a convolution of the measured full-width-half-maximum (FWHM) of the specular peak, $\Delta\theta_{exp}$, and the instrument function broadening, $\Delta\theta_{inst}$:

$$\Delta\theta_w^2 = \Delta\theta_{exp}^2 - \Delta\theta_{inst}^2. \tag{2.27}$$

The crystal's coherence length, l_c, or average domain size, can be found through $\Delta\theta_w$ according to the relation[24,25]

$$l_c = \frac{5.54}{\Delta\theta_w k_i \cos\theta_f}. \tag{2.28}$$

These capabilities make HAS elastic diffraction an exceptional tool to study surface's atomic scale structure, surface order, defect type and amount, and electronic corrugation. Furthermore, it has been utilized to document changes in surface structure, making elastic diffraction uniquely suited to study both surface structure and dynamics.

2.4.2 Inelastic Time-of-Flight and Phonons

When a helium beam impulsively scatters from a surface it can alternatively exchange energy with the surface.[23] Since a helium atom it has no rotational or vibrational degrees of freedom, and its electronic states are far too large, its energy exchange with the surface is

entirely from or to the helium atoms' kinetic energy.[4,23] In other words, the helium atom's energy exchange with the surface can be completely tracked via the helium atoms changes in kinetic energy. The helium atoms kinetic energy and their change in kinetic energy can be measured with time-of-flight measurements.[4,23] For the surface, energy goes to and from the phonon states at or near enough the surface.[12,23]

Within a time-of-flight there is an elastic peak and then peaks that correspond to creation and annihilation of phonons at or near enough to the surface. For a single phonon inelastic HAS event and the conservation of energy becomes:[23]

$$\Delta E = E_f - E_i = \hbar\omega, \tag{2.29}$$

where E_f and E_i are the helium beam's final and initial energies, respectively, and $\hbar\omega$ is the phonon energy with frequency ω. By using Equation 2.11, this becomes

$$\Delta E = \frac{\hbar^2}{2m}k_f^2 - \frac{\hbar^2}{2m}k_i^2 = \hbar\omega. \tag{2.30}$$

Since inelastic scattering alters the helium energy, $k_i \neq k_f$, so the parallel momentum exchange in Equation 2.15 becomes:

$$\Delta K = K_f - K_i = k_f \sin\theta_f - k_i \sin\theta_i = G_{hk} + Q, \tag{2.32}$$

where Q is the wavevector for the created or annihilated phonon.

In fact, from energy and momentum conservation (equations 2.21 and 2.22), a helium scan curve can be derived,[4,23]

$$\Delta E = \frac{\hbar^2}{2m}\left[\frac{(k_i \sin\theta_i + \Delta K)^2}{\sin^2\theta_f} - k_i^2\right], \tag{2.33}$$

which describes all energy and momentum conservation allowed scattering pathways that can reach the detector for a given set of He scattering conditions. This scan curve can be plotted on a suspected phonon dispersion band structure. For some set of scattering conditions where the

helium scan curve intersects the true phonon dispersion curve of the surface will yield a time-of-flight peak.

Once one has a single phonon inelastic TOF peak, one can use the simple definition of speed and the scattered intensity per unit of flight time to obtain the phonon energy and wavevector. The speed, v, of a particle can be calculated by the distance traveled, L, and the travel time, t, while it's kinetic energy, E, can be written in terms of its speed:[4]

$$v = \frac{L}{t} \text{ and } E = \frac{1}{2}mv^2. \tag{2.34}$$

In an inelastic scattering event, the speed of the beam changes upon scattering from the surface. The speed of the beam before scattering is defined by the time, t_{CS}, the particle takes to travel the distance L_{CS} from the chopper to the sample, while the speed after scattering is defined by the time, t_{SD}, the particle takes to travel the distance, L_{SD}, from the sample to the detector. The measured TOF peaks for of elastically and inelastically scattering events are made distinct by differing arrival times, t_{SD}. The flight time of an elastic TOF peak, t_0, readily gives the initial energy, allowing for simple kinematics to obtain:[4]

$$t_{SD} = t_{CD} - \frac{L_{CS}}{L_{CD}}t_0. \tag{2.35}$$

The inelastic TOF peak location, and hence the energy of the created or annihilated phonon, is found by using Equations 2.20, 2.24, and 2.25, where $t_{obs} = t_{SD}$. Note that, since t_{CS} is always the same for both the elastic and inelastic scattering events, the energy of the phonon is given by:[4]

$$\hbar\omega = \Delta E = E_f - E_i = \frac{1}{2}\left(v_f^2 - v_i^2\right) = \frac{1}{2}m\left[\frac{L_{SD}^2}{\left(t_{obs} - \frac{L_{CS}}{L_{CD}}t_0\right)^2} - \frac{L_{CD}^2}{t_0^2}\right], \tag{2.36}$$

and the momentum of the phonon can be found using Equation 2.22, where

$$k_f = \frac{mL_{SD}}{\hbar\left(t_{obs} - \frac{L_{CS}}{L_{CD}}t_0\right)}. \tag{2.37}$$

In manipulating TOF spectra, one often converts the spectra from time into velocity and kinetic energy. In order to convert the TOF that records intensity as a function of time one must consider the nonlinearity of kinetic energy. This nonlinearly means the relative amplitudes of inelastic peaks change significantly upon conversion, while the area under a given peak is kept constant. The Jacobian of the transformation accounts for the scaling from this nonlinear relationship. The intensities measured by the TOF is $f(t_{obs})$ and the distribution as a function of change in energy is $f(\Delta E)$, then the number of particles at the detector, dN—the area under the curve—is conserved, and[4]

$$dN = f(t_{obs})dt_{obs} = f(\Delta E)d(\Delta E). \tag{2.38}$$

Since

$$dv = -\frac{L_{SD}}{t_{obs}^2}dt_{obs}, \tag{2.39}$$

then

$$d(\Delta E) = mvdv = m\frac{L_{SD}^2}{t_{obs}^3}dt_{obs} \tag{2.40}$$

and the Jacobian becomes:

$$\frac{dt_{obs}}{d(\Delta E)} = \frac{t_{obs}^3}{mL_{SD}^2}. \tag{2.41}$$

However, the HAS instrument detector used to collect the data in this thesis records number density. This becomes significant when considering the finite size of the detector's ionizer: probe particles are ionized by electron bombardment before being detected. Since the time particles spend within the ionization volume depends upon their velocity, ionization cross-section varies inversely with final particle velocity, v_f, and the corrected scaling factor is given by:

$$f(\Delta E) = \frac{t_{obs}^3}{mL_{SD}^2} v_f f(t) = \left(\frac{t_{obs}^2}{mL_{SD}}\right) f(t_{obs}). \quad (2.42)$$

2.4.3 Thermal Attenuation of Specular Intensity and Electron-Phonon Coupling

Before the first HAS diffraction experiments, the thermal attenuation of reflected neutrons, x-rays, and electrons all had the Debye-Waller (DW) factor. This DW factor adjusts all scattered intensities, accounting for both thermal motion of the lattice and helium beam energy. Effectively, more lattice motion and higher changes in beam momentum and energy diminish the measure HAS intensity. When a surface is heated, thermal energy excites phonons in the lattice. This means that the atom positions become increasingly uncertain. Thus, upon heating a surface it becomes less ordered and coherent, causing the scattered helium to be less coherent and decrease in intensity. When scattering from a surface, if one heats the beam, increasing its energy, the helium will have a larger change in momentum when reflecting from the surface and as its disturbed its coherence is also seemingly reduced. However, this is also true for inelastic scattering where larger magnitude of energy exchange with the surface also diminishes scattered intensity.

Thermal attenuation occurs due to thermally excited phonons disturbing the electron density at the surface. This thermal attenuation is described by the following relation,

$$I(T_S) = I(0)e^{-2W(T_S)}, \quad (2.43)$$

where 2W is the DW factor. The traditional definition of the DW factor is

$$2W(T_S) = \langle \Delta k \cdot u(T_S) \rangle^2, \quad (2.44)$$

where Δk is the change in wavevector of the scattered He and u is mean squared displacement (MSD) of the surface atoms.[26] Recently, Manson et al. has derived a relationship between 2W

and the surface EPC constant via reasonable approximations, yielding the direct proportionality for metal surfaces above the surface Debye temperature,[14,15]

$$\lambda_{HAS} \cong -\frac{d \ln I_{00}}{k_B d T_S} \frac{\phi}{6Z} \frac{k_F^2}{k_{iz}^2}, \tag{2.45}$$

where I_{00} is the intensity of the specular reflection, ϕ is the work function, Z is the number of free electrons per atom, k_F is the Fermi wavevector, and k_{iz} is the surface perpendicular (z) component of the incident helium incident wavevector.

The traditional DW factor can be further analyzed by performing the dot product in the exponent separating the vectors into the sum of surface perpendicular and surface parallel components. Choosing scattering conditions that detector helium pathways have both surface perpendicular and surface parallel (anything off specular) components allows one to probe MSDs on the surface with anisotropic sensitivity.[4,23] The DW factor in its traditional definition is useful in probing the vibrational dynamics of the surface since it accounts for all the phonons at once with some anisotropic sensitivity. Additionally it allows one to predict changes in signal with changes in surface temperature and beam energy.

One must also consider the potential between helium and the surface. Particularly the fact that the helium-surface potential has a local minimum before the repulsive part overwhelms it, repelling the helium atom.[27] This helium-surface potential well depth slightly accelerates the helium atom prior to impact, and decelerates it by the same amount after impact.[27] Thus, this effect must be taken into account for the DW factor. The Beeby approximation is commonly used to correct for this effect, taking into account the acceleration of the helium atom from the helium surface potential before scattering. In the Beeby approximation, the potential well depth is added to the incident helium beam energy.[27] This quantity can be related to the DW factor by

expanding the traditional expression for the DW factor with standard kinematics. Upon substitution, restriction to specular scattering, and rearrangement, the relation,

$$\sigma = -\frac{d(2W)}{dT_S} = 4k_i^2 \frac{d\langle u_z^2 \rangle}{dT_S}\left[\cos^2\theta_i + \frac{D}{E_i}\right], \tag{2.46}$$

is obtained, where σ is the negative slope of a DW linear plot, k_i is the helium incident wavevector, θ_i is the incident angle relative to surface normal, D is the helium-surface potential well depth, and E_i is the helium incident energy.[4,28] Thus, a fit of DW decay, σ, versus $k_i^2\cos^2\theta_i$ yields the helium-surface potential well depth and the first derivative of the mean-square displacement with respect to surface temperature. It is common practice to use the Debye model to extract a surface Debye temperature.[28]

Recall that helium atoms exchange energy with phonons, while they scatter off of the electron density. Thus, inelastic helium–phonon scattering events are actually two concerted scattering events: helium–electron and electron–phonon. A theoretical description of this helium–electron–phonon scattering event has been developed for metals, semiconductors, topological insulators, 2D materials, and metallic films to show that the Debye–Waller (DW) factor is directly proportional to the SEPC (λ_S).[22] The derivation starts from the distorted-wave Born approximation, using second-order perturbation theory to define electron–phonon matrix elements, and adopting additional yet reasonable approximations.[2,14,15,22] The DW factor describes thermal attenuation of the scattered He intensity and does so as a multiplicative factor present in all scattering probabilities.[2,4] As mentioned, the DW factor originally came from neutron and X-ray scattering, accounting for motion of nuclei in the lattice from thermal excitation of phonons.[3,4] However, after being applied to helium atom scattering, the theory was developed, and the role of the electron density elucidated.[20] Simply put, the thermal excitation of

phonons at or near enough to the surface perturbs the surface electron density, reducing the coherence of the scattered He and measured HAS intensity.[2]

2.6 Experimental Apparatus and Parameters

This section details the HAS instrument used to collect scattering data. After covering ultra high vacuum (UHV) conditions, the three main sections of the instrument are thoroughly covered: the

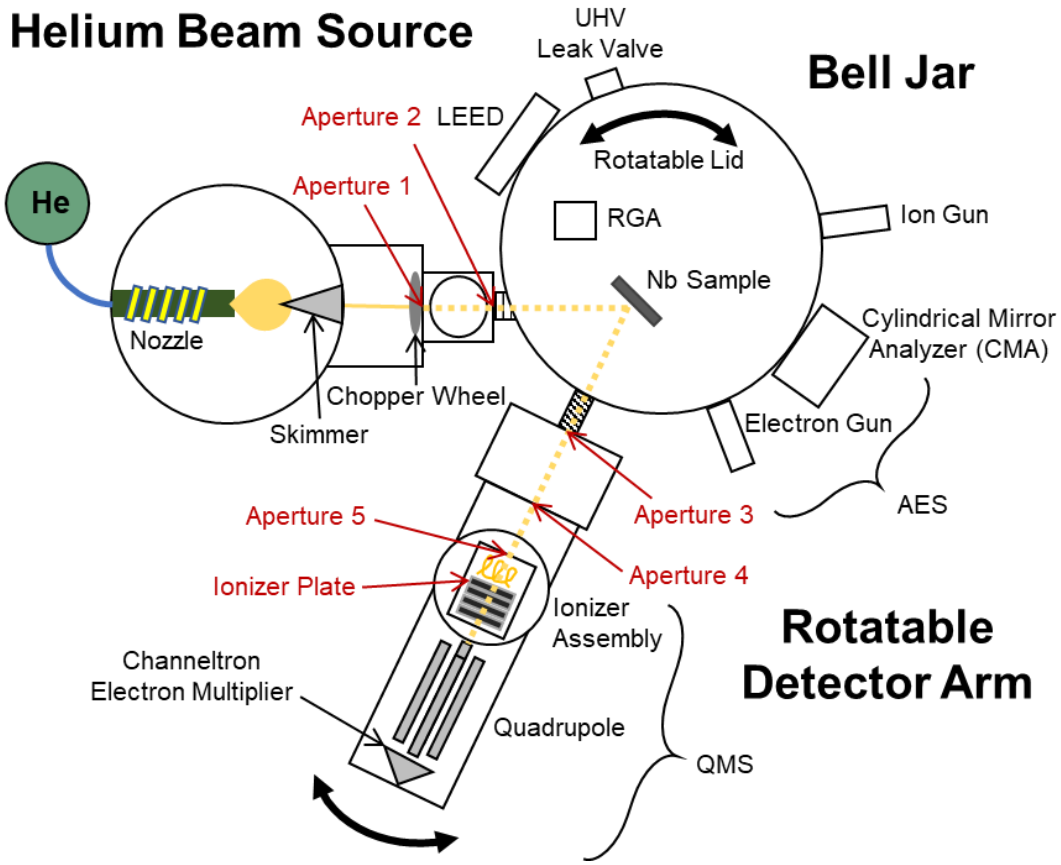

Figure 2.2: Schematic of the He atom scattering apparatus, with instrumentation used in this thesis identified. The collimating apertures are labeled in red.

beamline, the scattering chamber, and the rotatable detector. Then the crystal preparation methods and experimental parameters used in the succeeding chapters. A schematic of the HAS instrument is shown in Figure 2.3.

2.6.1 Ultra High Vacuum

Ultra High Vacuum (UHV) is required for the helium supersonic beam, but also to control and manipulate surfaces. There are various levels of vacuums, summarized in Table 2.1. UHV is obtained by going below 1E-10 Torr. This approximately causes <1E-4 monolayers (assuming a sticking coefficient of unity) to form per second. Thus, controlling and manipulating surfaces requires UHV. At higher pressures more and more gasses collide with the surface – sticking, reacting, or dissolving into the crystal. If the experiment only requires short periods of surface stability one may be able to make their measurements at higher background pressures. Thus, while UHV is the goal and a good benchmark, the optimal background pressure varies for each surface and the time demands of each experiment.

Another reason for UHV is the supersonic beam itself. In fact for scattering experiments, one must consider the mean free path of gas particles in the UHV chamber. The mean free path of an atom, λ, depends on the background pressure, P, temperature, T, and scattering cross section, σ:

$$\lambda = \frac{k_B T}{\sqrt{2} P \sigma}. \tag{2.47}$$

If the mean free path is larger than the size of the UHV chamber, the helium beam is guaranteed to be effectively undisturbed by the background gasses. Additionally, there must be a sufficiently decreasing pressure gradient moving from the beamline to the UHV scattering chamber. This

eliminates back flow from spontaneous diffusion that will oppose, interfere with, and destroy the supersonic beam.

2.6.2 Beamline

The beamline generates a supersonic atomic or molecular beam for scattering experiments. The beamline consists of three differentially pumped regions: the source region, the first differentially pumped chopper region, and a second differentially pumped region that is connected to the scattering chamber with a gate valve. Ultra-high purity helium gas is fed into the source by a single-stage gas regulator (Airgas, Y11-N198K), with backing pressures between 300–1400 psi. The helium pressurized within a custom-built elkonite (Cu-W alloy) nozzle, expands through a 15 μm Mo circular pinhole (SPI) into the source region. The gas line to the nozzle is wrapped around the second stage of a closed-cycle helium refrigerator (Advanced Research Systems, DE-202A), while a resistive ribbon heater (Advanced Research Systems, 36 Ω) wraps around the nozzle and is powered by a PID controller (Lakeshore Cryotronics, Model 325). These cooling and heating components, along with a Si diode (Lakeshore Cryotronics, DT470-SD-13-3S) allow the beam energy to be precisely set and held within ±0.1 K of the set point. To ensure the thermal stability of the entire nozzle manifold, a wrapped tent of Mylar superinsulation limits thermal loss due to radiative heating. The source manifold can heat the nozzle between 50 K and 400 K, which for reference corresponds to experimental helium beam energies, Ei, between 11 meV and 86 meV.

Supersonic beams require high backing pressures, generating very large fluxes in the source chamber that require sufficiently high pumping speeds and large throughputs. In fact, the source chamber has a base pressure of 1 × 10-7 Torr that increases to the order of 1 × 10-4 Torr when a helium beam is pressurized. This difficulty is addressed by equipping the beamline

source region with an 8000 L/s diffusion oil pump (Varian, VHS-400) backed by a 750 m3/h roots blower (Pfeiffer, WKP 500AM) in series with a 70 m3/h rotary vane pump (Pfeiffer, Duo65MC). Upon exiting the source chamber, the expanding gas enters the first differentially pumped chopper region through a conical, Ni skimmer (Beam Dynamics, Model 2) with a diameter of 0.5 mm and approximately 201 cm away from the nozzle pinhole. The skimmer collimates the expanded beam by selecting only its centerline from the zone of silence. This position is carefully optimized to minimize shock waves and improve beam energy resolution. The first differentially pumped chopper region is pumped by a 700 L/s diffusion oil pump (Edwards, Diffstak 160) backed by a 70 m3/h rotary vane pump (Pfeiffer, Duo65MC). As named, within this region is a 15 cm-diameter wheel chopper to modulate the beam and start the timing for TOF measurements. The chopper is mounted on a linear feedthrough (Huntington, VF-108) for an adjustable vertical position. Three different modulation patterns are cut into the chopper at a specific radius from the center. Thus, adjusting the vertical position changes the chopping pattern. A square-wave pattern (50% duty-cycle) is excellent for background subtraction, making it the staple for diffraction experiments. However, TOF experiments require much shorter pulses in time and use either the single-shot (1% duty-cycle) or cross-correlation (50% duty-cycle) patterns. Single-shot has four trigger slots per revolution and allows for highest-resolution TOF measurements with lower intensity, while cross correlation has a pseudorandom, 511-bit pattern of openings that increases intensity and signal-to-noise ratios of TOF measurements, but approximately halves resolution relative to the single-shot. The wheel chopper is powered by a motor (Globe Motors, 75A1003-2) attached to the wheel with high-vacuum bearings (Barden Precision Bearings, SR4SSTA5). The motor is powered by AC voltage from a function generator (Stanford Research Systems, DS335) that is amplified by a stereo

amplifier (Bogen, GS150), resulting in chopper wheel speeds of 7–200 Hz. As briefly mentioned, TOF timing is initiated by a light pulse from an LED source passing through triggering slots in the chopper and sensed by a photon detector. Upon detection, the light pulse generates a TTL pulse, triggering the multichannel scaler (MCS) and successive counting electronics described in Section 2.6.4. After being chopped in the first differentially pumped chopper region, the beam enters the second differentially pumped region through the first collimating aperture of the instrument, labeled Aperture 1 in Figure 2.3—a complete list of aperture dimensions and placements are given in Table 2.2. This second differentially pumped region is pumped by a 135 L/s diffusion pump (Edwards,

Aperture	**Aperture Size**	**Distance from Chopper**
Nozzle	15 μm	-13.81 cm
Skimmer	0.5 mm	-12.81 cm
Chopper	Variable	0
Aperture 1	0.89 mm	2.66 cm
Aperture 2	1.93 mm	22.35 cm
Sample	~4 mm	49.96 cm
Aperture 3	4.45 mm	76.88 cm
Aperture 4	5.56 mm	95.88 cm
Aperture 5	5.79 mm	103.36
Ionizer Entrance Plate	6.35 m	105.97 cm
Filament	N/A	107.01 cm

Table 2.1 HAS instrument aperture sizes and their distances from the chopper; aperature names are consistent with labels in Figure 2.3.

Diffstak 63) backed by the same rotary vane pump used for the first differential stage. After passing through all three beamline regions, the helium beam finally enters the scattering chamber through a second aperture and a manual gate valve (Aperture 2 in Figure 2.3). The first two apertures collimate the incident beam to a 0.22° angular spread that results in an approximately 4 mm diameter beam spot size on the crystal.

2.6.3 Scattering Chamber

The scattering chamber is a UHV bell jar with a differentially pumped, rotatable lid that holds and manipulates the sample as well as equipped with other surface sensitive techniques. Scattering chamber pressure is measured with an ion gauge (Varian, UHV-24) and typical base pressures of 3 × 10-10 Torr are obtainable post bake. The sample mount is fastened to a hexapole manipulator that rotates with the lid and can be positioned for low energy electron diffraction (LEED), Auger electron spectroscopy (AES) and crystal sputtering, or HAS experiments. The UHV of the scattering chamber is carefully maintained for the supersonic beam and surface preparation. The scattering chamber is pumped primarily by a 2400 L/s diffusion pump (Varian, VHS-6) backed by a 24 m3/h rotary vane pump (Pfeiffer, Duo20M), with a 10 in right-angle, pneumatic solenoid valve separating these pumps from scattering chamber. The diffusion oil pump is separated from the right-angle valve by a baffle system cooled by a Freon refrigerator (Polycold, PCT-200). Additionally, there is a 60 L/s ion pump (Perkin-Elmer, 2106035), within the bell jar on the high-vacuum side of the right-angle valve. This pump is a safeguard that maintains vacuum conditions if the right-angle valve closes or the diffusion oil pump malfunctions. The ion pump sublimates titanium filaments, depositing titanium metal in a

cylinder around the filaments. This titanium film aggressively reacts with any and all background gasses, particularly reactive gasses that are hard to pump like water to lower the base chamber pressure. The right-angle valve is interlocked with various metrics to protect the chamber from potential exposure to the foreline or pump oil. These interlocked metrics are the scattering chamber pressure; diffusion pump heater current; diffusion pump temperature, waterline flow, and power; foreline pressure; and baffle temperature. If any of these metrics rise above or below the set value the right-angle valve will close, protecting the scattering chamber and leaving it to be pumped by the ion pump. The sample cooling system, discussed later, further improves vacuum conditions through cryopumping.

The lid of the scattering chamber rests on three concentric, MoS2-coated Teflon spring seals (St. Gobain) that form two differentially pumped regions, the inner lid and the outer lid. The two layers of differentially pumped regions allow the lid to be rotated while keeping the scattering chamber under UHV. The inner lid – closest to UHV chamber – is pumped by a 10 L/s ion pump (Gamma, TiTan), while the outer lid is pumped by a 12 m3/h rotary vane pump (Pfeiffer, Duo10M). These differentially pumped lid regions also must be vented after the scattering chamber is vented. When pumping down, the inner lid first is brought down to rough vacuum (~10-5 Torr) by a sorption pump before the inner lid ion pump is turned on. The manipulator extends into the scattering chamber from the lid, offset 5 cm from the center of the lid and aligned with the geometric scattering center of the instrument. The sample is mounted on this six-axis manipulator (Vacuum Generators, HPT2), allowing precise translation along the x-, y-, and z-axes, rotation in the polar (θ) and azimuthal (ϕ) directions, and tilt (χ) orientation. The manipulator is cooled by a closed-cycle helium refrigerator (Advanced Research Systems, DE-202P) to temperatures of ~200 K. The second stage of the refrigerator connects to an OFHC Cu

bar with a sapphire/In joint, which serves as an anchor for a Cu braid. The Cu braid connects to the mount and sample by an OFHC Cu plate behind the crystal.

Nb surfaces require prohibitively high temperatures to prepare ordered, single crystal surfaces. Thus, a new heating and mount system was designed and built. The heater and mount system is illustrated in Figure 2.4(a) and shown in Figure 2.4(b).

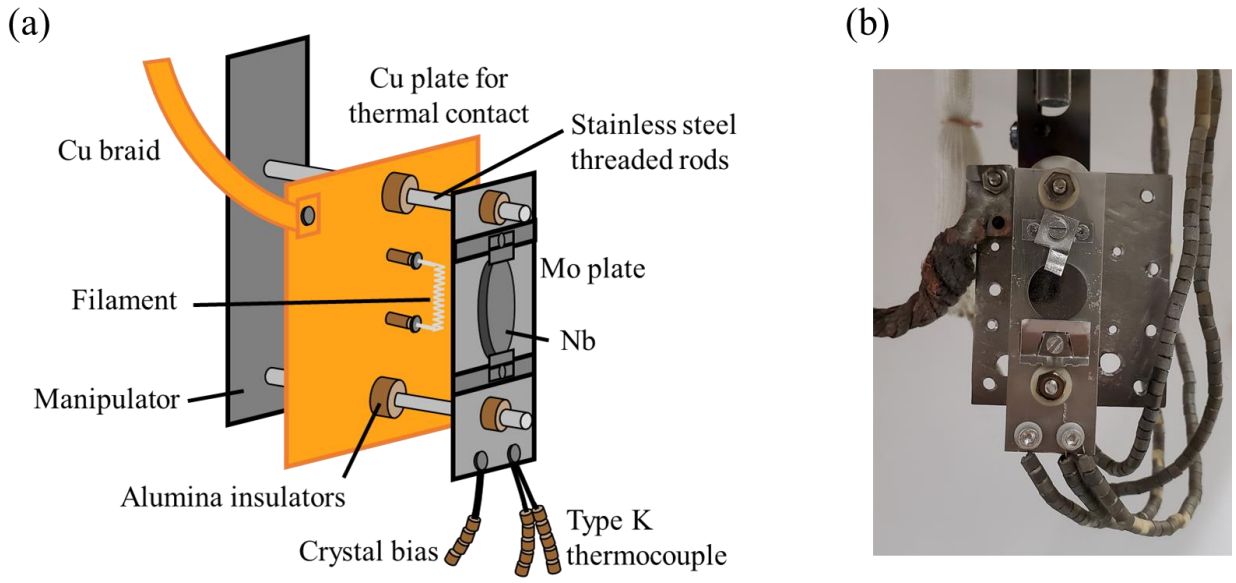

Figure 2.3: (a) Schematic of crystal mounting system viewed from the side; (b) head-on picture of Nb(100) crystal installed on the mount.

The crystal is mounted on a Mo sample plate with Mo clips and screws. These Mo clips and screws which originally were part of a commercial mount (Vacuum Generators). The Cu and Mo plates were fastened to the manipulator via Mo threaded rods on alumina bushings (Al2O3) for thermal and electrical isolation. The heating mechanism was chosen to be an electron-beam (e-beam) generated from a 1%-thoriated W filament. This filament was made by coiling 0.25 mm diameter wire in the threads of 2-52 screws. The ends of the filament were fastened to Mo

rods with Mo nuts (Kimball Physics). The Mo rods supporting the filament were run through a Cu plate (filament plate) and attached to Cu leads that lead to a feed through on the lid. The filament plate is placed behind the sample mount on the same threaded rods with Alumina bushings to electrically float the filament. In use one end of the filament is grounded manually. The filament is powered with a 0–10 A power supply (BK Precision, 1687B) via a vacuum feedthrough. While thermally ejected electrons from the filament, an e-beam is not formed unless there is a voltage difference to direct it. The sample is placed at a positive voltage relative to the grounded filament. Thus, the thermally emitted electrons are accelerated towards and strike the sample, heating it. The filament has a line-of-sight to the sample via a hole drilled through the Mo sample plate. A 0.5 mm, Cu-Mn-Ni alloy bias wire (Alfa Aesar) is fastened to the bottom corner of the Mo sample plate with Mo screws and nuts (DETAILS) and leads to a BNC feedthrough in the bell jar lid. The sample bias to direct electrons from the filament is powered by a 0–600 V power supply (Sorensen, XG 600-1.4). During experiments the sample temperature is monitored by a type-K thermocouple (Omega Engineering) attached to a bottom corner of the Mo sample plate, near the bias wire, with Mo screws and nuts. The leads for the filament, bias wire, and thermocouple are threaded with alumina beads for electronic isolation. Since the Mo sample plate is biased electrically at 0–600 V from ground, the sample thermocouple requires conversion by a signal conditioner (Automation Direct, FCT1) before it's temperature can be read by a PID controller (Eurotherm, 2404). Additionally, a pyrometer (Advanced Energy, LumaSense IGA 140, MB25L, 350–2500°C) is placed in one of the two scattering chamber windows. The larger of the two windows has line-of-sight of the sample when the lid is in the Auger position, while the smaller window has line-of-sight to the sample

when the lid is near the scattering position. Next, when and how these two thermometers are used will be discussed.

The e-beam heater has two modes of heating: e-beam heating (>800 K) and radiative heating (<800 K). Thus, the appropriate thermometry depends upon the temperature range and lid position. In e-beam heating the filament is powered with the sample at a positive voltage, just as previously discussed. In radiative heating only the filament is powered with a neutral sample. When radiatively heating, there is not a focused e-beam, but blackbody radiation emitted from the filament in all directions that evenly heats the sample and its Mo plate. Thus, the appropriate thermometry depends upon the temperature range and lid position. For radiative heating the sample plate is heated evenly by the blackbody radiation, allowing the fastened thermocouple to measure the temperature of the plate and the sample. However, when e-beam heating there is a temperature gradient between the sample and the corner of the sample plate where the thermocouple is fastened. This is calibrated by simultaneously recording thermocouple and pyrometer temperatures throughout the e-beam temperature range. The system was let to thermally equilibrate for about 5 minutes before these values were recorded. This time was determined by observing both temperatures stabilize after about 2 - 5 minutes of reaching the set point. With this calibration curve we can convert the thermocouple temperature on the bottom corner of the sample plate to a pyrometer reading which is taken as the true sample temperature. This allowed the thermocouple to be used to measure the sample temperature while scattering. To ensure this calibration was applicable during measurements, the sample mount system was always allowed to thermally equilibrate for about 5 minutes prior to measurement.

Beyond the use of different thermometry, the Eurotherm PID controller would control the heater output in various ways. During experiments, the Eurotherm PID controller monitors the

calibrated thermocouple and regulates heater output via the filament power (0–5.1 A) while the sample bias is manually set (0–600 V). For the experimental set up, the sample temperature would be stable within ±1 K of the set point. However, when preparing the sample (in a different lid position and temperature range: between 1600 K and 2400 K) the filament is manually set (0–5.8 A), while the Eurotherm PID controller regulates the heater output via the sample bias (0–600 V). During sample preparation the temperatures are stable within ±1–5 K of the set point. A guided user interface and software program was written and developed in LabVIEWTM (National Instruments, LabVIEWTM 2015) to be an interface with the Eurotherm PID controller.

Sample preparation is monitored with traditional surface analysis equipment by simply rotating the lid of the scattering chamber. Crystal structure and azimuthal orientation may be confirmed by reverse-view low-energy electron diffraction (LEED) with an integral electron gun (Princeton Research Instruments, RV-8-120). Surface quality and composition may be further analyzed by Auger electron spectroscopy (AES), with a seperate offset electron gun (Phi, 04-015) and a double-pass cylindrical mirror precision electron energy analyzer (Phi, 15-255). Sample can be cleaned with a sputter gun (Phi, 04-191) positioned near the AES analyzer. The sputter gun ionized back-filled Ne gas through a UHV leak valve (Duniway, 9069) and accelerates the ions toward the sample to initiate ion bombardment. Scattering chamber partial pressures are monitored daily with an installed residual gas analyzer (RGA) (Extrel, RGA300M.

The scattering chamber connects to the detector with a custom welded UHV bellows and a hand-operated gate valve. The next section will discuss the path of scattered helium through the rotatable detector.

2.6.4 Rotatable Detector

The He atom enters the first stage of the detector's differential pumping through a collimating aperture (Aperture 3 in Figure 2.3). This region is connected to a 135 L/s diffusion oil pump (Edwards, Diffstak 63)—backed by a 12 m3/h rotary vane pump (Pfeiffer, Duo10M) common to the entire detector—by a pneumatic gate valve and liquid N2-filled baffle trapping system. Additionally, there is a UHV leak valve (Varian, 951-5106) installed in this region that is useful for calibration and troubleshooting the detector. After passing through Aperture 4 (Figure 2.3), the scattered He atom enters the second stage of differential pumping, which houses the ionizer and Aperture 5 (Figure 2.3). This stage is pumped by a 200 L/s turbo pump (Pfeiffer, TPU170) backed by a 135 L/s diffusion oil pump (Edwards, Diffstak 63) and the rotary vane pump. The third stage of the detector contains the quadrupole and is pumped by a 280 L/s diffusion oil pump (Edwards, Diffstak 100) backed by the rotary vane pump, which is connected to the vacuum region by a pneumatic gate valve and liquid N2-filled trap. The gate valves in both the first and third stages of the detector are kept closed unless scattering experiments are in progress; when these valves are closed, vacuum is maintained by the turbo pump in the ionizer region. The base pressure of the detector after it has been baked, as measured by an ion gauge (Varian, UHV-24) in the ionizer region, reaches 1 × 10-10 Torr when both gate valves are open. The detection system consists of an axial ionizer (Extrel, 041-1), ion optics, a quadrupole mass spectrometer (QMS) rod assembly (Extrel, 7-324-9), and an off-axis channeltron electron multiplier (Photonis, 4816). He is ionized by electron bombardment from a hot, 0.005" diameter, 1%-thoriated W filament with typical emission currents of 11 mA. Electrons are focused on the He beam path by a grid biased relative to the ionizer plate; typical settings for the grid and other optics, optimized for He ions, are listed in Table 2.2.

Detector Parameter	Setting
Ionizer	11 mA
Ion Energy	57 V
Electron Energy	191 V
Extractor	12 V
Lens 1	15 v
Lens 2	16 V
ELFS Plate	137 V
Electron Multiplier	2900 V

Table 2.2 Operating currents and voltages for the detector's ionizer, ion optics, and QMS.

He ions are extracted, accelerated, and focused into the quadrupole entrance by two electrostatic lenses. Radiofrequency and DC voltages are applied across the quadrupole rods—which filter incident atoms based on mass-to-charge ratios—by a power supply (Extrel, QPS50) that interfaces with LabVIEW^{TM} software through a USB data acquisition (DAQ) device (National Instruments, USB-6001). The filtered He ions are detected by the electron multiplier, which converts the ions into pulses that are between 5–15 mV in height and approximately 5 ns wide. These pulses are sent through a 200× fast preamplifier (Ortec, VT120A) before traversing a cable to the counting electronics. The pulses then pass through an amplifier and discriminator (Phillips Scientific, 771 quad bipolar amplifier with six channel discriminator), which removes unwanted background signal and converts the raw pulses to NIM pulses that are 1.6 V tall and 50 ns wide. A custom-built multichannel scalar converts the NIM pulses to TTL and counts the TTL pulses; it is timed by a custom-built CAMAC. The CAMAC is triggered by the chopper and

controlled by LabVIEW^{TM} software through a GPIB interface (LeCroy 8901A). The entire detector sits on a turntable that rotates through a manual- or computer-controlled motor and gear assembly. The angular range of the detector is 38° and is decoupled from the polar angle of the sample manipulator: the detector can be scanned across a wide range of final scattering angles for each incident scattering angle. LabVIEW^{TM} software is used to interface with the motor through an optical encoder and an up-down counter, and the detector rotates with 0.1° precision. The overall angular resolution of the instrument, from the chopper to the multiplier, is FWHM = 0.45°, while the total flight path is approximately 1 m.

2.6.5 Crystal Preparation and Typical Experimental Parameters

The Nb(100) crystal was purchased from Surface Preparation Laboratory (Netherlands, 99.99% purity, ~0.1° cut accuracy) and cut to a 10 mm diameter, 2 mm thick disk. The Nb crystal initially showed C, B, and S impurities with AES, which were removed with repeated annealing at and flashing to ~1900 K, with 500 eV Ne + used to sputter impurities from the surface (PNe ~ 5.5 × 10^{-5} Torr, 3 μA maximum emission). On special occasions when the O content of the crystal diminished, the crystal was exposed to backfilled O_2 at ~ 4 × 10^{-8} Torr and heated to ~1250 K for periods of 5 – 10 minutes. A repeated cycle of annealing, flashing, and sputtering continues until after a 1900 K anneal for at least 1 hour, does not bring up impurities. Surface order was initially checked with LEED. A representative LEED image is shown in Figure 2.5.

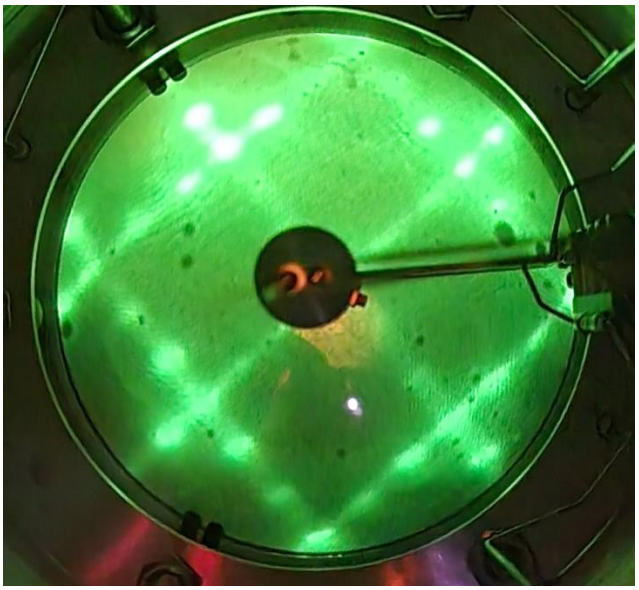

Figure 2.4: Representative LEED image of the (3 × 1)-O Nb(100) surface after preparation.

As will be covered later, Nb(100) surface reconstructs into a (3 × 1)- O superlattice structure. This is evident in the provided LEED image. The BCC of the Nb(100) surface is broken by the three fold symmetry along both directions due to 90°- rotated domains. Diffraction scans were taken next to verify surface structure and order. These scans are discussed in Chapters 3 and 4 were obtained by rotating the detector. The detector collects data at increments of 0.2°, which typically lasted ~5 seconds. Square-wave chopping generates open and closed (background) signal channels; diffraction scans sum the intensity of the open channel and subtracts the sum of background channel intensity generating an intensity value at each 0.2°. The incident scattering angle, θ_i, is the average of the detector angle, θ_{det}, at specular and the instrument's included angle, θ_{inc}, which is determined by the geometry of the detector (θ_{inc} = 54.3° for these experiments). The final angle, θ_f, is obtained from the θ_{det} and θ_{inc} via the relationship: $\theta_f = \theta_{det} - \theta_i + \theta_{inc}$. The raw data in each diffraction scan is recorded as the scattered intensity vs. θ_{det}. The x-axis, the θ_{det}, may be converted to ΔK through Equation 2.15,

as long as k_i is obtained with a TOF spectrum and Equation 2.16. TOF spectra were modulated with either the single-shot or cross-correlation chopper modes. In single-shot experiments, the chopper wheel spun at 200 Hz with 4 μs channel times, however for cross-correlation experiments, the chopper wheel spun at approximately 196 Hz with 10 μs channel times. The time length of each scan was dependent upon signal, noise, and resolution. These change for various sets of incident and final conditions. Typically, TOF spectra were save in summed batches every 20–60 min. If the spectra have poor resolution or signal-to-noise ratio, more TOF were taken and summed until sufficient signal-to-noise ratios were obtained. Within a TOF the center of the elastic peaks were used to measure the incident beam energy. Inelastic peak times were converted to phonon energies and wavevectors through Equations 2.26-27.

Chapter 3

Persistence of the Nb(100) Surface Oxide Reconstruction at Elevated Temperatures

Chapter 3 is an adapted version of the article, McMillan, A. A.; Graham, J. D.; Willson, S. A.; Farber, R. G.; **Thompson, C. J**.; Sibener, S. J. Persistence of the Nb(100) Surface Oxide Reconstruction at Elevated Temperatures. Superconductor Science and Technology 2020, 33, 105012, before peer review or editing, as submitted by A. A. McMillan to Superconductor Science and Technology. IOP Publishing Ltd is not responsible for any errors or omissions in this version of the manuscript or any version derived from it. The Version of Record is available online at https://iopscience.iop.org/article/10.1088/1361-6668/abaec0.[29]

Helium atom scattering and Auger electron spectroscopy (AES) are used to characterize the (3×1)-O reconstruction of the Nb(100) surface at elevated temperatures. Persistent helium diffraction peaks and specular lineshape analysis indicate that the oxide structure persists, apparently unchanged, until surface temperatures of at least 1130 K. In a complimentary experiment, AES oxygen to niobium ratios for Nb(100) show little to no change when the surface temperature is varied from 300 K to 1150 K. These data inform future development of superconducting radio frequency (SRF) cavities. In particular, these findings demonstrate the important role that niobium oxides play in the optimization of growth strategies and coating procedures for Nb_3Sn and other next–generation SRF superconducting alloy materials.

3.1 Introduction

Niobium has become the material of choice for modern superconducting radio frequency

(SRF) cavities in particle accelerators. Its low surface resistance (R_S), high critical temperature (T_C), and relatively high cavity quality (Q) factor at large fields all have contributed to its current use in SRF cavities [30–33]. In addition, pure Nb is relatively soft and ductile, which allows it to be formed and welded into the cavity geometries required to optimize Q factors and accelerating gradients [30]. Extensive research has been performed on these cavities and enables them to operate close to the fundamental limits of Nb [32–38]. Future progress, then, rests on the development of new materials: one of the most promising options is Nb_3Sn. Theoretical and experimental advances show that Nb_3Sn cavities could yield higher Q factors with larger accelerating gradients at higher operational temperatures than traditional Nb cavities [39–44], improving performance while also greatly reducing the cost of infrastructure and cryogens.

Unlike Nb, there are substantial issues associated with making cavities from Nb_3Sn [32]. While its brittle nature and poor thermal conductivity prevent it from being fashioned into a cavity directly, thin Nb_3Sn coatings formed on Nb have shown promising results [32,45]. This process typically involves coating an existing Nb cavity with Sn, and then annealing at high temperatures to form the Nb_3Sn thin film at or near the surface [35,46]. Research into the microscopic formation of these thin films is necessary for advancement of SRF technology.

One complication present in the growth of Nb_3Sn thin films is the role of Nb's native oxide layer. Nb is highly reactive to oxygen and its surface usually is covered by one of many possible oxide structures, both in air and in vacuum [47,48]. The oxygen exposures required to reach these different oxide structures, as well as the structures themselves, have been well characterized [47–51]. Generally, a thick insulating Nb_2O_5 layer dominates the surface in air, while thin ordered (n×1)-O domains ("ladders") form readily on a Nb(100) surface after high temperature annealing in vacuum [49,52–54]. As a refractory metal, Nb has a high melting

temperature of 2741 K [55]. The oxygen in Nb starts to desorb as NbO and NbO_2 [56,57] above 1900 K [47] in ultra–high vacuum (UHV), and it is not until Nb is heated above 2500 K that pure, clean, oxygen–free Nb is seen [47,56–60]. The extreme temperatures needed to remove oxygen mean that the Nb SRF cavities are coated in an oxide layer, and that the Sn deposited to form Nb_3Sn is deposited on one of many Nb oxides. The growth morphology of Nb_3Sn on Nb is dependent on the interaction of Sn with the oxide layer. Thus, a complete, temperature–dependent, microscopic understanding of the Nb oxide surface is critical to the development of consistent, well–formed Nb_3Sn thin films. Such understanding will allow for the development of alloy growth procedures with improved overall quality, homogeneity, and stoichiometry, enhancing critical operational SRF characteristics in high fields.

A key, missing factor in the literature is the nature of the Nb oxide surface at elevated temperatures. Up until now, studies have been limited to analyses at or below room temperature: thermal history and desorption temperatures are known, but the structure and stoichiometry at high temperatures has not been elaborated. In Nb_3Sn SRF cavity fabrication processes, the Nb surface temperature is elevated during Sn nucleation, annealing, and degassing [32,35,46]. An understanding of the Nb oxide surface at elevated temperatures will guide current and new routes for improved Nb_3Sn cavity production. To our knowledge, this combined helium atom scattering (HAS) and Auger electron spectroscopy (AES) study represents the first investigation of the Nb(100) oxide ladder structures at elevated temperatures, and it is one of the few in-situ studies of metal oxide structures at high temperatures.

HAS is a unique, nondestructive, surface sensitive technique that elucidates surface structure and dynamics [61]. The helium atoms are neutral probes that scatter off the electron cloud a few angstroms away from the surface: the surface is not damaged in any way [3,4,21]. HAS is

particularly suited for examining surface structure at elevated temperatures. Unlike in typical low–energy electron diffraction (LEED), where electron bombardment heating presents experimental challenges, the neutral helium probe is not affected by the high voltages required for electron bombardment. Scanning tunneling microscopy (STM) also becomes very difficult at extremely high sample temperatures, due to atomic thermal fluctuations and instrument instability [62]. Debye–Waller attenuation of scattered He does become increasingly more important at elevated surface temperatures [21], but if the crystal is sufficiently reflective, diffracted He signal can be seen above the diffuse scattering background and the surface structure obtained.

3.2 Experimental

3.2.1 Helium Atom Scattering – Methods and Sample Preparation

The surface structure of Nb(100) was characterized with a UHV HAS apparatus that has high momentum and energy resolution. The apparatus has been described in detail elsewhere but is summarized here [63]. The HAS instrument consists of three regions: a differentially pumped beam source, a sample chamber, and a rotatable detector arm, resulting in a total helium flight path of 1.0701 m (chopper–to–crystal distance of 0.4996 m, crystal–to–ionizer distance of 0.5705 m).

The helium was expanded through a 15 μm nozzle that was cooled by a closed–cycle helium refrigerator. This generated a nearly monoenergetic ($\Delta v/v \leq 1\%$), supersonic helium beam that was collimated into an approximately 4 mm spot on the crystal surface. A mechanical chopper modulated the beam prior to collision with the surface; a 50% duty cycle was used for angular distributions and a 1% duty cycle for time–of–flight measurements to determine the beam energy. The Nb(100) crystal was mounted on a six–axis manipulator that precisely

controlled the incident angle, θ_i, the azimuthal angle, ϕ, and the tilt, χ, with respect to the scattering plane. Sample temperatures ranging from 300 K to 1900 K were achieved using electron bombardment in combination with a closed–cycle helium refrigerator. Reflected helium atoms entered a triply differentially pumped, computer–controlled, rotatable detector arm; were ionized via electron bombardment; filtered using a quadruple mass spectrometer; and detected with an electron multiplier followed by pulse counting electronics. Angular distributions were obtained by rotating the detector at 0.2° increments while holding the incident angle and energy fixed. The overall instrument resolution was 0.45°. The incident helium beam was held at 21 meV (k_i = 6.3 Å^{-1} and T_n = 96.9 K) so that the specular, first–order primitive, and (3×1)-O superlattice diffraction peaks could be observed in the same angular distribution.

Nb(100) was obtained from Surface Preparation Laboratory (Netherlands, 99.99% purity, ~0.1° cut accuracy) and prepared in the HAS apparatus by cycles of annealing at and flashing to 1900 K. The primary initial impurities identified by AES were carbon, boron, sulfur, and nitrogen. Sputtering with 500 eV Ne^+ ions removed the boron and sulfur contaminants while the combination of annealing and flashing eventually removed the carbon. Annealing and sputtering continued until AES analysis showed only niobium and oxygen present on the surface. Flashes to 1300 K were performed before experiments to remove any trace adsorbates from the crystal surface.

3.2.2 Auger Electron Spectroscopy – Methods and Sample Preparation

AES measurements of Nb(100) from Surface Preparation Laboratory (Netherlands, 99.99% purity, ~0.1° cut accuracy) were performed in a UHV experimental system composed of a scanning tunneling microscopy chamber (UHV VT–STM, RHK Technology) and a preparation chamber equipped with AES capabilities, as previously described [52]. The Nb(100) crystal was

cleaned via repeated cycles of Ar^+ ion sputtering and electron bombardment annealing at a sample temperature (T_S) of approximately 2100 K, as measured using a Mikron Infrared (MG–140) pyrometer. Surface cleanliness was confirmed by AES and STM analyses, which showed the characteristic (3×1)-O superlattice with no surface contaminants [49,52,64].

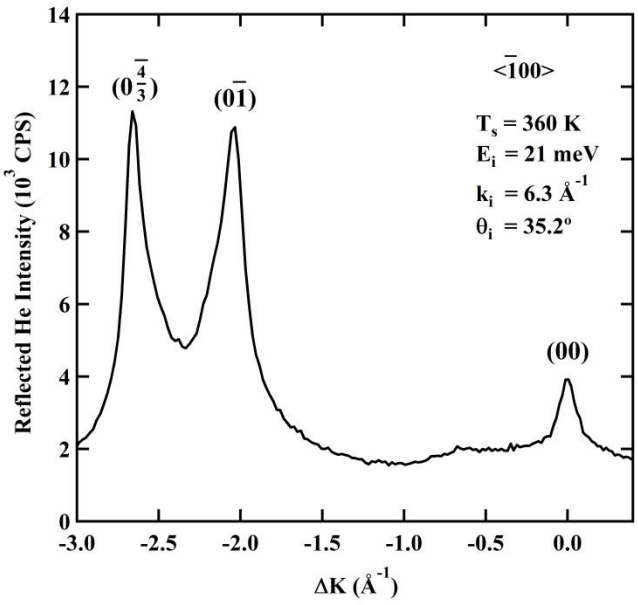

Figure 3.1: Representative diffraction spectrum for He on (3×1)-O/Nb(100) along the <$\bar{1}$00> symmetry axis as a function of parallel momentum exchange.

3.3 Results and Discussion

3.3.1 Helium Diffraction

After preparation in vacuum, the Nb(100) surface reconstructs into a (3×1)-O ladder structure, as observed elsewhere [52]. Figure 3.1 shows an angular distribution of helium back−scattered from the Nb(100)/(3×1)-O surface along the <$\bar{1}$00>, ($\bar{\Gamma} - \bar{X}$) azimuthal direction. The diffraction spectrum was taken at a surface temperature of 360 K with an incident angle of θ_i = 35.2°. The reproducibility of the surface was confirmed through repeated scans at T_S = 360 K after flashing the crystal to 1300 K. Three diffraction peaks are resolved clearly: a zeroth−order specular peak ($\theta_i = \theta_f$) at ΔK = 0 Å^{-1}, a first−order, $(0\bar{1})$ diffraction peak at ΔK = -2.0 Å^{-1} (θ_f =

14.7°), and a (3×1)-O superlattice, $\left(0\frac{\overline{4}}{3}\right)$ diffraction peak at ΔK = -2.6 Å^{-1} (θ_f = 9.1°). These elastic diffraction peaks arise when the requirements for Bragg diffraction are satisfied, such that

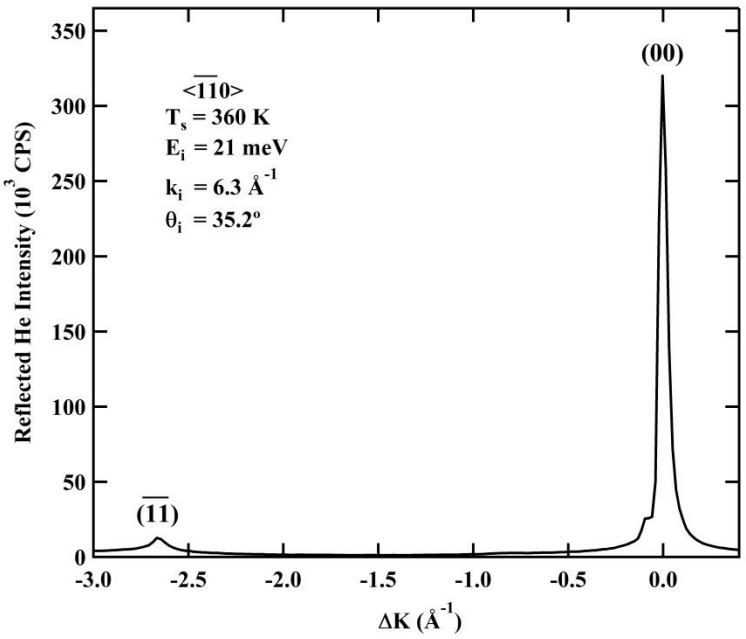

Figure 3.2: Representative diffraction spectrum for He on (3×1)-O/Nb(100) along the <$\overline{1}$10> symmetry axis as a function of parallel momentum exchange.

$$\Delta K = k_i(\sin\theta_i - \sin\theta_f) = G_{mn}, \tag{4.1}$$

where ΔK is the change in the surface−parallel component of the helium wavevector k_i; θ_i and θ_f, respectively, are the initial and final scattering angles relative to the surface normal; and G_{mn} is a linear combination of surface reciprocal lattice vectors. From the first−order, $(0\overline{1})$ diffraction peak, the Nb−Nb lattice spacing was determined to be 3.08 ± 0.02 Å, which corresponds favorably to surface lattice constants found through LEED measurements [49]. The diffraction peak at ΔK = -2.6 Å^{-1} was identified as (3x1)-O superlattice peak, since its ΔK value is approximately

$\frac{4}{3}$ times that of the $(0\overline{1})$, primitive peak. This also aligns with previous LEED studies that show the (3x1)-O superlattice structure [49]. The intensities of both the $(0\overline{1})$ and $\left(0\frac{\overline{4}}{3}\right)$ peaks are far greater than that of the specular peak, which is in contrast to HAS from the bare Nb(100) surface and

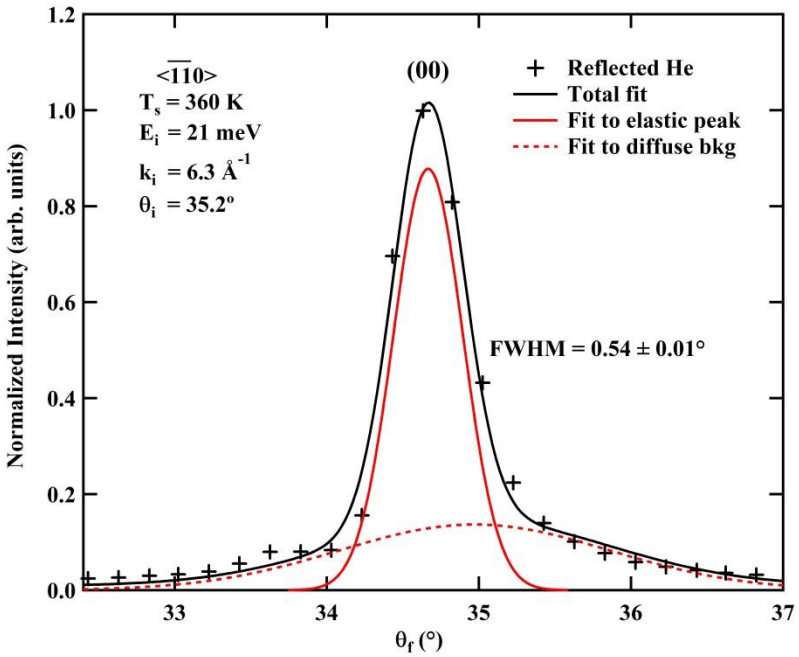

Figure 3.3: Width analysis of a specular ($\theta_i = \theta_f$) He diffraction peak on (3×1)-O/Nb(100) along the <$\overline{1}$10> symmetry axis, plotted vs. final scattered angle (θ_f). The solid red line is a Gaussian fit to the coherent elastic peak, the dashed red line is a Gaussian fit to the diffuse elastic and multiphonon background, and the solid black line is the overall fit to the data (black crosses). The narrow, coherent elastic peak (solid red line) has a FWHM of 0.54 ± 0.01°.

suggests an increase in surface corrugation as a result of the ladder structure [60,65].

The angular distribution of the <$\overline{1}10$>, ($\overline{\Gamma} - \overline{M}$) azimuthal direction was determined and is shown in Figure 3.2 at T_S = 360 K. In this direction, the specular peak is far more intense than in the <$\overline{1}00$> direction, again indicating a high surface corrugation. The small, secondary specular peak can be attributed to surface faceting from the anneal process and was ignored in analysis [60]. The peak at ΔK = -2.7 Å^{-1} corresponds to the ($\overline{11}$) diffraction peak.

The high intensity of the specular peak in the <$\overline{1}10$> direction allowed us to analyze the

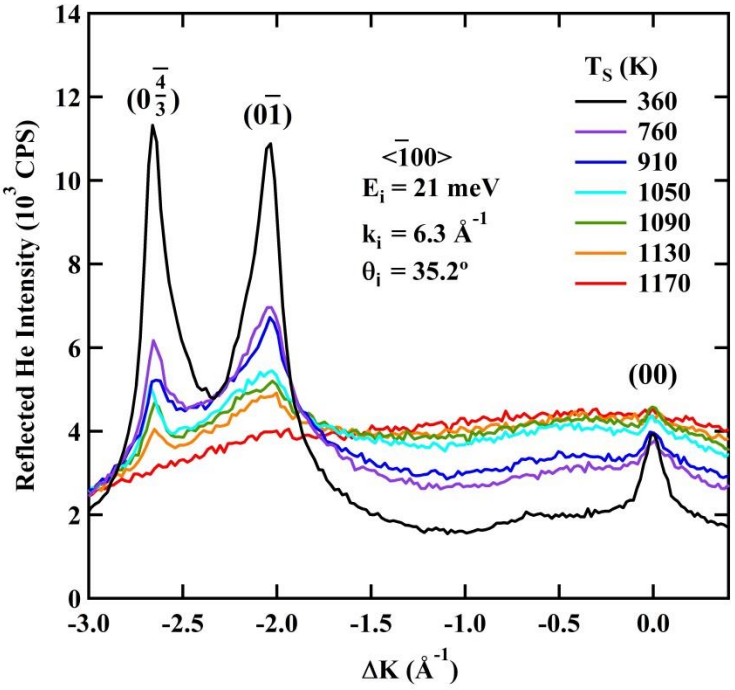

Figure 3.4: Decay of diffraction spectra for He on (3×1)-O/Nb(100) along the <$\overline{1}$00> symmetry axis as a function of surface temperature, plotted vs. parallel momentum exchange.

peak lineshape with minimal contributions from the diffuse elastic and multiphonon background seen in the <$\overline{1}$00> direction. The helium beam strikes the surface with a 4 mm spot size, averaging over many atomically flat terraces. The average width of these terraces has been

shown to be approximately equal to the coherence length, l_c [25,66]. The specular peak broadening from the average domain size, $\Delta\theta_w$, can be found through a deconvolution of the measured specular peak full width half maximum (FWHM), $\Delta\theta_{exp}$, and the instrument function broadening, $\Delta\theta_{inst}$:

$$\Delta\theta_w^2 = \Delta\theta_{exp}^2 - \Delta\theta_{inst}^2. \tag{4.2}$$

The coherence length then can be determined through the equation [66],

$$l_c = \frac{5.54}{\Delta\theta_w k_i \cos(\theta_f)}. \tag{4.3}$$

Figure 3.3 shows the fitting function used to determine the width of the specular peak. The

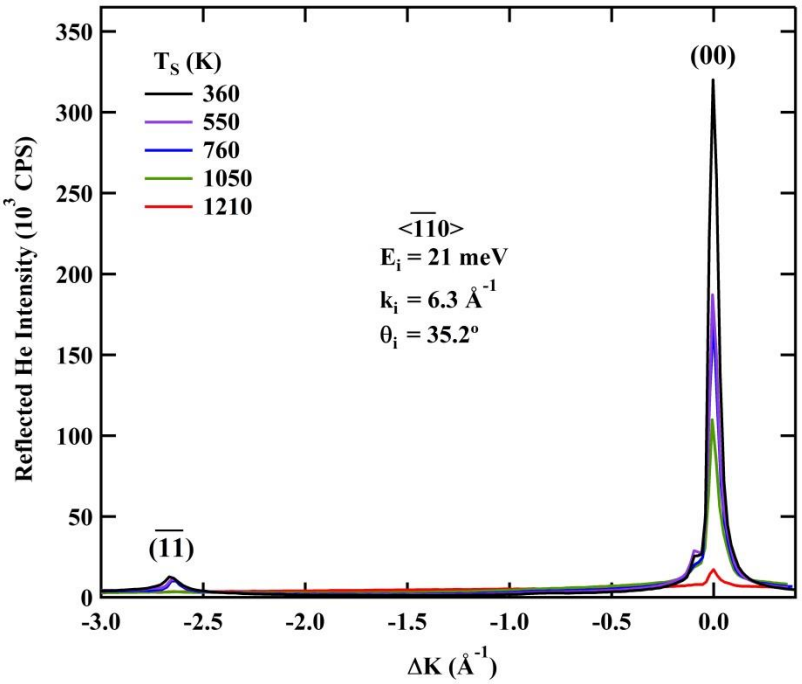

Figure 3.5. Decay of diffraction spectra for He on (3×1)-O/Nb(100) along the <$\overline{1}10$> symmetry axis as a function of surface temperature, plotted vs. parallel momentum exchange.

normalized peak was fit with one sharp Gaussian function for the coherent elastic signal and one broad Gaussian for the diffuse elastic and multiphonon background signal [67]. With an overall instrument resolution of 0.45° and a measured specular FWHM of 0.54 ± 0.01°, the average domain size was found to be 210 ± 10 Å.

Diffraction spectra in the <$\bar{1}$00> direction, as a function of increasing temperature, are shown in figure 3.4. Surface stability at each temperature was determined by immediately repeating each scan; the identical scans indicated that the surface structure was unchanging. While the specular peak is enveloped by the background at around 1053 K, the $(0\bar{1})$ and $\left(0\frac{\bar{4}}{3}\right)$ diffraction peaks are visible up to at least 1130 K, at which point the peak intensities are lower than the detected background.

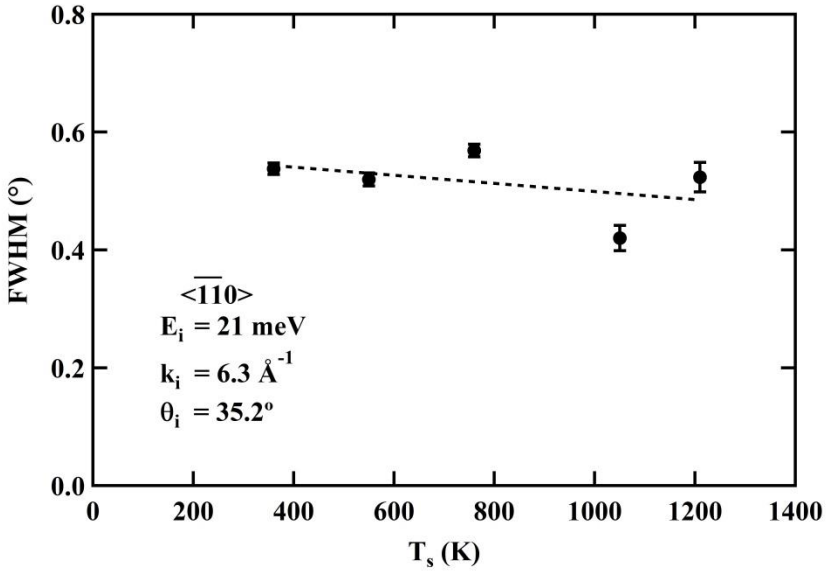

Figure 3.6: FWHM of Gaussian fits to the coherent elastic portion of specular ($\theta_i = \theta_f$) He diffraction peaks on (3×1)-O/Nb(100) along the <$\bar{1}$10> symmetry axis, plotted vs. surface temperature. All peaks were fit with two Gaussians, as illustrated in figure 3. Dotted line is to guide the eye.

Temperature dependent spectra in the <$\overline{1}10$> direction are shown in figure 3.5. Spectra were recorded as a function of increasing temperature, except for the spectrum taken at 550 K, which was taken after a 1900 K flash. The specular intensities at five different surface temperatures were fit in a similar manner to that shown in figure 3.3, and the FWHM of each coherent elastic peak is shown in figure 3.6. HAS lineshapes are very sensitive to surface disorder [21,65]; any oxygen dissolution or disorder caused by the elevated temperatures would dramatically increase the width of the specular peak. Instead, the width stays nearly constant as a function of surface temperature up to 1210 K, as seen in figure 3.6. This, in addition to the existence of the superlattice diffraction peak in figure 3.4 at 1130 K, indicate that the (3×1)-O superlattice remains unchanged on the Nb(100) surface up to at least 1130 K, and presumably up to at least 1210 K.

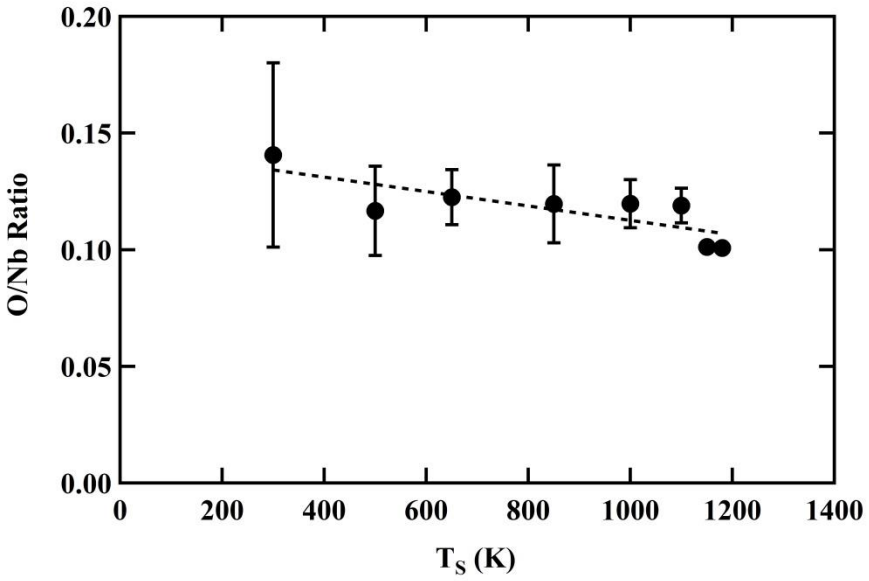

Figure 3.7: O/Nb AES ratios taken at T_s between 300 K and 1150 K. There is no significant decrease in O content on Nb(100) below 1200 K. Dotted line is to guide the eye.

3.3.2 Auger Electron Spectroscopy

A second Nb(100) single crystal was prepared in a separate UHV experimental system, which resulted in the (3×1)-O superlattice structure [52,68]. In order to determine the concentration of surface oxygen on Nb(100) at elevated temperatures, a ratio of the peak–to–peak intensities of the principle O and Nb peaks were obtained, at 519 eV and 169 eV, respectively [69], for T_S ranging from 300 K to 1150 K. The O/Nb ratios displayed in figure 7, plotted as a function of T_S, quantitatively describe the surface composition at elevated surface temperatures. To our knowledge, this is the first AES data demonstrating the effects of thermal annealing on oxidized Nb samples that capture the surface composition at these high temperatures.

Across the entire temperature range studied in this work, the O/Nb ratio is stable, providing evidence for a constant surface oxygen concentration up to 1150 K. The near surface does not lose oxygen from the thermal annealing [52], even though the subsurface oxygen content may vary due to the cleaning procedure and the amount of oxygen in the bulk, as seen by slight fluctuations in the O/Nb ratio at T_S = 300 K. The average measured Auger peak intensities did not change as a function of primary beam exposure time, indicating that the AES experiments did not modify the surface elemental composition over the course of data collection. Furthermore, the Nb(100) surface was analyzed by in-situ, room temperature STM following the AES measurements. The STM work confirmed that the surface remained covered by the characteristic (3×1)-O superlattice and that the sample was not damaged by the high temperature AES measurements. Residual gas analyzer spectra indicated that the oxide did not desorb within the studied temperature range, so any observed reduction in the O/Nb ratio would be a result of oxygen dissolution into the bulk crystal. However, based on the AES O/Nb ratios detailed in

figure 3.7, there is no evidence of appreciable oxygen dissolution below 1200 K. This AES analysis confirms the HAS measurements that show no appreciable oxygen dissolution or disorder within the T_S range studied.

3.4 Conclusion

Helium atom scattering and Auger electron spectroscopy provide evidence for the continued existence of a (3×1)-O ladder structure on the Nb(100) surface until at least 1130 K and, to our knowledge, this work is the first investigation of the niobium oxide surface at elevated temperatures. Helium diffraction peaks from the oxide structure were persistent until 1130 K, and the specular peak lineshapes indicated little to no surface disorder up to 1210 K. The constant AES oxygen to niobium peak ratios of Nb(100) also indicated that oxygen did not leave the surface either through dissolution or evaporation until above 1200 K, consistent with previous studies [47,49]. The unvaried oxide reconstruction at the investigated high temperatures informs future SRF cavity research and development. The next−generation method of coating Nb cavities with a thin film of Nb_3Sn involves an initial nucleation step where the surface is held at about 770 K [32], below the 1130 K threshold measured here. Our research shows that Sn is nucleating on an oxide, not on bare Nb. This further illuminates the role of oxygen in the Sn deposition and cavity optimization processes. The oxide structure above 1130 K−including at approximately 1375 K [32] where the Sn−coated cavities are annealed−is still unknown, and would bring similarly interesting information to the discussion on SRF cavity production. Additional unanswered questions include Sn mobility, long−term stability, the mechanisms and kinetics for Sn incorporation into the Nb substrate, and the development Nb_3Sn alloy materials with lower defect concentrations and higher chemical and spatial uniformity. These questions need to be

addressed to realize the SRF community's ambitious goal to successfully implement this promising alloy in next−generation accelerator applications.

Chapter 4

A Combined Helium Atom Scattering and Density-Functional Theory Study of the Nb(100) Surface Oxide Reconstruction: Phonon Band Structures and Vibrational Dynamics

Chapter 4 is reproduced from McMillan, A. A.; **Thompson, C. J.**; Kelley, M. M.; Graham, J. D.; Arias, T. A.; and Sibener, S. J. A Combined Helium Atom Scattering and Density-Functional Theory Study of the Nb(100) Surface Oxide Reconstruction: Phonon Band Structures and Vibrational Dynamics. *J. Chem. Phys.* 156, 124702 (2022) with the permission of AIP Publishing. Copyright 2022 The Journal of Chemical Physics.[70]

Helium atom scattering (HAS) and density-functional theory (DFT) are used to characterize the phonon band structure of the (3 × 1)-O surface reconstruction of Nb(100). Innovative DFT calculations comparing surface phonons of bare Nb(100) to those of the oxide surface show increased resonances for the oxide, especially at higher energies. Calculated dispersion curves align well with experimental results and yield atomic displacements to characterize polarizations. Inelastic helium time-of-flight measurements show phonons with mixed longitudinal and shear-vertical displacements along both the $<\bar{1}00>$, $\overline{\Gamma X}$ and $<\overline{11}0>$, $\overline{\Gamma M}$ symmetry axes over the entire first surface Brillouin zone. Force constants calculated for bulk Nb, Nb(100), and the (3 × 1)-O Nb(100) reconstruction indicate much stronger responses from the oxide surface, particularly for the top few layers of niobium and oxygen atoms. Many of the strengthened bonds at the surface create the characteristic ladder structure, which passivates and stabilizes the surface. These

results represent, to our knowledge, the first phonon dispersion data for the oxide surface and the first ab initio calculation of the oxide's surface phonons. This study supplies critical information for the further development of advanced materials for superconducting radiofrequency cavities.

4.1 Introduction

Particle accelerators are used in a wide range of disciplines, including high-energy particle physics, chemistry, free-electron laser (FEL) science, and materials science, as well as in medical and industrial applications.[37,71] High-energy accelerators propagate large, radiofrequency (RF) electromagnetic fields within superconducting RF (SRF) cavities to generate and control beams of charged particles.[72] These RF fields, however, only penetrate through the first ~100 nm of the cavity surface: SRF cavity performance is controlled by the chemistry and quality of the surface.[33] To lower RF surface resistance (R_s), minimize power loss, and optimize performance, the surface preparation of the SRF cavity must be designed and implemented carefully.

Oxidized niobium surfaces are the current industry standard for SRF cavities. Nb has the highest critical temperature of elemental superconductors (T_c = 9.3 K) and has low RF surface resistance at operating temperatures of about 2 K.[30,32,38,73] Additionally, Nb is thermally conductive and malleable; it can be cooled effectively and formed into SRF cavity shapes.[30,74] High-energy particle accelerator facilities, such as those at Fermi National Accelerator Lab and the European Council for Nuclear Research (CERN), require a large series of SRF cavities to produce intense and accelerated beams—these series are up to tens of km in length.[74–76] Due to their extreme size and an operational temperature (~2 K) below helium's boiling point (4.2 K), the accelerators require extremely costly cryocooling systems, maintenance facilities, and staff.[32,77] Further developments in cavity surface preparation techniques, and even new surface

materials, are needed to improve accelerator performance, raise operating temperatures, and lower operational costs.[32,35,37]

Nb has a strong affinity for oxygen. When exposed to air, Nb's surface forms an oxide layer that may be altered by temperature treatments but will return persistently, implying that Nb components in accelerators are covered by an oxide layer.[47,48] Due to the penetration depth of RF fields, changes in the oxide significantly affect the chemistry of SRF cavity treatments and resulting cavity performance.[33] To gain a thorough and accurate understanding of the interfacial mechanisms driving the performance and development of SRF cavities, we first must investigate the chemistry, structure, and dynamics of oxidized Nb surfaces. The structures of the oxides formed on Nb(100), Nb(110), Nb(111), and polycrystalline Nb have been well characterized, especially at low temperatures.[48,49,51–54,56,68,78–81] Very recently, helium atom scattering (HAS) and Auger electron spectroscopy (AES) were used to characterize the evolution of the oxide surface at elevated temperatures, showing that the (3 × 1)-O reconstruction of the Nb(100) surface is stable up to at least 1130 K.[82] However, oxide surface dynamics on this material have not yet been reported. The (3 × 1)-O Nb(100) surface provides an ideal system to begin investigating the chemistry of Nb oxide surfaces, and this study of the surface's phonon band structure provides information needed to refine current and develop new materials for SRF cavities.

Atomic and molecular beam scattering have been used to investigate the structure and vibrational dynamics of surfaces since the 1920's.[83] Supersonic He beams are suited to study surfaces due to their lack of penetration into the bulk, inertness, and unusually narrow velocity distributions.[3,4,22,61,84] He atoms' momentum and energy are well matched to those of surface phonons, giving HAS a unique ability to measure and resolve low-energy phonon

modes.[3,4,21,22,61,84,85] These modes, particularly the Rayleigh mode, are sensitive to changes in surface interatomic forces and bonding.[2] In previous studies, the phonon dispersions of bulk Nb and the bare Nb(100) surface were studied with neutron and He atom scattering, respectively, as well as fit to lattice dynamical calculations.[60,86,87] Neutron scattering revealed unusual phonon anomalies for bulk Nb modes along high-symmetry directions.[60,86–89] These phonon dispersion curves were best fit by a model which includes electronic degrees of freedom, indicating that the anomalies are caused by electron-phonon coupling.[60] Additionally, Kohn anomalies along low-symmetry directions also point to electron-phonon interactions.[88,89] The previous HAS study of Nb(100) surface modes shows no such anomalies, but measurements were confined to the first half of the Brillouin zone (BZ) due to experimental limitations. Furthermore, the discrepancy between the force-constant model used and the experimental data prompted the authors to conclude that a first-principles theoretical approach would be needed to describe the surface accurately.[60]

Unlike for insulators, the interaction between scattered He atoms and the conduction electrons in a metal must play a large role in any successful theoretical model. The He-surface potential is softened relative to that of ionic crystals, while energy exchange with surface phonons is mediated by surface electrons.[2] Density-functional theory (DFT) is a first-principles approach that can create a lattice-dynamical model that includes the role of free electrons in interatomic forces.[2] By reframing the quantum many-body problem into an auxiliary system of independent electrons interacting in an effective potential, while treating the atomic nuclei classically, calculating the dynamical matrix and surface phonon dispersions for the (3×1)-O reconstruction of the Nb(100) surface becomes feasible.[90] In addition, DFT can provide ab initio estimates to quantify the extent of the electron-phonon interaction for a given phonon mode,

which correlates directly with the intensity of inelastically scattered He for that phonon.[2]

This combined HAS and DFT study investigates the phonon band structure of the (3 × 1)-O Nb(100) reconstruction, in addition to the band structures of bulk Nb and the bare Nb(100) surface. The first-principles description of the surface phonon dispersion curves makes clear how the oxide affects phonon polarizations and interatomic forces, and it contributes to a fundamental, chemical understanding of the crystalline and polycrystalline oxidized Nb surfaces. This study provides needed atomic-scale information to the wider SRF community and aids the development of materials for Nb SRF cavities.

4.2 Experimental

4.2.1 Helium Atom Scattering

We performed measurements with an ultra-high vacuum (UHV) HAS apparatus that provided high angular and energy resolution. A brief overview of the instrument is included here but has been reported in detail elsewhere.[63] There are three main regions of the HAS instrument: a differentially pumped beam source, a sample chamber, and a differentially pumped, rotatable detector arm. The He beam was generated by expansion through a 15 μm nozzle that was cooled by a closed-cycle He refrigerator. After passing through a skimmer, the beam was modulated by a mechanical chopper before colliding with the surface. The resulting supersonic He beam was nearly monoenergetic ($\Delta v/v \leq 1\%$) and hit the 1 cm sample with an approximately 4 mm spot size. A triply differentially pumped, computer-controlled, rotatable detector arm collected the reflected He atoms. The atoms were ionized by electron bombardment, filtered using a quadrupole mass spectrometer, and detected with an electron multiplier followed by pulse counting electronics. A total He flight path of 1.070 m was used to maximize intensity and

resolution. Chopper-to-crystal distance was 0.500 m, with a crystal-to-ionizer distance of 0.571 m.

We took elastic diffraction data with a beam modulated by the chopper in a square-wave pattern, with a 50% duty cycle. Angular distributions were obtained by rotating the detector at 0.2° increments while holding the incident angle and energy fixed, with an overall instrument angular resolution of 0.45°. We collected elastic and inelastic time-of-flight (TOF) spectra by chopping the beam with either a 50% duty cycle for cross-correlation analysis—a pseudorandom 511-bit sequence of openings in the chopper wheel that increases signal-to-noise ratios—or with a single-slit, 1% duty cycle pattern.[91] TOF spectra often were taken multiple times under identical conditions and added to form composite spectra with increased signal-to-noise.

The Nb(100) crystal was mounted on a six-axis manipulator within the HAS instrument's sample chamber. This manipulator afforded precise control over the incident angle, θ_i, azimuthal angle, ϕ, and tilt, χ, with respect to the scattering plane. Electron bombardment heating and a closed-cycle He refrigerator modulated the sample temperature within a range of 300 K to 1900 K. Surface Preparation Laboratory (Netherlands) provided the Nb(100) sample (99.99% purity, ~0.1° cut accuracy), which we then cleaned in the HAS instrument by cycles of annealing at and flashing to 1900 K, in addition to sputtering with 500 eV Ne^+ ions (3 μA maximum). Impurities identified by in-situ AES were C, B, S, and N; these were removed by the combination of annealing, flashing, and sputtering. We continued the cleaning cycles until only Nb and O were present on the surface, as confirmed by AES, and until the surface was smooth enough for high-intensity He diffraction. Due to the annealing, flashing, and sputtering process described above, the (3×1)-oxide reconstruction forms naturally and spontaneously. The creation of the oxide has been well documented: when a Nb crystal is annealed or flashed above 600 K, the native, thick,

Nb_2O_5 layer reduces to NbO_2 and then NbO.[92–94] Annealing Nb(100) between 870 K and 1970 K causes the (3 × 1)-O ladder structure to form spontaneously;[49] bare Nb is not seen with anneal temperatures lower than 2500 K.[49,52] We confirmed the presence of the ladder structure through AES peak ratios, LEED spectra, and HAS. During data collection, the Nb sample periodically was flashed to about 1200 K to eliminate unwanted surface adsorbates.

4.3.2 Density-Functional Theory

We calculated electron and phonon properties of Nb and NbO with DFT using the open-source plane-wave software JDFTx.[95,96] The electronic states for the outer electrons of Nb ($4p^6 5s^2 4d^3$) and O ($2s^2 2p^4$) were calculated by treating exchange and correlation effects with the PBE-sol functional and applying the corresponding ultrasoft pseudopotentials parametrized for the functional.[97,98] All DFT calculations presented in this paper employ an electronic cutoff energy of 20 hartree, with a 200 hartree charge density cutoff. Electronic properties for bulk BCC niobium were calculated by sampling 18^3 k-points in the Brillouin zone and solving for 15 bands, with electron occupancies corresponding to a Fermi function at an effective electron temperature of 5 mH. With these parameters, we calculated the lattice constant of Nb to be 3.27 Å, in excellent agreement with the experimental measurement of 3.29 Å.[52] The surface calculations for cubic Nb(100) and (3 × 1)-O Nb(100) sampled 12 × 12 × 1 and 3 × 9 × 1 k-points in the respective Brillouin zones, and electronic occupancies for both systems were calculated using an effective electron temperature of 20 mH. A 10-layer slab was used to calculate the properties of Nb(100) and an asymmetric 8-layer slab was used for (3 × 1)-O Nb(100), with the oxide on one surface and bare Nb(100) on the opposite surface. Using this asymmetric cell, we tested the bare Nb surface of the (3 × 1)-O Nb(100) system against the bare 10-layer Nb(100) slab to ensure that relevant properties converged. To model the experimental

oxide surface, whose structure is dominated by a 3 × 1 motif, we introduced surface lattice vectors that are 3 × 1 lattice constants across and allowed the surface vectors of the slab to relax. The surface lattice vectors of the 8 layer (3 × 1)-O Nb(100) slab relaxed between the lattice constants of bulk Nb (3.29 Å) and NbO (2.99 Å); specifically, to values of 3.21 Å and 3.14 Å for the threefold and onefold vectors, respectively.[68] The resulting phonon frequencies of the (3 × 1)-O Nb(100) slab are real-valued, ensuring that our finite system is dynamically stable. To accommodate the minor differences between the DFT and experimental lattice vectors, the reciprocal space plots reported in this paper that compare theory to experiment reference the Brillouin zone in lattice units.

We calculated phonon properties using the finite-difference supercell method, perturbing atoms by ~0.4–0.5 a_0 to calculate the real space interatomic force constant matrix directly.[99] Adequate supercell sizes were 6 × 6 × 6 for bulk BCC niobium, 3 × 3 × 1 for cubic Nb(100), and 1 × 3 × 1 for (3 × 1)-O Nb(100). Properties of the coupled electron-phonon systems required fine k-space samples for accurate calculations of the scattering integrals; we calculated phonon linewidths by transforming into a maximally localized Wannier function (MLWF) basis to sample the Brillouin zone with the Monte Carlo method.[100]

4.5 Theoretical Background

Niobium is a conventional superconductor.[73] Its properties can be described reasonably well within the Bardeen-Cooper-Schrieffer (BCS) theory of superconductivity, and its electrons condense into Cooper pairs via the electron-phonon coupling (EPC) mechanism.[101] Theoretical predictions are improved by applying the higher order Eliashberg theory within a DFT framework to calculate EPC explicitly.[99,102,103] By transforming into an MLWF basis, we

calculate directly how electrons couple to various lattice distortions to extract the quantities relevant in predicting inelastic He-scattering rates.[104] Specifically, we employ perturbation theory and calculate the overlap of the perturbing electron-ion potential between the unperturbed electronic states in order to calculate explicitly the electron-phonon matrix elements within DFT:[105]

$$g^{\boldsymbol{q}\nu}_{n\boldsymbol{k},\, n'\boldsymbol{k}+\boldsymbol{q}} = \left(\frac{\hbar}{2M\omega_{\boldsymbol{q}\nu}}\right)^{\frac{1}{2}} \langle \psi_{n',\boldsymbol{k}+\boldsymbol{q}} \left| \frac{dV^{e-i}}{du_{\boldsymbol{q}\nu}} \cdot \hat{\epsilon}_{\boldsymbol{q}\nu} \right| \psi_{\boldsymbol{q}\nu} \rangle, \tag{4.1}$$

where $u_{\boldsymbol{q}\nu}$ and $\omega_{\boldsymbol{q}\nu}$ are the atomic displacements and frequencies, respectively, for the phonon mode ν with crystal momentum $\boldsymbol{q}$ and polarization vector $\hat{\epsilon}_{\boldsymbol{q}\nu}$, and M is the ion mass.

The above matrix elements connect to inelastic He-scattering rates through the phonon linewidths and the dimensionless EPC constants. Specifically, the phonon linewidths, or equivalently, the inverse phonon lifetimes, are defined as:[106]

$$\gamma_{\boldsymbol{q}\nu} = 2\pi\omega_{\boldsymbol{q}\nu} \sum_{n,n'} \int \frac{d^3k}{(2\pi)^3} \left| g^{\boldsymbol{q}\nu}_{n\boldsymbol{k},n'\boldsymbol{k}+\boldsymbol{q}} \right|^2 \delta\left(e_{\boldsymbol{q},n} - e_F\right) \delta\left(e_{\boldsymbol{k}+\boldsymbol{q},n'} - e_F\right). \tag{4.2}$$

These linewidths then determine the dimensionless EPC constants,

$$\lambda_{\boldsymbol{q}\nu} = \frac{\gamma_{\boldsymbol{q}\nu}}{\pi\hbar N(e_F)\omega^2_{\boldsymbol{q}\nu}}, \tag{4.3}$$

where $N(e_F)$ denotes the electronic density of states at the Fermi level.

Finally, to estimate HAS signal intensities, we follow the theoretical frame of Benedek et al. and estimate the inelastic scattering probability to be proportional to $\lambda_{\boldsymbol{q}\nu}$, but instead of using an approximate analytic form for the surface electron-phonon matrix elements, we calculate the matrix elements ab initio directly in an MLWF basis using DFT.[14,107–110] In order to better probe the surface-specific phonon characteristics measured by HAS, we project the mode-selected EPC constants onto the z-displacements of the corresponding phonon polarization vector, while

including the exponential decay of the He wave functions into the material, and define the surface-projected EPC constants as:

$$\bar{\lambda}_{\boldsymbol{Q}\nu} \propto \sum_{\boldsymbol{Q}\nu,\kappa} |e^{\alpha=z}(\boldsymbol{Q}\nu)|^2 \, \lambda_{\boldsymbol{Q}\nu} \, exp(-\beta z_\kappa) \, \delta\left(E - \hbar\omega_{\boldsymbol{Q}\nu}\right). \tag{4.4}$$

Here, κ labels the atoms, z represents the atoms' distance beneath the surface, β is the helium decay softness parameter, and E is the energy transfer of the He atom. The above expression is written as a proportionality because here we do not include factors, such as additional matrix elements, that are considered to be energy- and wavevector-independent.[14,108,109,111] Following standard distorted-wave Born approximations of atom-surface potentials, we estimate the softness parameter, β, for Nb(100) to be ~2.1 Å^{-1}, which falls within the typical range expected for metals.[2,112]

4.4 Results and Discussion

He diffraction scans from the (3 × 1)-O Nb(100) surface are shown in Figure 4.1. Figure 1(a) is a representative angular scan along the <$\bar{1}$00>, $\overline{\Gamma X}$ azimuthal direction, while Figure 1(b) is a scan along the <$\overline{11}$0>, $\overline{\Gamma M}$ direction with an inset diagram of the reciprocal surface lattice vectors. We took both scans with a cold He beam (E_i = 21 meV) and slightly elevated surface temperatures (T_S = 360 K and 410 K for Figures 1(a) and 1(b), respectively). The scan in Figure 1(a) was taken at an incident angle of θ_i = 34.8°; we confirmed surface reproducibility by taking repeated diffraction scans at T_S = 360 K after flashing the crystal to 1200 K. The specular peak ($\theta_i = \theta_f$) at ΔK = 0 is approximately 2.6 times more intense than the next largest, first-order (0$\bar{1}$) diffraction

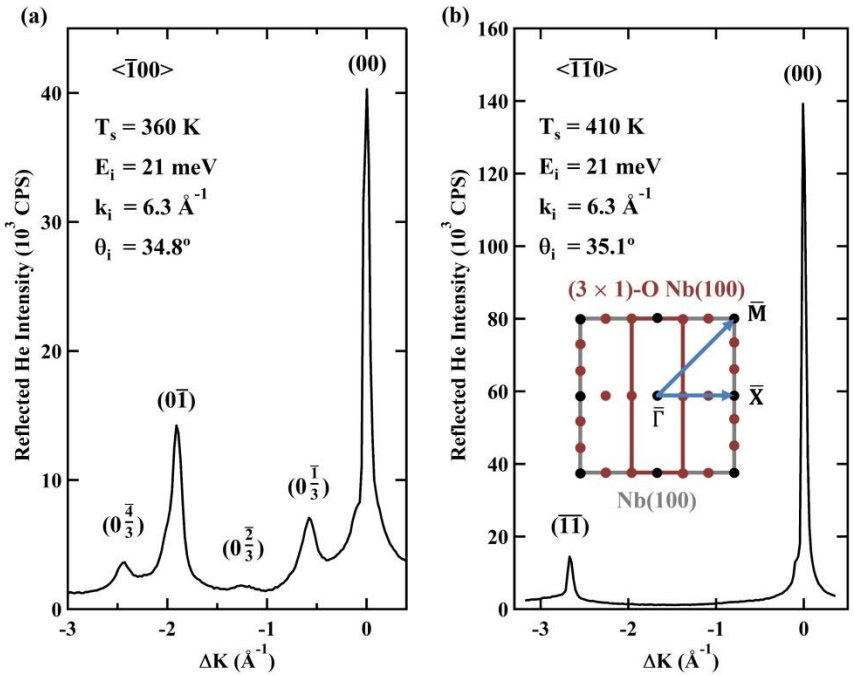

Figure 4.1: Representative He atom diffraction spectra for the (3 × 1)-O Nb(100) surface along the (a) <$\bar{1}$00> and (b) <$\overline{11}$0> symmetry axes, with the inset diagram in (b) showing the reciprocal surface lattice vectors. The specular (00) peak is visible in both directions, while the oxide structure can be seen in (a) along the <$\bar{1}$00> axis, with fractional peak notation corresponding to the (3 × 1)-O structure. The <$\overline{11}$0> axis in (b) shows the underlying ($\overline{11}$) Nb(100) lattice peak.

peak at $\Delta K = -1.9$ Å^{-1} (θ_f = 15.8°). When compared with a scan of bare Nb(100), the larger first- to zeroth-order peak intensity ratio indicates that the oxide structure has a higher surface corrugation.[21] In particular, we note that the first-order diffraction peak intensity is within the same order of magnitude as the specular intensity, while the first-order diffraction intensity observed for the bare Nb(100) surface is over two orders of magnitude less than the specular intensity.[60] Each peak occurs when the Bragg equation holds true; that is, when

$$\Delta K = k_i(\sin\theta_i - \sin\theta_f) = G_{mn}, \tag{4.5}$$

where the surface-parallel component of the He wavevector k_i changes by ΔK; the initial and final scattering angles, relative to surface normal, are θ_i and θ_f, respectively; and G_{mn} is a linear combination of reciprocal surface lattice vectors.

Three additional diffraction peaks are visible in the angular scan of the <$\bar{1}$00>, $\overline{\Gamma X}$ azimuthal direction, all of which correspond to the (3 × 1)-O ladder structure. The $\left(0\frac{\bar{1}}{3}\right)$ peak, at $\Delta K = -0.6$ Å^{-1} (θ_f = 28.7°), is approximately one-third of the way between the (00) and ($0\bar{1}$) peaks. Similarly, the $\left(0\frac{\bar{2}}{3}\right)$ peak (ΔK = -1.2 Å^{-1}, θ_f = 22.0°) is two-thirds of the way between the primary peaks, while the $\left(0\frac{\bar{4}}{3}\right)$ peak (ΔK = -2.4 Å^{-1}, θ_f = 10.8°) is past the ($0\bar{1}$) peak by one-third of that distance. The visibility of all three superlattice peaks shows the excellent surface order of the sample and the minimal scattered He background intensity measured by the detector.

The angular scan in Figure 4.1(b) was taken at an incident angle of θ_i = 35.1° in the <$\bar{1}\bar{1}$0>, $\overline{\Gamma M}$ direction. Since the (3 × 1)-O reconstruction does not affect atomic spacing along this azimuthal direction, only primary lattice diffraction peaks are seen. The specular peak at ΔK = 0 is much larger than the first-order, ($\bar{1}\bar{1}$) diffraction peak (ΔK = -2.7 Å^{-1}, θ_f = 8.9°), indicating that the surface is corrugated slightly less along this axis than along the $\overline{\Gamma X}$ axis.[21]

For inelastic, in-plane scattering, the conservation of energy and crystal momentum dictates possible scattering angles and energies. For a given beam with incident energy E_i, wavevector k_i, and angle θ_i, possible final conditions (angle θ_f, wavevector k_f, and energy E_f) must satisfy the equation,

$$\Delta K = k_f \sin\theta_f - k_i \sin\theta_i = G_{mn} + Q, \tag{4.6}$$

where G_{mn} again is a linear combination of reciprocal surface lattice vectors and Q is the two-

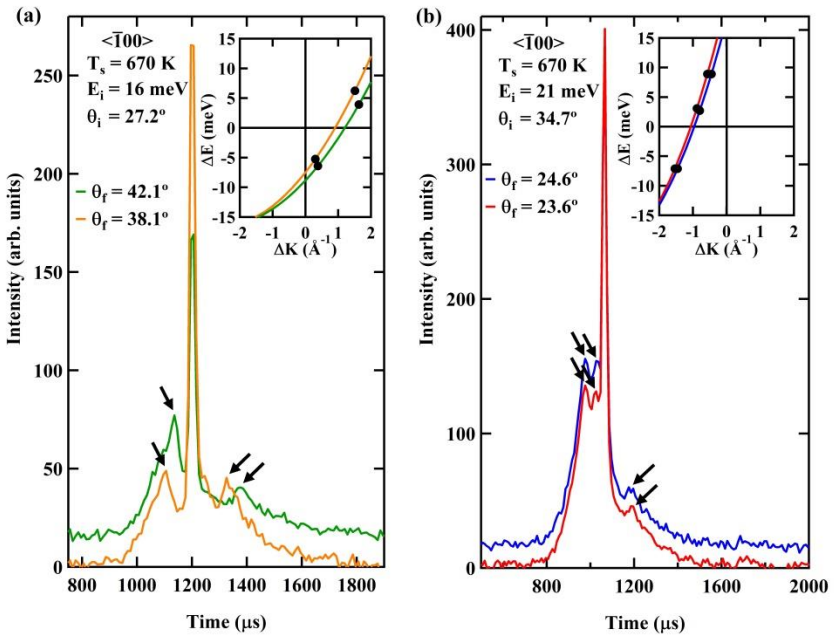

Figure 4.2: Representative cross-correlation TOF spectra for the (3 × 1)-O Nb(100) surface along the <$\bar{1}$00> symmetry axis, under different incident and final conditions. Data in (a) were taken with a 16 meV incident He beam, while data in (b) were taken with a 21 meV incident beam. Phonon peaks are designated by black arrows, with insets showing representative scan curves for each spectrum. Black dots indicate phonon peak positions; ΔE is the energy gained or lost by the He beam.

dimensional wavevector for a phonon with energy $\hbar\omega$. By substituting relevant energies (Equation 4.7) and rearranging, the scan curve indicating accessible phonons can be extracted (Equation 4.8):

$$\Delta E = E_f - E_i = \frac{\hbar^2 k_f^2}{2m} - \frac{\hbar^2 k_i^2}{2m} = \hbar\omega(Q); \tag{4.7}$$

$$\frac{\Delta E}{E_i} = \frac{\left(\sin\theta_i - \frac{\Delta K}{k_i}\right)^2}{\sin^2\theta_f} - 1. \tag{4.8}$$

Systematically varying incident beam energy and angle while capturing TOF spectra moves the scan curve across the surface Brillouin zone (SBZ) and maps out surface phonon resonances.

Figure 4.2 shows examples of cross-correlation TOF spectra measured along the <$\bar{1}$00>, $\overline{\Gamma X}$ axis. Each spectrum was taken under specific incident and final conditions that maximized

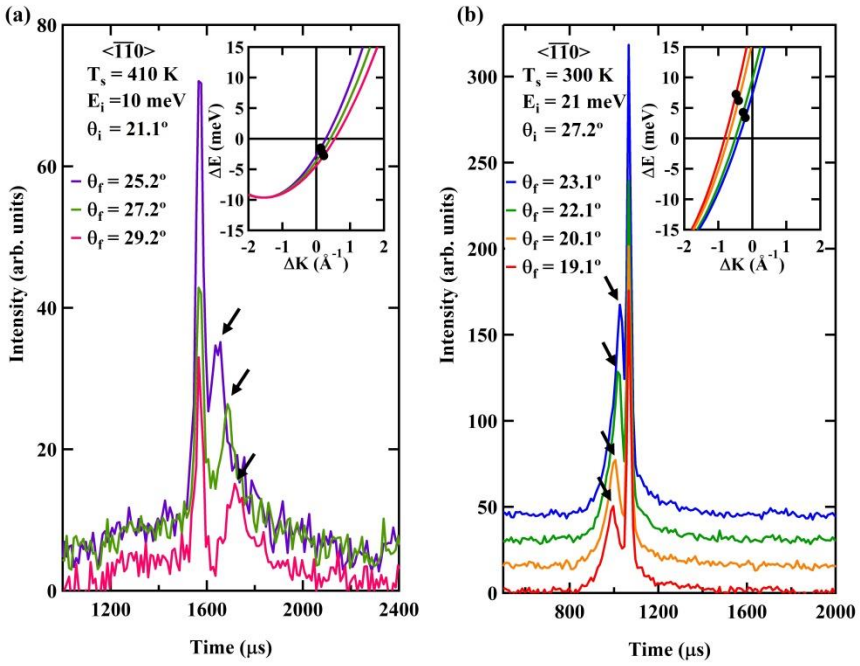

Figure 4.3: Representative cross-correlation TOF spectra for the (3 × 1)-O Nb(100) surface along the <$\bar{1}$10> symmetry axis. Data in (a) were taken with a 10 meV incident He beam, while data in (b) were taken with a 21 meV incident beam. Phonon peaks are designated by black arrows; insets show representative scan curves for each spectrum with black dots indicating phonon peak positions. ΔE is the energy gained or lost by the He beam.

intensity and resolution. We explored various surface temperatures, with T_S = 670 K yielding the best results: for this axis, all spectra were taken with cross-correlation chopping at T_S = 670 K. Figure 4.2(a) and Figure 4.2(b) were taken with incident energies E_i = 16 meV and 21 meV and angles θ_i = 27.2° and 34.7°, respectively. The dominant peak in each spectrum is elastic, where $E_i = E_f$, and was used to calculate incident beam energy. Subsidiary peaks—indicated by black arrows—are phonon modes, with peaks to the left of elastic corresponding to surface phonon annihilation (the He beam gains energy), and peaks to the right corresponding to surface phonon creation (the He beam loses energy). We identified the position of the top of each peak by fitting

a given spectrum with multiple Gaussian functions and extracting the function centers. That time then was

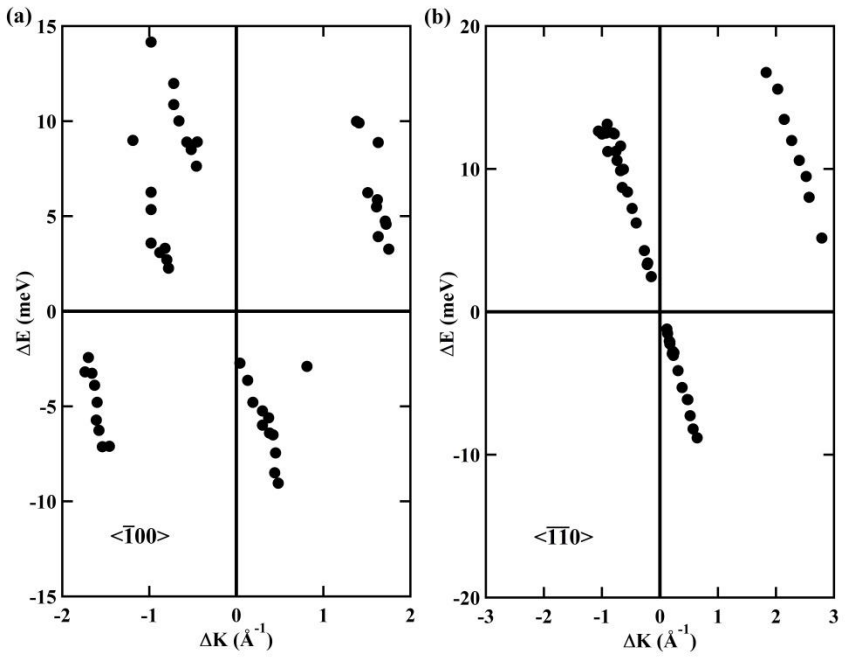

Figure 4.4: Extended dispersion plots along the (a) <$\bar{1}$00> and (b) <$\overline{11}$0> symmetry axes. Each point corresponds with the center of a phonon peak from a TOF spectrum. These values are as measured by the He beam, where ΔE indicates energy gained or lost by the He beam.

correlated with a specific ΔE and ΔK for the He beam and plotted, along with the corresponding scan curve, in Figure 4.2's insets.

Figure 4.3 shows similar TOF spectra but taken along the <$\overline{11}$0>, $\overline{\Gamma M}$ axis. Along this axis, we held the surface temperature at either T_S = 300 K or 410 K, depending on the scan. Additionally, a few phonon modes identified in this direction were measured using a single-shot chopping pattern for increased resolution, though Figure 3 contains cross-correlation data. Figure 4.3(a) was taken with T_S = 410 K, E_i = 10 meV, and θ_i = 21.1°, while T_S = 300 K, E_i = 21 meV, and θ_i = 27.2° for Figure 3(b). Phonons are identified with black arrows and we obtained peak

positions in the same manner as for Figure 4.2. Phonon positions in the SBZ with corresponding scan curves are shown in the figure insets.

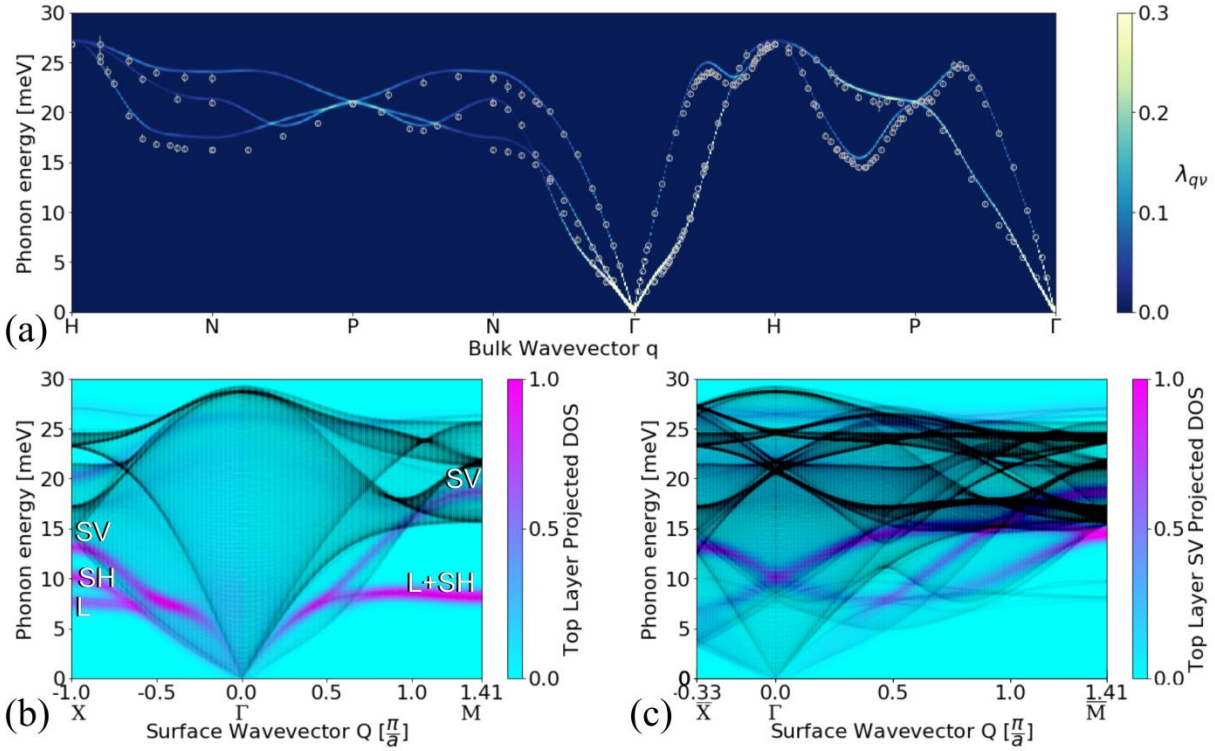

Figure 4.5: (a) Bulk phonon dispersions calculated for Nb along high-symmetry paths of the BCC Brillouin zone, where each mode's EPC strength is indicated by its brightness level and brighter colors correspond to stronger coupling. Neutron scattering data from literature (white circles) are overlaid on the calculations for comparison.[86] Surface phonons along symmetry directions $\overline{\Gamma X}$ and $\overline{\Gamma M}$ for (b) cubic Nb(100) and for (c) (3 × 1)-folded Nb(100). Black lines represent phonon dispersions calculated for an effective 130-layer slab of Nb(100). The colormaps display the surface phonon density of states (DOS) projected onto the top layer of atoms, and surface resonances are labeled for the shear-vertical (SV), shear-horizontal (SH), or longitudinal (L) in (b). The (3 × 1)-folded Nb(100) colormap in (c) displays only the SV mode to demonstrate the BZ folding process more clearly.

All measured phonon peak positions are shown in Figure 4.4, with Figure 4.4(a) showing data taken along the $\overline{\Gamma X}$ axis and Figure 4.4(b) along the $\overline{\Gamma M}$ axis. As in Figures 4.2 and 4.3, these extended SBZs are as measured by the He beam, with ΔE indicating energy gained or lost

by the beam. Multiple phonon resonances are seen in both axes and will be discussed below with DFT results.

Figure 4.5(a) shows the DFT-calculated phonon modes of bulk Nb along the BCC Brillouin zone symmetry directions (colormap) compared with neutron scattering data from literature (white circles).[86] The DFT-calculated modes reproduce previously calculated and measured results, confirming the accuracy of the method used.[60,86] Phonon anomalies indicated by the change in slope of the bottom-most resonances along the ΓH and ΓN directions are observed, as are dips in the higher resonance along ΓH and lower resonance along HP, and a resonance crossing near H along ΓH.[60,87] The bulk phonon modes are colored by their respective EPC constant strengths, $\lambda_{\boldsymbol{q}\nu}$: by taking advantage of the MLWF basis, we are able to track the EPC of bulk niobium throughout the Brillouin zone. The strongest coupling is seen near the Γ point for all resonances, which corresponds with lower phonon energies.

Next, we identified both surface-projected bulk phonon modes and surface modes for an effective 130-layer slab of Nb(100) by beginning with a 10-layer slab and inserting 120 bulk layers into its dynamical matrix. These results are shown in Figure 4.5(b) along symmetry directions $\bar{\Gamma}\bar{X}$ and $\bar{\Gamma}\bar{M}$ and are overlaid with a colormap of the top-layer surface phonon density of states (DOS). By examining the atomic displacements associated with the surface phonon modes, we identify polarizations and find that the longitudinal (L) and shear-horizontal (SH) modes dip below the shear-vertical (SV) mode and the bulk-projected band along both symmetry directions. The highest surface DOS is seen in the L+SH mode near $\bar{M}$. In Figure 4.5(c), we folded the effective 130-layer slab of cubic Nb(100) to represent a (3 × 1)-folded BZ equivalent to the BZ of (3 × 1)-O Nb(100). The folded BZ displays more apparent resonances at a given wavevector, both surface-projected bulk and strictly surface, as a result of the folding. For

example, what once were acoustic modes can now, after folding, appear as optical modes. This process is illustrated in Figure 4.5(c): considering only the top-layer SV projected DOS for clarity, the DOS now disperses to higher phonon energies at shorter wavevectors. Accordingly, surface modes are folded to near the middle of the surface-projected bulk band, and the SV mode in particular is translated to about 10 meV at

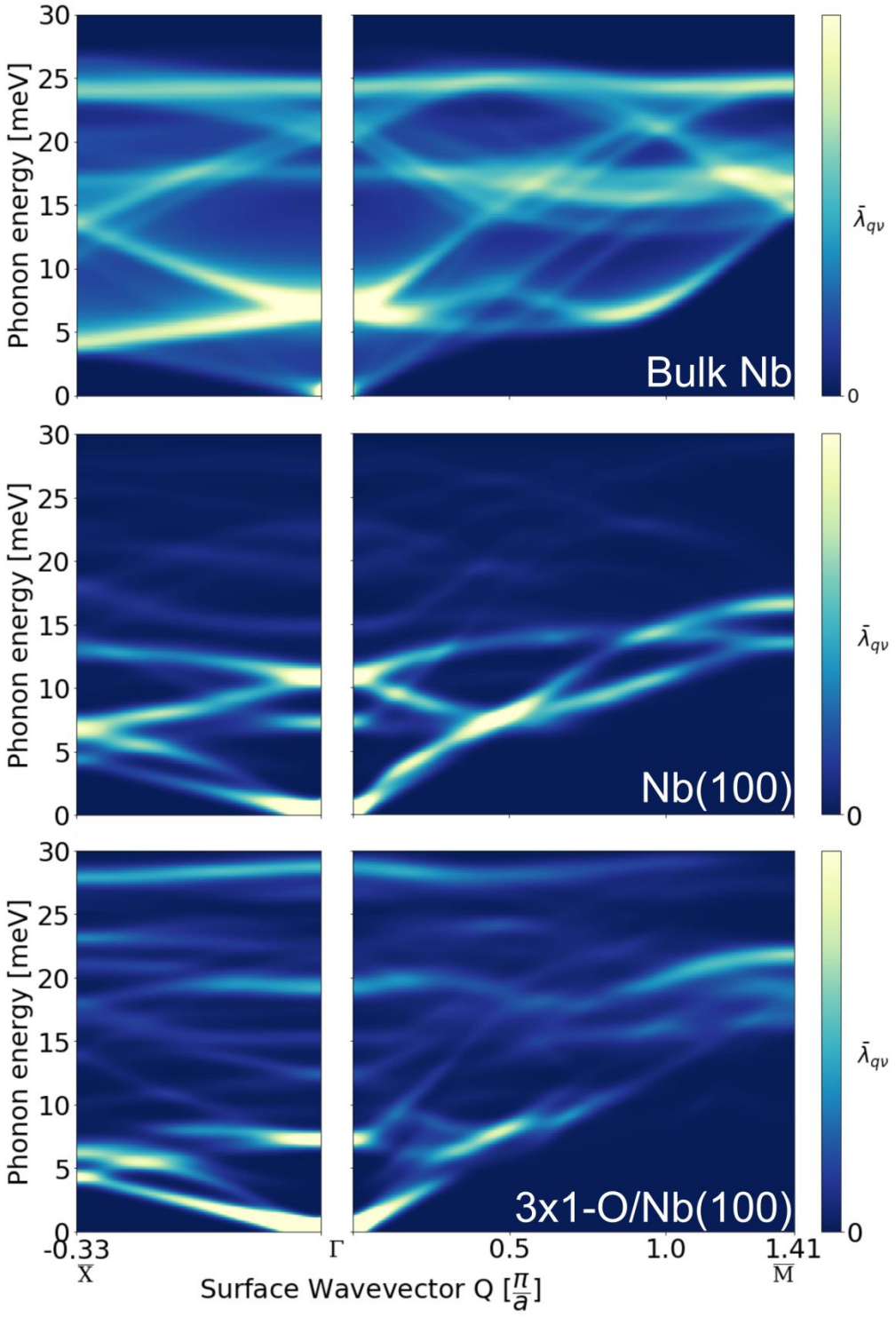

Figure 4.6: Surface EPC strengths along SBZ symmetry directions $\overline{\Gamma X}$ (left column) and $\overline{\Gamma M}$ (right column), projected from bulk Nb (top row) onto the SBZ and projected onto the exponentially weighted *z*-displacements using Equation 4 for (middle row) the bare Nb(100)

surface and (bottom row) the (3 × 1)-O Nb(100) surface. Coupling strengths are indicated by brightness level, with brighter colors corresponding to stronger coupling.

the $\bar{\Gamma}$-point.

Figure 4.6 shows the results from our calculated EPC strengths for bulk Nb projected on the SBZ, along with the coupling strengths for the bare Nb(100) and (3 × 1)-O Nb(100) surfaces. Values of surface EPC strengths are projected onto exponentially weighted z-displacements (see Equation 4.4), as these are what can be seen most readily with HAS. The first BZ for both the bare and (3 × 1)-O surfaces are folded to correspond with the ladder structure and allow for direct comparison. The EPC for the Nb(100) surface is pronounced near the $\bar{\Gamma}$-point at low energies and near 11 meV, higher than it is for bulk Nb projected on the SBZ. Multiple resonances are seen along both directions for the Nb(100), though most of the EPC strength is concentrated below 16 meV.

The electron-phonon interaction strength becomes much more dispersed for the oxide surface, with multiple new resonances appearing at higher phonon energies due to the addition of the less massive O atoms. The resonances at $\bar{\Gamma}$, approximately 11 meV for Nb(100), move higher, to about 13 meV, and lose significant relative strength for the oxide. The resonance at 7 meV appears more intense for the oxide, as are the lowest resonances along both symmetry directions.

High-energy, optical modes also appear in the oxide, most notably near 28 meV. However, the strongest couplings for the bare Nb(100) and oxide surfaces are seen in approximately the same locations: in the acoustic modes near the $\bar{\Gamma}$ point for 0–3 meV; near the $\bar{X}$ point near 5 meV; and near 0.5 π/a along the $\bar{\Gamma}\bar{M}$ around 7 meV.

When a He atom scatters from a metal, it interacts with the surface electron density. The creation or annihilation of surface phonons occurs through these electrons, intrinsically linking

HAS with EPC strengths.[2] In Figure 4.7, HAS phonon data are overlaid with the calculated dispersion plot for (3 × 1)-O Nb(100), where experimental data points are shown as white dots and

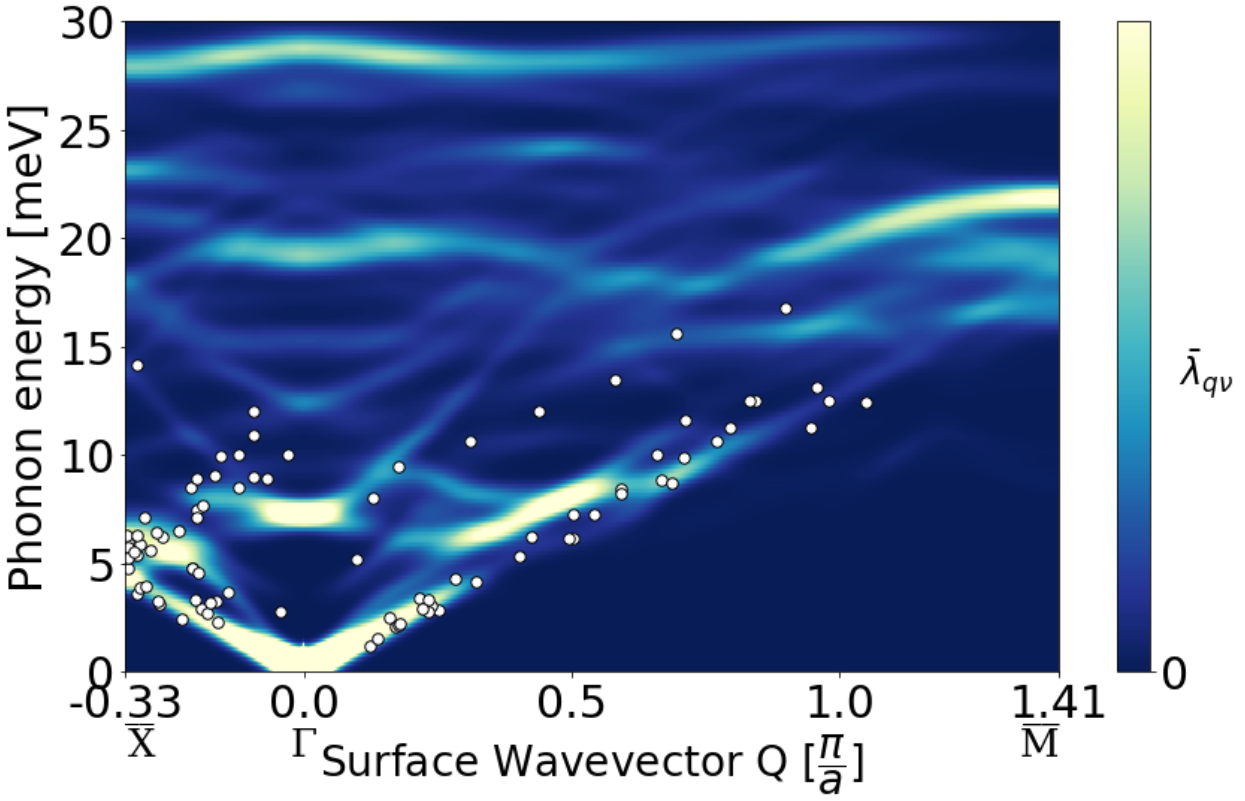

Figure 4.7: Phonons for the (3 × 1)-O Nb(100) surface measured with HAS (white dots), overlaid on DFT-calculated surface electron-phonon coupling strengths projected onto *z*-displacements, using Equation 4. Coupling strengths are indicated by brightness level, with brighter colors corresponding to stronger coupling. HAS data and theoretical predictions along $\bar{\Gamma}\bar{M}$ were translated back into the first BZ of cubic Nb(100), while the data along $\bar{\Gamma}\bar{X}$ was folded back to the (3 × 1)-folded BZ of the ladder structure.

EPC strength is indicated by brightness. Satisfactory agreement is seen between the experimental and theoretical results and demonstrates the importance of electron-phonon interactions in resonances visible with inelastic He scattering. The density of measured points is a convolution of experimental conditions and available phonon modes—where phonons were more easily resolved, more phonons were measured. The highest density of measured points, near $\bar{X}$ and 6

meV and near 0.25 π/a along $\bar{\Gamma}\bar{\mathrm{M}}$ and 3 meV, corresponds well with the stronger EPC calculated by DFT. Along the $\bar{\Gamma}\bar{\mathrm{X}}$ direction two acoustic modes can be seen with HAS, though their distinction is blurred at higher energies by the folding of the first BZ. The lowest mode is the Raleigh mode while the upper is longitudinal, but as will be seen in Figure 4.8, towards the zone boundary there is a hybridization and mixing of SV and L displacements which blurs this distinction, a common feature of metal surfaces.[113]

There also are two modes measured with HAS along the $\bar{\Gamma}\bar{\mathrm{M}}$ direction, with the lower mode, gain being the Rayleigh mode. By comparing the EPC strengths for Nb(100) and (3 × 1)-O Nb(100) in Figure 4.6, we attribute the upper measured mode primarily to the addition of the oxide on the surface. This corresponds with the trend seen in Figure 4.6, where the oxide disperses EPC, and hence inelastic He-scattering intensity, to higher energies. An anomalous feature can be seen in the lowest longitudinal mode along $\bar{\Gamma}\bar{\mathrm{M}}$, indicating a lattice instability which is often accompanied by a symmetry breaking, and may be related to the oxide reconstruction but requires further analysis.[114]

By comparing our experimental data for the (3 × 1)-O Nb(100) surface with data from literature for the bare, Nb(100) surface, we see changes caused by the oxide reconstruction.[60] Our data and that from Hulpke et al. both show two measured modes along $\bar{\Gamma}\bar{\mathrm{X}}$ and $\bar{\Gamma}\bar{\mathrm{M}}$.[60] Along $\bar{\Gamma}\bar{\mathrm{X}}$, these modes agree between the two surfaces, though our data extends much farther into the first SBZ, limiting the comparison. Along $\bar{\Gamma}\bar{\mathrm{M}}$, however, the high-energy mode is significantly stiffened for the oxide surface. This increase in energy ranges from about 2–4 meV: larger differences are seen closer to $\bar{\Gamma}$, while the difference decreases somewhat as the mode disperses through the BZ. As will be seen in Figure 4.9, the stiffening of the phonon mode corresponds with increased surface force constants for the oxide, and indicates that the oxide stabilizes the

Nb(100) surface. The lower, Rayleigh mode measured along $\overline{\Gamma}\overline{M}$ appears to follow that measured for metallic Nb, but as with the $\overline{\Gamma}\overline{X}$ direction, the data from Hulpke et al. does not extend far into the first SBZ, and we are not

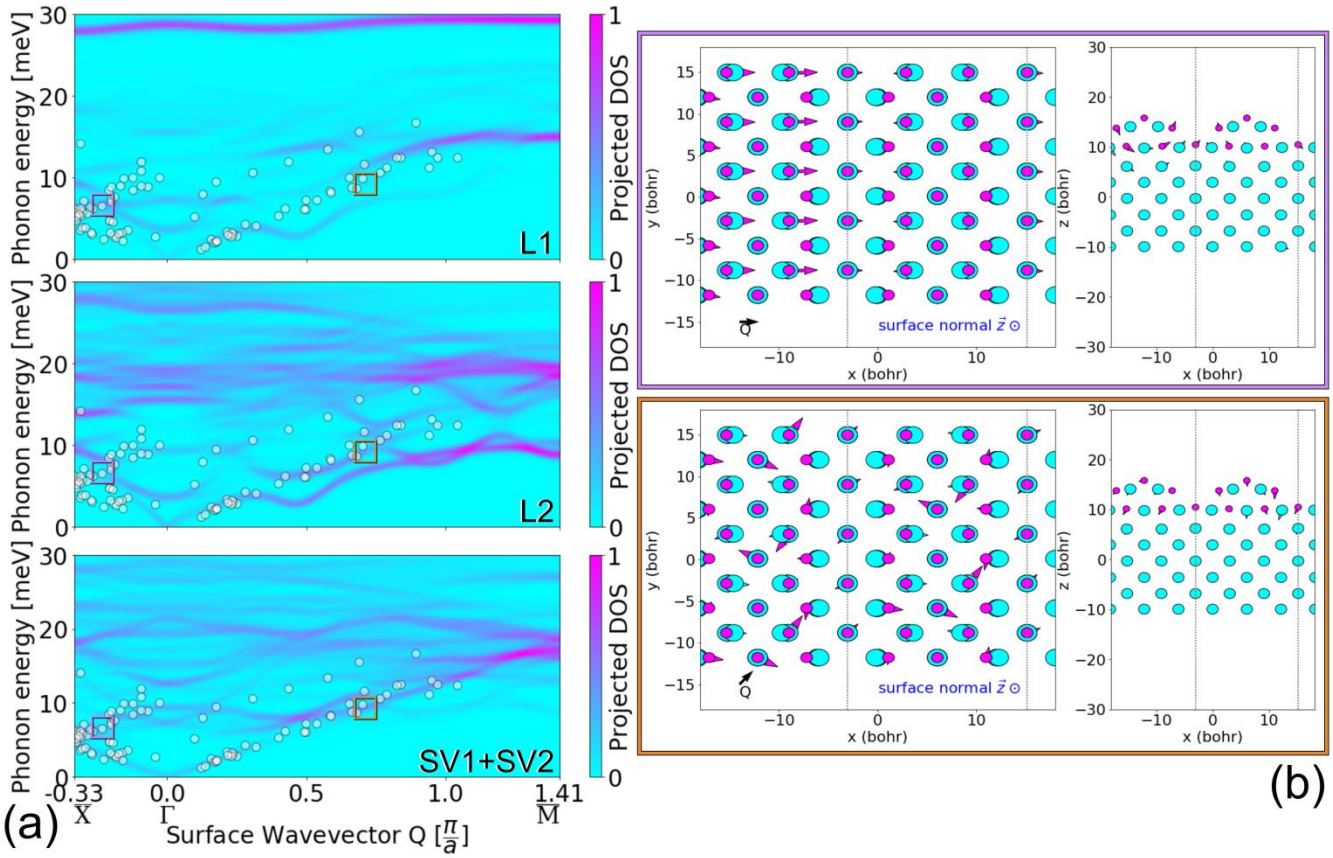

Figure 4.8: Top layer densities of states projected onto the SV or L displacements of the surface atoms of (3 × 1)-O Nb(100); from top to bottom: L displacements from layer 1 (L1) and from layer 2 (L2), and SV displacements from layers 1 and 2 (SV1+SV2), where layer 1 refers to the crest of the oxide and layer 2 denotes the planarly intact layer beneath the crest. Each white circle marks an HAS event (repeated from Figure 7). (b) Atomic displacements of the Nb atoms (larger teal circles) and O atoms (smaller magenta circles) for (3 × 1)-O Nb(100) calculated with DFT corresponding to the two boxed modes highlighted in (a). The displacements in the (upper) violet box correspond to the mode along $\overline{\Gamma}\overline{X}$ at 6.8 meV and the displacements in the (lower) orange box correspond to the mode along $\overline{\Gamma}\overline{M}$ at 9.3 meV. The arrows in (b) indicate directions of the atomic displacements and their relative magnitudes, viewing (left) down along surface normal and viewing (right) along the surface with the surface normal pointing up. The vertical dashed lines in (b) coincide with the troughs in the ladder structure.

able to compare data near the $\bar{M}$ zone edge, though this is where the DFT-calculated Rayleigh wave appears to differ most between the two surfaces in Figure 4.6.[60]

Figure 4.8(a) shows the top layer DOS projected onto the SV or L displacements of (3 × 1)-O Nb(100) surface atoms. This allows us to assign the polarizations to the modes measured by HAS. Along $\bar{\Gamma}\bar{X}$, the lowest measured mode, or the Raleigh mode, is almost entirely SV, while the higher modes are mixed L and SV. Along $\bar{\Gamma}\bar{M}$, both measured modes appear mixed, though the higher mode is primarily L due to second-layer atoms (L2), while the lower mode mixes L1, L2, and SV1+SV2. The high-energy optical mode across the entire SBZ is seen to be almost entirely L due to the top layer of atoms—from the crests of the (3 × 1)-O Nb(100) ladder structure. This mode has the highest DOS for L1, has very little dispersion, and is near the top of the bulk-projected band seen in Figure 4.5(c).

Two specific phonons measured by HAS are examined in Figure 4.8(b): one along $\bar{\Gamma}\bar{X}$ (upper violet box) and one along $\bar{\Gamma}\bar{M}$ (lower orange box). Figure 4.8(b) shows the atomic displacement directions and magnitudes with arrows corresponding to O (smaller magenta circles) or Nb (larger teal circles) atoms, viewed along surface normal and viewed head-on with surface normal pointing up. For both phonons, the O atoms are much more active than the Nb. The phonon in the violet box is primarily L in the first layer of atoms, as indicated both by Figure 4.8(a) and by the direction of the arrows in Figure 8(b). The resonance in the orange box is a hybridization of L and SV, involving L displacements in the second layer of atoms and SV in both the first and second layers.

Figure 4.9 shows the pairwise interatomic force constants for bulk Nb, Nb(100), and (3 × 1)-O Nb(100). The addition of the oxide to the surface causes a significant increase in force constants, even between Nb atoms. The highest force recorded was the force on a Nb atom when

it was perturbed along the surface, which is labeled by a black, five-pointed star and illustrated in Figure 4.9(c). This force is almost twice the highest force seen for the bare Nb(100) surface, indicating that the oxide stabilizes the surface. Another notable feature is the Nb-Nb force increase caused by the oxide, which is labeled by the black, four-pointed star at approximately R = 2.6 Å. This is the surface-parallel force on one of the Nb atoms in the crest of the (3 × 1)-O Nb(100) ladder structure

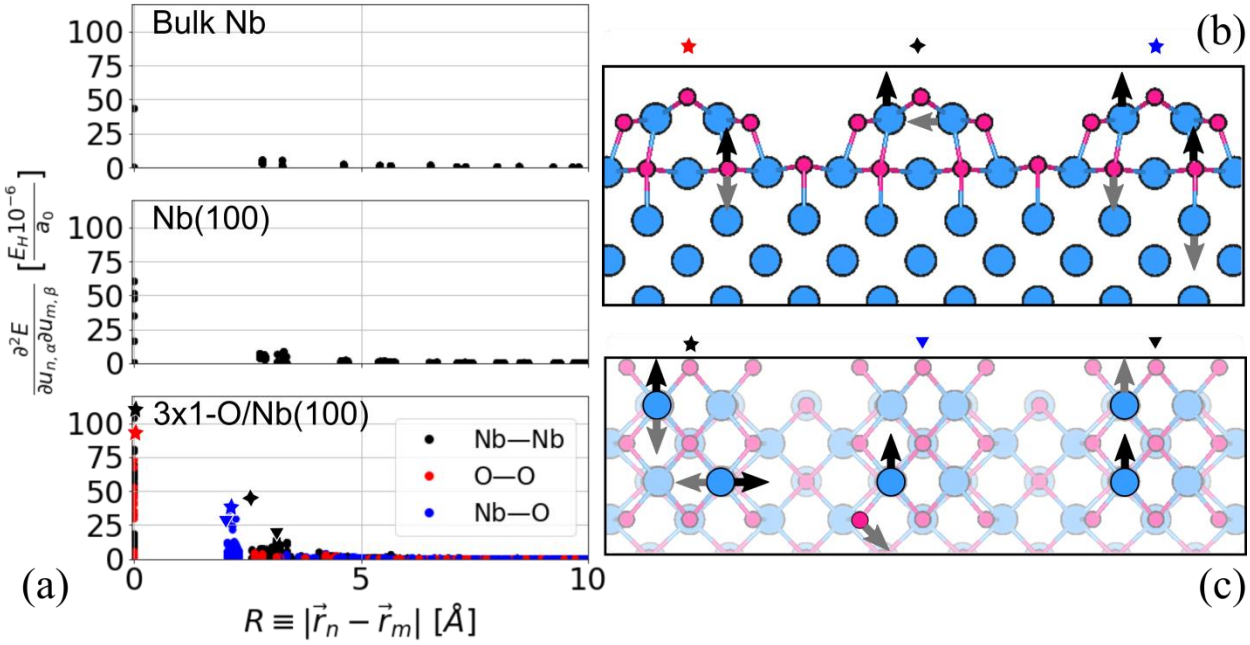

Figure 4.9: (a) Pairwise interatomic force constants in bulk Nb, Nb(100), and (3 × 1)-O Nb(100) all plotted on the same scale as a function of distance between the two atoms, with R = 0 corresponding to the force on an atom when it is perturbed. All interatomic force constants in bulk Nb and Nb(100) involve only Nb-Nb interactions (black circles), while (3 × 1)-O Nb(100) includes additional force constants between Nb-O (blue circles) and O-O (red circles). Noteworthy interatomic force constants in (3 × 1)-O Nb(100) are marked with distinct symbol shapes in (a) and then depicted in the crystal structures in either (b) a side view with surface normal pointing up or in (c) a top down view with surface normal pointing out of the page. In (b) and (c), Nb atoms are colored as larger blue circles and O as smaller magenta circles, and the black and gray arrows correspond to the atomic perturbation and responding forces, respectively.

when another atom in the crest is disturbed along the surface-normal direction, as seen in Figure 9(b). A surface-parallel perturbation of a Nb atom within the crest causes a relatively high

response in a neighboring Nb atom 3.1 Å away, also in the surface-parallel direction (black triangle in Figure 4.9(c)). Most of the force constants that involve O atoms, shown by the red and black markers in Figure 4.9(a), are higher than the Nb-Nb force constants in bulk Nb and the bare Nb(100) surface. This feature occurs most prominently when Nb and O are near neighbors, separated by about R = 2.1 Å (blue five-pointed star in Figure 4.9(b) and blue triangle in Figure 4.9(c)).

Our work shows that the (3 × 1)-O superlattice structure significantly modifies the forces of bulk Nb and the unreconstructed, bare Nb(100) surface. The strong bonds introduced by the (3 × 1)-O superlattice make up the characteristic ladder crests and strongly oppose surface-normal and surface-parallel perturbations. This result explains the high-energy phonon resonances in the dispersion plot shown in Figure 4.7 and stabilizes the Nb surface, leading to Nb's strong affinity for O.[47,48] Additionally, the strengthened Nb-Nb bonds indicate a heightened Nb diffusion barrier at the surface.[115] The (3 × 1)-O structure could inhibit nucleation and alloying at the surface, raising surface melting temperatures and the alloying temperatures of relevant SRF materials such as Sn.[116–118]

Recent work by Farber et al. characterizes Sn adsorption and diffusion behavior on the (3 × 1)-O Nb(100) surface reconstruction.[119] Their results reveal that defects do not alter significantly either Sn adsorption or diffusion: these processes likely are dictated by the (3 × 1)-O superlattice structure. Our results support this interpretation of their data by indicating that the ladder crest features are strongly bonded and thus resistant to perturbation. Our results also explain their observed adsorption sites and preferential diffusion along the troughs of the ladder structure. An atomic-scale, theoretical characterization of the (3 × 1)-O Nb(100) surface alloying with Sn has not been completed. However, our results suggest that the ladder troughs are

susceptible sites for reactivity or alteration, while the ladder crests are strongly stabilizing and provide a barrier to treatments and corresponding reactions. Further atomic-scale studies of alloying on these surfaces will provide a more detailed picture.

4.5 Conclusion

We used HAS and DFT to map the surface phonon dispersions of the (3 × 1)-O Nb(100) reconstruction. A comparison between calculated resonances of the bare Nb(100) surface and the oxide surface show a large increase in phonon modes for the oxide, especially at higher energies. We explicitly calculated the electron-phonon interaction strengths at the surface and compared the results with inelastic He TOF data. The agreement seen between experiment and theory allows us to identify the measured surface modes. The primary modes measured with HAS are caused largely by longitudinal and shear-vertical displacements of the top two layers of O and Nb atoms on the (3 × 1)-O surface, and these modes also display meaningful electron-phonon interaction strengths. DFT analysis of the force constants at the surface show significant increases in bonding between Nb atoms, as well as strong Nb-O and O-O bonds. These data further expound what is known about the oxide surface and will inform the development of new SRF materials by elucidating the dynamics of the oxide surface. While this collaborative work begins to reveal how the (3 × 1)-O superlattice structure alters EPC at the Nb(100) surface, it is only a piece of the picture. Beyond the differences in phonon resonances shown above, the significant modification of interatomic interactions could in turn affect surface superconductivity and SRF cavity behavior. Future experimental and theoretical studies investigating the EPC of these surfaces currently are underway.

Chapter 5

Correlating Electron-Phonon Coupling and *in situ* High Temperature Atomic-Scale Surface Structure at the Metallic Nb(100) surface by Helium Atom Scattering and Density-Functional Theory

Chapter 5 is reproduced from **Thompson, C. J**; Van Duinen, M. F.; Kelley, M. M.; Arias, A. A.; Sibener, S. J. Correlating Electron-Phonon Coupling and *in situ* High Temperature Atomic-Scale Surface Structure at the Metallic Nb(100) Surface by Helium Atom Scattering and Density-Functional Theory. *J. Phys. Chem. C* 128, 14, 6149-6157 (2024) with the permission of AIP Publishing. Copyright 2024 The Journal of Physical Chemistry C.[120]

Helium (He) atom scattering (HAS) simultaneously measured the surface electron-phonon coupling (EPC, SEPC) constant (λ, λ_S) and *in situ* high temperature atomic-scale surface structure of the unreconstructed, metallic Nb(100) surface. The Nb(100) surface λ_S is 0.50 ± 0.08 and its atomic-scale surface structure confirmed. The λ_S measured for the Nb(100) surface is ~1/2 the reported bulk Nb λ values. The significance of Nb(100)'s diminished EPC was elucidated by estimating relevant superconducting properties from the measured λ_S, surface Debye temperature, known material parameters, and well-established equations. Density-functional theory (DFT) with local averaging agrees well with the HAS data. A critical temperature (T_C) of 1.4 – 3.6 K, a superheating field (H_{sh} at 2 K) ≤ 0.16 T, and a superconducting gap (at 2 K) ≤ 1.0 meV were estimated from these measurements. These results indicate that the Nb(100) surface has decreased superconducting properties relative to the bulk. This study shows that these effects may be due also to the interface itself even without oxygen.

These results contain the first λ measured for the metallic Nb(100) and any Nb surface. These measurements begin a fundamental understanding of atomic-scale surface structure's effect on EPC and superconductivity in Nb.

5.1 Introduction

Niobium is the current material of choice for superconducting radio frequency (SRF) cavities in particle accelerators. Both Nb's normal and superconducting state properties have led the material to its ubiquitous use and extensive study in SRF cavities.[6,121–123] Nb's relatively high ductility allows for facile manufacture of optimal cavity geometries for relatively high quality (Q) factors and accelerating gradients.[6,121–124] Additionally, pure Nb's relatively high thermal conductivity facilitates effective cooling, necessary to enter and maintain Nb's superconducting state.[6,121,122] Nb's superconducting state's relatively high critical temperature (T_C) and low RF surface resistance (R_s) contribute significantly to Nb SRF cavities' high Q factors at attainable operating temperatures.[6,123] Since the RF fields only penetrate through the first 40 to 100 nm of the cavity surface, SRF cavity performance depends critically upon the surface chemistry and surface quality.[6,125] Thus, surface preparation of SRF cavities must be carefully designed and implemented. Furthermore, the superconducting state's unique behavior at these surfaces results from SRF cavity preparation techniques.[123,126–130] However, fundamental studies correlating atomic-scale surface structure with changes in the superconducting state remain unexplored. How does the surface modify the physical properties driving the formation of the superconducting state and its favorable properties? A deeper understanding of atomic-scale surface structure's effect on the well-known superconducting state of the bulk would reveal the mechanisms determining which SRF cavity preparations aid or hinder the performance of a cavity. Additionally, since extensive research on Nb and Nb SRF cavities has allowed them to

approach their fundamental limits of operation, the search has begun for new materials and cavity treatments to further reduce R_s, maximize the superheating field (H_{sh}), minimize power loss, and optimize overall performance.[17,124,126,127,130] Due to ≤100 nm penetration depth of RF fields in typical Nb SRF cavities, changes in the surface significantly affect cavity performance.[6,124,125] In fact, surface defects, inhomogeneities, and impurities limit cavity quality factors and operating temperatures, holding back a variety of promising new SRF cavity materials.[123,124,126,128,129,131,132] While well-studied, the evolution of surface defects remains a challenging part of SRF cavity treatment design and implementation. An understanding of the evolution of surface defects and their resulting effects on superconductivity at the surface remains elusive. While the (3x1)-O has been shown to be stable and well-ordered up to ~1130 K under SRF cavity preparations, a foundational understanding of the interface must begin with the metallic, unreconstructed surface.[29] Understanding how specific atomic-scale surface structures arising from distinct SRF cavity preparations impact the accelerator's performance and energetic efficiency would enable SRF cavity surfaces by design. In order to progress to this point, we must first understand the effect of the Nb surface structures on the material's superconducting properties by investigating the effects of surface treatments and their resulting surface structures.

Electron-phonon coupling (EPC) in Nb is responsible for the formation of its superconducting state.[6,8,10,16,133] The EPC constant (λ) is a dimensionless constant that quantifies the effective strength of electron-phonon interactions in a material.[10] This constant then determines many superconducting properties such as the critical temperature (T_C) and superconducting gap.[6,10,16] We will utilize helium (He) atom scattering's (HAS) unique capability for *in situ* high-temperature measurements of both surface structure and surface EPC (SEPC) constant (λ_S) to connect atomic-scale surface structure with its effect on λ_S and thus

surface superconductivity. We have demonstrated this capability by measuring λ_S and atomic-scale surface structure simultaneously on the unreconstructed Nb(100) surface. While the Nb(100) surface structure and phonon band structure has been measured previously and calculated recently by Kelley et al., the SEPC constant, λ_S, has not.[134–138]

Furthermore, these results have begun building a necessary foundational understanding of the effects of atomic-scale surface structure on superconductivity. With this understanding in hand, we plan to investigate variations in atomic-scale surface structure to reveal their effects on surface superconductivity. Because this is the first measurement of SEPC at the Nb(100) surface, much remains to be known about the SEPC of Nb surfaces from changes in surface composition and structure. However, many substantial studies of the EPC in bulk Nb have been made.[136,137,139–145] The EPC of bulk Nb has been measured by electronic Raman scattering (1.15),[142] proximity electron tunneling spectroscopy (1.04 ± 0.06),[146,147] femtosecond pump-probe measurements (1.16 ± 0.11),[144] and calculated with McMillan's well known expression for T_C from accompanying measurements of appropriate normal-state parameters (0.92).[17,18,23]

Atomic and molecular beam scattering techniques have been used to investigate structure and vibrational dynamics of surfaces since the 1920's.[32–34] Supersonic He beams are suited to study surfaces due to their lack of penetration into the bulk, chemical inertness, and remarkably narrow velocity distributions.[18,148] The de Broglie wavelength and narrow momentum distribution of He atoms allow for precise measurements of atomic-scale structure.[5,149] The momentum and energy of He atoms are well-matched to those of surface phonons, giving HAS a unique ability to measure and resolve low-energy phonon modes.[5,12,18,148–150] Recently, the role of SEPC in the He-surface scattering event has been elucidated and theoretically described for single phonon modes and thermally excited phonons in the high temperature limit of many types of

surfaces.[15,23,151–159]

While the derivation of the formula for λ_S differs for each kind of surface, including metals, metallic layers, 2D materials, and topological insulators, the concept of an electron mediated interaction between He and phonon states is present in all.[15,23,151–159] The He atoms scatter off of the surface electron density, and within good approximation scattering repulsive potential is directly proportional to the electron density for metallic surfaces.[20] While He scatters off of the electron density, energy is exchanged between the He atom and the lattice of the crystal surface through phonon creation and annihilation events.[5,23,148] This energy exchange is mediated by the electron density at the surface and has been formulated for a variety of surfaces, especially metallic surfaces.[15,23,151–159] Recent work has expanded this formulation to show that the Debye-Waller (DW) factor is directly proportional to the SEPC (λ_S), which was accomplished starting from the distorted-wave Born approximation, using second-order perturbation theory to define electron-phonon matrix elements, and adopting additional yet reasonable approximations.[10,15,23,159] The DW factor is a multiplicative factor in all scattered intensities that describes thermal attenuation of the He atom's scattering intensity.[5,23,149] Traditionally, the DW factor accounted for the thermal excitation of phonons with appreciable displacements at the surface, however these recent developments elucidated the mediation of thermally excited phonons and scattered He via the electron density.[15,23,149,159] Simply put, the thermal energy of the surface excites phonons at or near enough to the surface that they disturb the surface electron density which then reduces the coherence of the scattered He and measured HAS intensity.[23]

The work presented herein provides the first measurement of λ on the metallic, unreconstructed Nb(100) surface and any Nb surface. Furthermore, it presents *in situ* high temperature atomic-scale surface structure measurements made simultaneously with λ_S

measurement. This work utilizes and demonstrates HAS's unique capability for *in situ* high temperature measurements of both surface structure and the λ_S to connect atomic-scale surface structure with its effect on λ and, thus, superconductivity. This capability unlocks the potential elucidation of the changes to the surface by oxides, carbon impurities, N doping, Sn alloying, and other SRF cavity preparations.

5.2 Methods

Measurements were performed and crystal surface prepared in a UHV scattering instrument. The instrument has been detailed elsewhere, but is summarized below.[29,70,160,161] The instrument was composed of three main sections: a differentially pumped beam source, sample chamber, and a differentially pumped, rotating detector. The sample surface was prepared, altered, and all measurements made *in situ* within the sample chamber. A supersonic atomic or molecular beam was created by expansion from a 15 μm nozzle cooled with a closed-cycle He refrigerator. A skimmer extended through the Mach disk into the zone of silence, extracting a supersonic atomic or molecular beam. In the next differentially pumped chamber the beam passed through a mechanical chopper for pulse modulation. The resulting supersonic beam was nearly monoenergetic ($\Delta v/v \leq 1\%$). This beam made a ~4 mm spot size on the 1 cm sample, scattering into 2π steradians. A triply differentially pumped, computer-controlled, rotatable detector arm collected the scattered atoms or molecules. Between the differentially pumped detector regions, the probe atoms or molecules were ionized by electron bombardment, mass selected using a quadrupole mass spectrometer, and detected with an electron multiplier followed by pulse counting electronics. The flight path was 1.528 m, the sum of the chopper-to-sample path of 0.500 m and the sample to ionizer path of 1.028 m. For our experiments we used He as our probe, scattering from a Nb(100) surface with a supersonic He atomic beam.

Diffraction scans were obtained by square-wave beam modulation, with a 50% duty cycle and a rotating the detector at 0.2° increments with fixed incident angle and energy, with an overall instrument angular resolution of 0.20°. The beam was characterized by time-of-flight (TOF) measurements made with a single-slit chopping, 1% duty cycle pattern. The Nb(100) crystal was mounted on a six-axis manipulator within the HAS instrument's sample chamber. This manipulator enables control over the incident angle, θ_i, azimuthal angle, ϕ, and tilt, χ, with respect to the scattering plane. Electron bombardment heating and a closed-cycle He refrigerator modulated the sample temperature within a range of 300 to 2300 K. Surface Preparation Laboratory (the Netherlands) provided the Nb(100) sample (99.99% purity, ~0.1° cut accuracy), which we then cleaned in the HAS instrument by cycles of annealing and flashing up to 2300 K, in addition to sputtering with 1 keV Ne^+ ions (3 μA maximum). Impurities identified by *in situ* AES were C, B, S, and N; these were removed by the combination of annealing, flashing, and sputtering. We continued the cleaning cycles until only Nb was present on the surface, as confirmed by AES, and until the surface was well-ordered enough for high-intensity He diffraction. Due to the annealing (~2300 K), flashing (~2300 K), and sputtering process described above, the unreconstructed Nb(100) surface formed naturally and spontaneously. The Nb(100) surface structure and cleanliness was confirmed with AES, LEED, and He diffraction. During data collection, the Nb sample was periodically flashed to ~2300 K to eliminate unwanted surface adsorbates. Debye-Waller data were obtained by aligning the crystal at each surface temperature and taking diffraction scans across the specular peak. Each Debye-Waller measurement consisted of varying surface temperature up and then down a chosen temperature range, aligning the crystal and taking a diffraction scan over specular. These measurements were taken from the lower limit, ~1400 K, of the chosen temperature range to the upper limit, ~1750

K, then immediately back down to the lower limit. The lower temperature limit was determined as the lowest temperature free of substantial background gas adsorption in the time it took to align and take a diffraction scan. The crystal and mount thermally equilibrated for ~5 minutes and then was aligned before every diffraction scan. The thermal equilibration time for the crystal and mount was determined by comparing thermocouple measurements on the mount with pyrometer measurements of the crystal.

To theoretically study the Nb(100) surface, we performed density-functional theory (DFT) calculations using open-source planewave software JDFTx.[162,163] We implemented norm-conserving pseudopotentials[164] and calculated the electronic states for the outer electrons of niobium ($4p^6 5s^2 4d^3$) at an effective temperature of 20 milli-Hartree using a Fermi function to determine electronic occupancies. The exchange-correlation energy was approximated using the Perdew-Burke-Ernzerhof functional revised for solids (PBEsol).[165] Our calculations employed planewave cutoff energies of 30 Hartree and 200 Hartree for the electronic wavefunctions and density, respectively. We computed properties of a 10-layer slab of niobium with (100) surface termination in a cell that is 42.33 Å long along the surface-normal direction and truncated Coulomb potentials to increase the accuracy of calculated surface properties.[166] We calculated a lateral lattice constant for Nb(100) at 3.30 Å, in good agreement with the experimental measurement of 3.29 Å.[167] We calculated phonon properties using the finite-difference supercell method, perturbing atoms by ~0.4 to 0.5 a_0 to calculate the real space interatomic force constant matrix directly.[168] Interatomic force constant matrices for Nb(100) were evaluated in a 3×3×1 supercell with a k-space sampling density equal to the unit cell's sampling of 12×12×1 k-points.

5.3 Results and Discussion

The clean metallic unreconstructed Nb(100) surface was prepared and confirmed with HAS diffraction and AES in Figure 5.1(a) and Figure 5.1(b), respectively. Figure 5.1(a) contains a diffraction scan taken at 1297 K along the <$\bar{1}$00>, $\overline{\Gamma X}$ azimuthal direction. Each peak occurs when the von Laue condition holds true, or when

$$\Delta K = k_i(\sin\theta_i - \sin\theta_f) = G_{mn}, \tag{5.1}$$

where the surface-parallel component of the He wavevector k_i changes by ΔK; the initial and final scattering angles, relative to surface normal, are θ_i and θ_f, respectively; and G_{mn} is a linear combination of reciprocal surface lattice vectors.[5,8,149] The scan shows an intense, narrow specular peak ($\theta_i = \theta_f$) at ΔK = 0 and the first-order ($0\bar{1}$) diffraction peak at $\Delta K = -2.000$ Å^{-1}, just slightly beyond the expected -1.904 Å^{-1}.[134,135] This diffraction peak shifted slightly above and below the expected value after each preparation, indicating some lattice compression and expansion.[169] The specular peak is ~28 times the size of the first order diffraction peak, typical of a smooth metal surface with relatively flat electronic corrugation.[23,170] The absence of oxygen in the Auger data is corroborated by the absence of any superlattice peaks along this symmetry direction in the diffraction scan.[29,70,135]

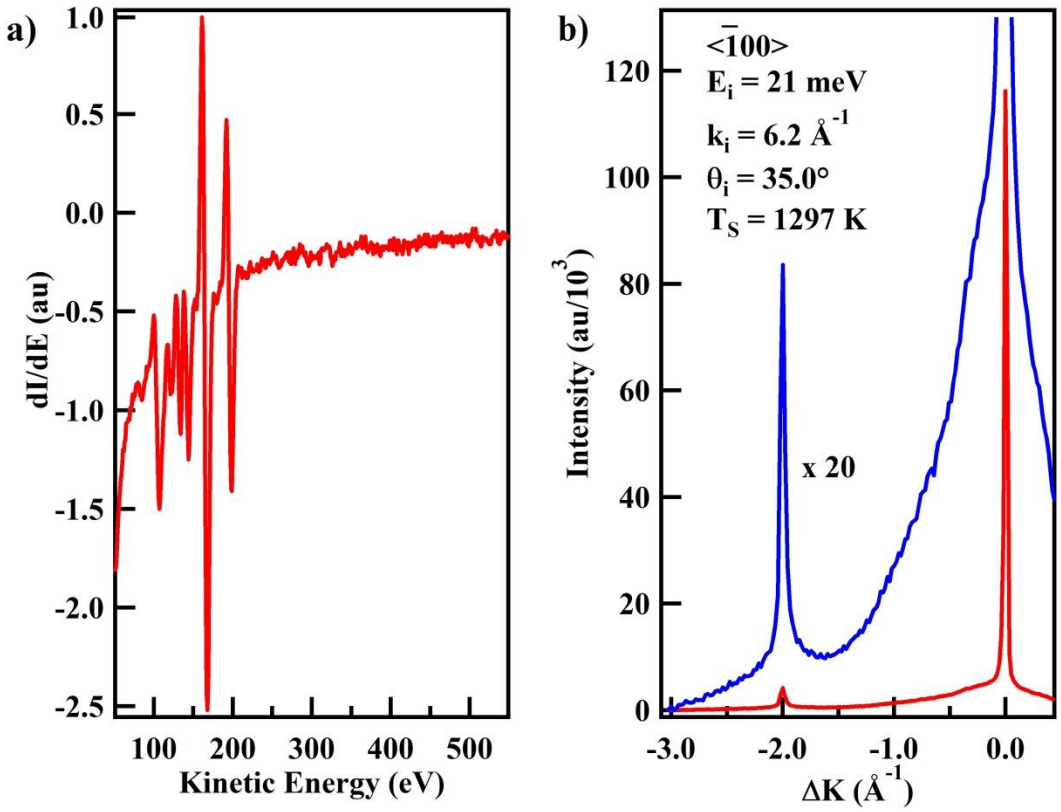

Figure 5.1: Representative (a) Auger electron spectrum and (b) He atom diffraction spectrum for the clean, unreconstructed Nb(100) surface along the <$\bar{1}$00> symmetry axis. In (a) the primary Nb peak is evident at 167 eV and the secondary Nb peak at 192 eV. There is an absence of C (270 eV), N (379 eV), and O (503 eV) peaks, indicating a clean Nb surface. In (b) there is only the first order diffraction peak. This peak is sharp and weak relative to the specular reflection, indicating a smooth, well-ordered metallic surface.

Thermal attenuation of the specular peak occurs due to thermally excited phonons disturbing the electron density at the surface. This thermal attenuation follows the following relation,

$$I(T_S) = I(0)e^{-2W(T_S)}, \tag{5.2}$$

Where I is the measured He scattered intensity and $2W$ is the DW factor.[26,149] The traditional definition of the DW factor is

$$2W(T_S) = \langle \left(\Delta k \cdot u(T_S)\right)^2 \rangle, \tag{5.3}$$

where Δk is the change in wavevector of the scattered He and u atomic displacement of the surface atoms.[26] However, recently, Manson et al. has derived the relationship between 2W and the surface EPC constant, yielding the approximation,

$$\lambda_{HAS} \cong -\frac{d \ln I_{00}}{k_B dT_S} \frac{\phi}{6Z} \frac{k_F^2}{k_{iz}^2}, \tag{5.4}$$

where I_{00} is the intensity of the specular reflection, ϕ is the work function, Z is the number of free electrons per atom, k_F is the Fermi wavevector, and k_{iz} is the surface perpendicular (z) component of the incident He incident wavevector.[15,159] The DW diffraction scans were taken over the specular peak at a variety of temperatures. These temperatures were chosen to be above any significant adsorption of background gasses. These diffraction scans were taken from temperatures ~1400 K to ~1750 K for a variety of beam energies.

The data used for the slope, $\frac{d \ln I_{00}}{k_B dT_S}$, which determines λ_S through Eq. 5.4, were measured taking particular care for surface cleanliness. Specifically, these EPC DW data (Figure 5.2) were obtained while confirming a clean Nb(100) surface structure through cleanliness with HAS diffraction and AES immediately before and after each DW measurement. This procedure ensured no impurities interfered with the measurement.

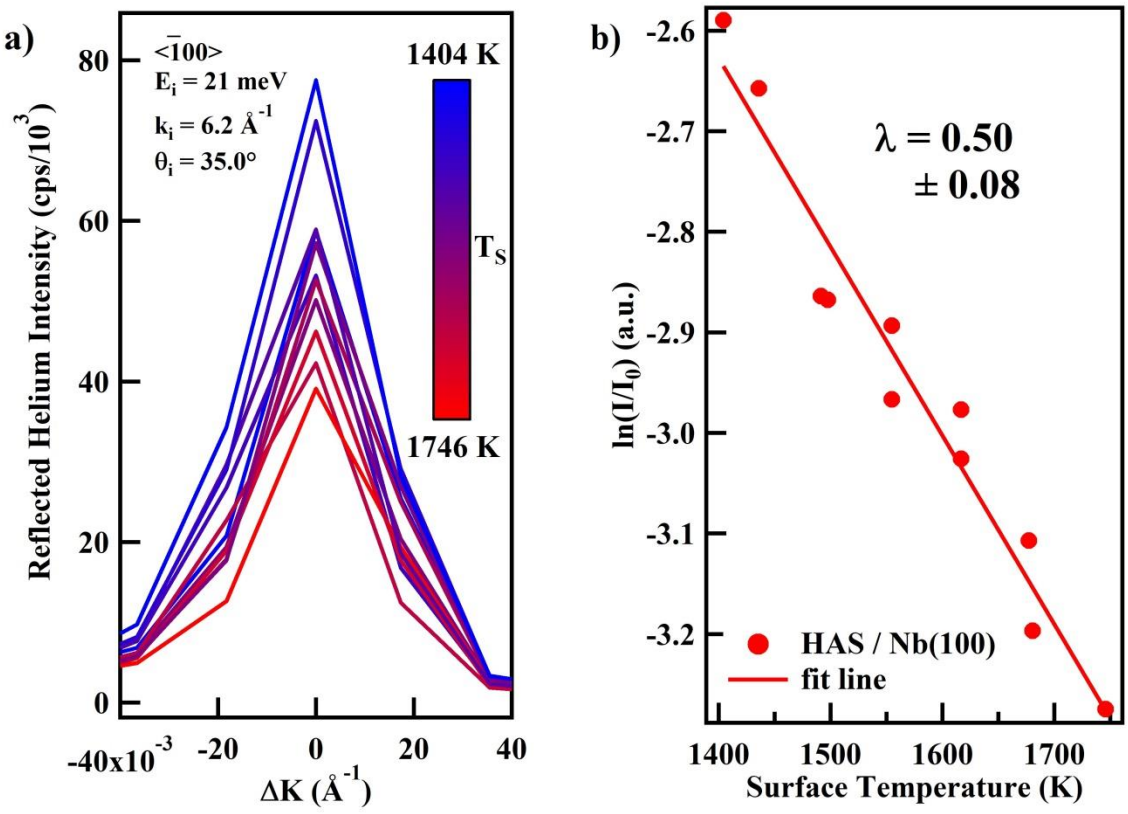

Figure 5.2: Thermal attenuation of the specular peak is observed in (a), where diffraction scans through the range were taken proceeding up the temperature range to 1746 K and then back down to 1404 K. The surface structure and cleanliness was confirmed with HAS diffraction and AES immediately before and after the measurement. The intensity values are taken from these specular reflections and plotted in (b). In (b) the ln of specular intensity is plotted versus surface temperature. The linear fit provides I_0 (intensity at 0 K) from the y-intercept fitting parameter and a slope fitting parameter equal to $\frac{d \ln I_{00}}{dT_S}$. From this slope and tabulated values for Nb's work function, number of free electrons per atom, and Fermi wavevector, we calculate λ = 0.50 ± 0.08 for the Nb(100) surface. The error is propagated from the fit error of the slope fitting parameter. Furthermore, we also extract the surface Debye temperature of 369 ± 11 K from these data, verifying that the system in the high temperature regime of the Bose-Einstein phonon population function required for equation 5.3. Additionally the Debye temperature is used in calculating the T_C from the measured λ and the McMillan equation.

This slope and tabulated values of the Fermi vector, work function, and number of free electrons per atom were used to calculate a λ_S of 0.50 ± 0.08 for the clean metallic Nb(100) surface.[8,15,159] The uncertainty in this value is propagated from the error in the linear fit of the data.

This is the first recorded value of λ for any Nb surface and, specifically the Nb(100) surface. The recorded λ values for bulk Nb are 1.15, 1.04, 1.16, and 0.92, almost twice the value at the Nb(100) surface we determine here.[136,137,139–145] This deviation shows that the Nb(100) surface reduces the electron phonon coupling at the surface relative to the bulk. This reduction indicates the termination of the Nb lattice with a Nb(100) surface should be expected to significantly decrease the superconducting gap and increase the RF resistance relative to the bulk. In SRF cavities, the surface oxide is commonly thought to decrease the efficiency of Nb SRF cavities; surprisingly, these effects may be due to the termination of the lattice in addition to the effects of the oxygen.[6,132] This work begins to build a fundamental understanding of the effects of the surface.

In addition to this refined DW measurement of the clean Nb(100) surface, we obtained a variety of DW measurements with varying amounts of impurities as measured by AES. These impurities did not affect surface structure, periodicity, order, or electronic corrugation, but they did affect Nb(100) SEPC. We concluded from further data analysis that these impurities must be at the subsurface. This ultimately meant that while these data were not appropriate to determine λ_S for a pure, metallic Nb(100) surface, they were ultimately appropriate to determine a He-surface attractive potential well depth, and they reveal linear trends between SEPC and impurity concentration. These data are summarized in Figure 5.3.

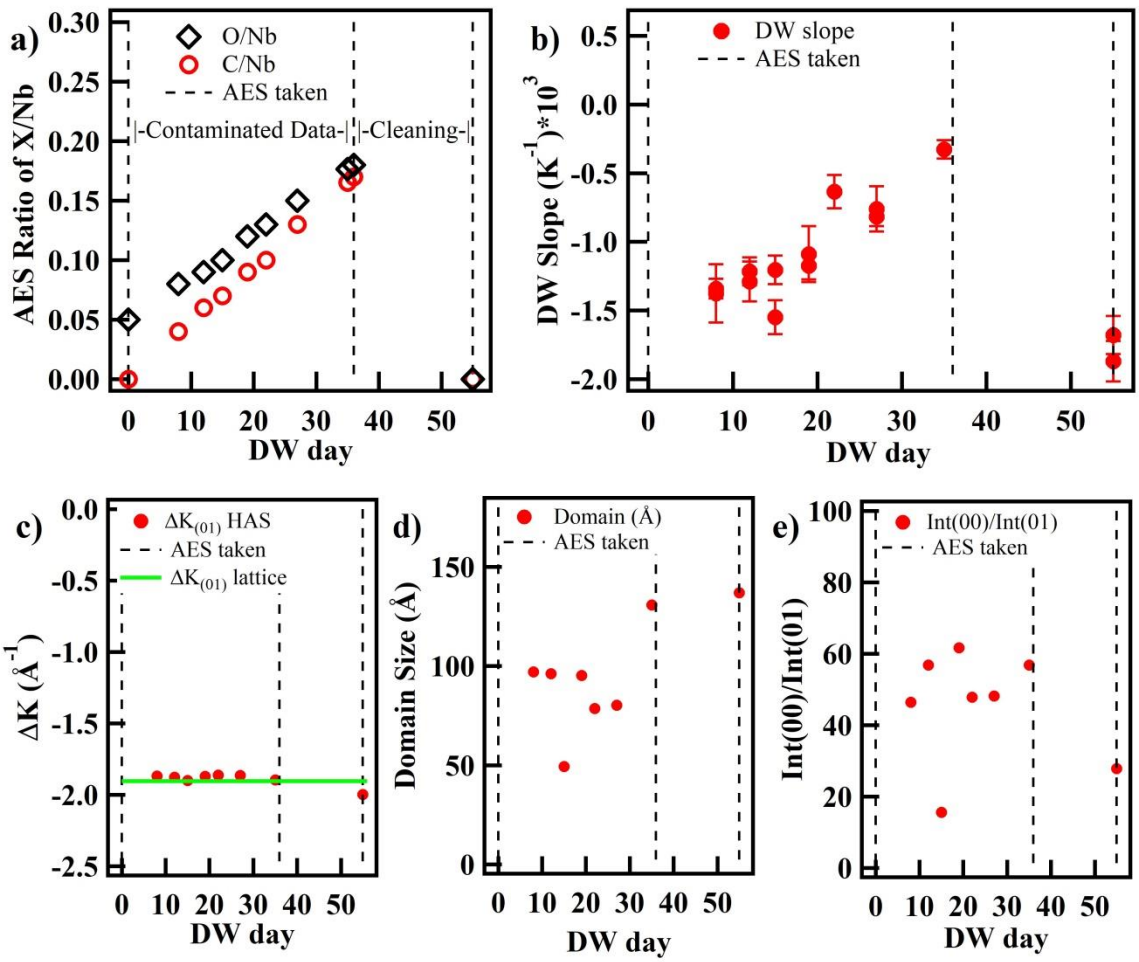

Figure 5.3: In (a) the AES ratio of O and C with Nb are plotted versus time (days). The blue lines mark when AES spectra were taken and the region between day 0 and day 36 was linearly interpolated to obtain the O and C ratio on each day. In (b) the DW slopes from each day were plotted versus time (days) showing a strong correlation with the O and C content. However in plots (c), (d), and (e) the (01) diffraction peak dK, domain size, and ratio of (01) peak to the specular (00) peak respectively show no correlation with O and C content. The diffraction peak's dK (c) show that the periodic lattice spacing

Looking at the data in Figure 5.3, one may observe the correlation between O and C content with the DW slope, but not in the diffraction peak location, specular to diffraction peak ratio, or the

domain size (extracted from the FWHM of the specular peak). The latter three properties are specific to surface structure, periodicity, order, and electronic corrugation, but the DW slopes involve surface vibrations that are also affected by the subsurface.[11,171] Since AES probes both the surface and a few layers into the subsurface, and the DW slope is the only surface property we measured that seems to be affected by the C and O impurities, we can conclude that these impurities must lie at the subsurface but not at the surface. If we take the DW data where the subsurface O and C content varies and extract λ_S, we see that there is an apparent diminishing of λ_S with accumulation of subsurface O and C impurities (Figure 5.4).

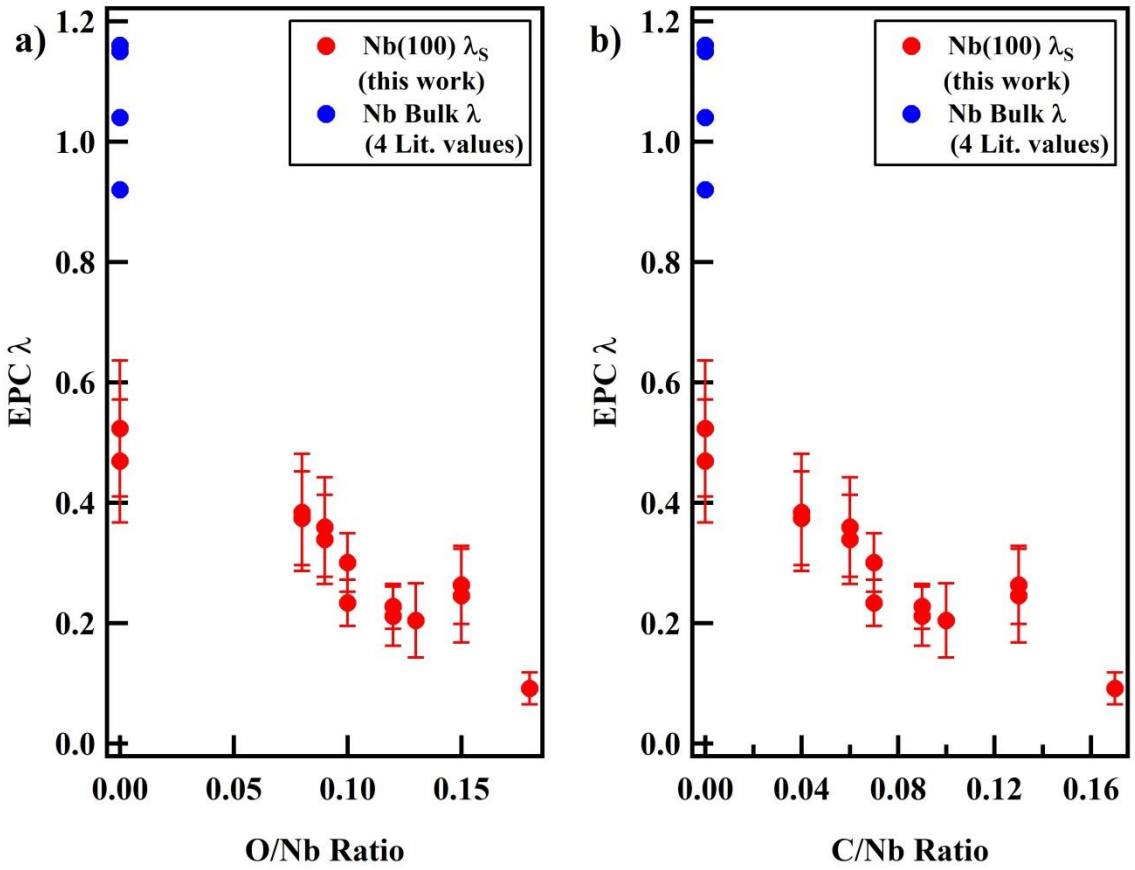

Figure 5.4: The EPC constant was extracted from the DW slopes plotted in Figure 5.3 (b) and plotted against O/Nb (a) and C/Nb (b). There is an apparent diminishing of λ_S with accumulation of subsurface O and C impurities. While we have not intended to study or observe this effect, we have coincidentally observed it. This effect deserves its own investigation that is outside the scope of this paper. Nonetheless, the data show that subsurface O and C apparently diminishes λ_S and indicates such subsurface impurities actively contribute to surface superconductivity and SRF cavity performance.

For the impure DW measurements, the subsurface O and C contents on each DW measurement were estimated by linearly interpolating between the two AES measurements on day 1 and day 36 in Figure 5.3 (a). While not the primary focus of this study, this effect is deserving of its own investigation in future work. Nonetheless, the data show that subsurface O and C apparently

diminishes λ_S and indicate such subsurface impurities actively contribute to surface superconductivity and SRF cavity performance. In fact, the effect of interstitial O on bulk Nb's EPC has been measured in the range of 0% to 4% by Koch et al.[140] These amounts of interstitial O were observed to decrease the EPC linearly with accumulated interstitial O, much like the trend observed in Figure 5.4 (a).

At beam energies from ~17 meV to ~35 meV the acceleration due to the He-surface attractive potential well depth, D, is significant and must be taken into account. The Beeby approximation is commonly used to correct for this effect, taking into account the acceleration of the He atom as it approaches the surface before reaching its turning point.[5,148,149] In the Beeby approximation, the potential well depth is added to the surface perpendicular component of the incident He beam energy.[5] This quantity can be measured by expanding the traditional expression for the DW factor with standard kinematics. Upon substitution, restriction to specular scattering, and rearrangement, the relation,

$$\sigma = -\frac{d(2W)}{dT_S} = 4k_i^2 \frac{d\langle u_z^2 \rangle}{dT_S}\left[\cos^2\theta_i + \frac{D}{E_i}\right], \tag{5.5}$$

is obtained, where σ is the negative slope of a DW linear plot, k_i is the He incident wavevector, θ_i is incident angle relative to surface normal, D is the He-surface potential well depth, and E_i is the He incident energy.[27,149] Thus, a fit of DW decay, σ, versus $E_i\cos^2\theta_i$ yields the He-surface attractive potential well depth and the first derivative of the mean-square displacement with respect to surface temperature. We will choose DW measurements with the narrowest range of subsurface impurities at 3 beam temperatures and use them to obtain a He-surface attractive potential well depth (Figure 5.5). The data with subsurface impurities are appropriate for the well depth calculation since the attractive potential well depth is exclusively a surface phenomenon.

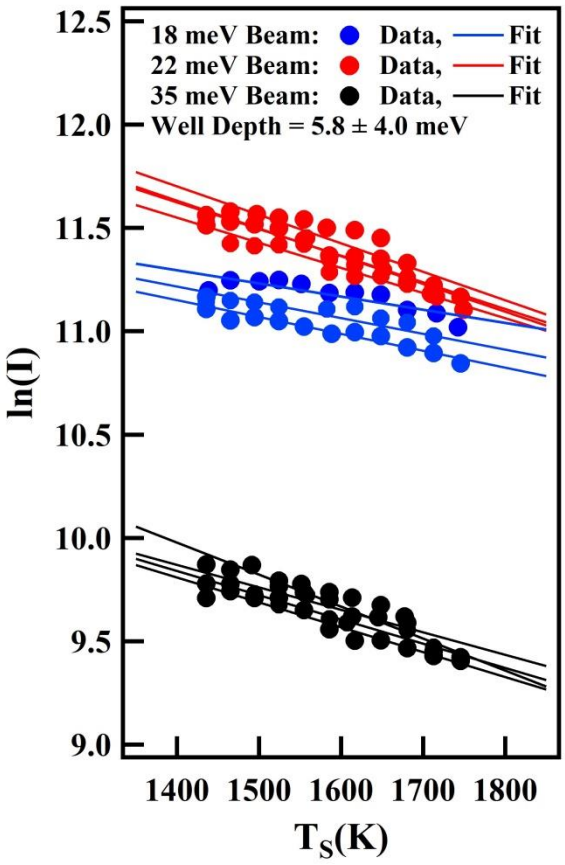

Figure 5.5: DW lines at 3 beam energies were selected for a relatively narrow range of subsurface impurities. These data provide the He-surface well depth, 5.8 meV with error due to varying subsurface impurities. Having an estimate for the well depth, D, allows us to correct our incident beam energy in the so called Beeby correction.

From the fitting parameters we obtain a He-surface well depth of 5.8 with error due to varying subsurface impurities. Having an estimate for the well depth D allows us to correct our incident beam energy with the Beeby correction.

We use DFT calculations of the mean-squared displacement (MSD) of the surface atomic vibrations of Nb(100) to complement our HAS data from the clean, metallic Nb(100). Figure 5.6

shows the vertical mean-squared displacement (MSD) of the surface atomic vibrations of Nb(100) calculated with

$$\langle u_z^2 \rangle = \frac{1}{N_{\boldsymbol{Q}}} \sum_{\boldsymbol{Q}\nu} \left[2n\left(\omega_{\boldsymbol{Q}\nu}, T\right) + 1 \right] \frac{\hbar \left| e_{\boldsymbol{Q}\nu}^{0,z} \right|^2}{2M\omega_{\boldsymbol{Q}\nu}}, \tag{5.6}$$

where the summation samples phonon modes ν at wavevectors $\boldsymbol{Q}$ throughout the surface Brillouin zone, $e_{\boldsymbol{Q}\nu}^{0,z}$, is the component of the phonon eigenvector corresponding to the z-displacement of the surface niobium-atom of mass M, and the bose factor $n(\omega_{\boldsymbol{Q}\nu})$ weights the displacements of each sampled phonon mode at temperature T.[23] This quantity enters the traditional definition of the DW factor in Eq. 5.3.

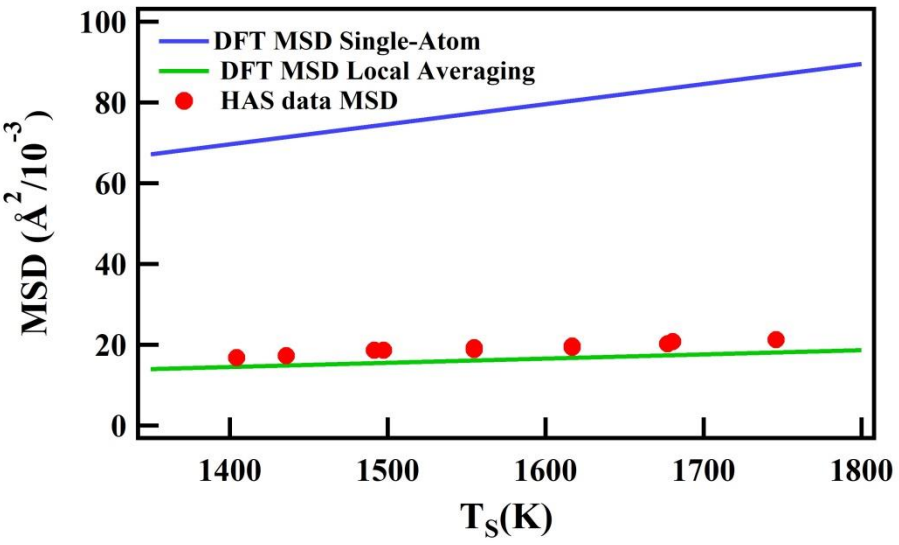

Figure 5.6: The upper theoretical curve (blue) shows the raw average of $\langle u_z^2 \rangle$ considering the one Nb atom of the monatomic crystal structure. The lower theoretical (green) shows an effective MSD after averaging over the four surface atoms from the square unit cell, which accounts for the likelihood of the incident He atom interacting with more than one Nb atom due to the comparable distance between Nb surface atoms and the finite size of He. The HAS data (red dots) falls upon the DFT prediction for HAS scattering (green) confirming the HAS measurements of clean, unreconstructed Nb(100).

The lower theoretical curve shows the raw average of $\langle u_z^2 \rangle$ considering the one Nb atom of the monatomic crystal structure. The upper theoretical shows an effective MSD after averaging over the four surface atoms from the square unit cell, which accounts for the likelihood of the incident He atom interacting with more than one Nb atom due to the comparable distance between Nb surface atoms and the finite size of He.[171] Using this locally averaged MSD and performing a least-squares fit of the well-depth in the Beeby approximation, the predicted DW factor from this effective MSD would match the measured HAS DW data at a well-depth of 9.5 meV. The HAS data falls within this region confirming the HAS measurements of clean, unreconstructed Nb(100).

To more deeply understand how this modification of the bulk λ would affect the surface's performance in an SRF cavity, we estimate superconducting properties that are commonly used benchmarks for prospective SRF cavity materials.[6,17] The resulting values are compiled in Table 5.1.

Table 5.1: Benchmark superconducting properties were estimated from well-used equations, using EPC constants and tabulated material properties. Superconducting properties were estimated for T = 2 K, using well-known tabulated values for Nb: London penetration depth = 40 nm, ξ = 27 nm, $\boldsymbol{\kappa}$ = 1.5, μ* = 0.1 – 0.15, and critical field of 0.20 T at 0 K. The surface EPC and Debye temperature extracted from HAS data were used to estimate the values for the unreconstructed Nb(100) surface.

	λ EPC	T_C (K)	Critical field (T)	Superheating field (T)	Band Gap (meV)
Nb(100)	0.50	1.4 – 3.6	≤ 0.14	≤ 0.16	≤ 1.0
Nb bulk (Ref. [136,137,139–145])	1.15, 1.04, 1.16, 0.92	9	0.21	0.25	2.8

We used Dynes' version of McMillan's equation as well as our measured surface Debye temperature and λ_S to estimate a T_C within the range of 1.4-3.6 K, significantly reduced from the bulk Nb value of 9 K.[6,10,13,16] A lower T_C ultimately corresponds to a lower superheating field H_{sh} of ≤ 0.16 T compared to the bulk value 0.25 T.[6,8,17,172] This means that superconducting states at the Nb(100) surface quench at lower magnetic fields than those in the bulk, reducing SRF performance.[123,172] We estimate the superconducting gap at 0 K and then, using λ_S and an empirical temperature dependence valid below T_C, estimate a superconducting gap at 2 K to be ≤ 1.0 meV, significantly reduced from 2.8 meV for bulk Nb at 2 K.[6,10,143,173] A smaller superconducting gap results in a higher R_S, a lower Q, and therefore a less efficient SRF cavity.[16,124] These theoretical estimates from our measured λ_S and surface Debye temperature as well as the measurements themselves show that the atomic-scale surface structure of the Nb(100) significantly modifies the relevant properties of the superconducting state, decreasing the SRF cavity performance even without the presence of a deleterious oxide.

5.4 Conclusion

We have utilized He atom scattering's (HAS) unique capability for *in situ* high temperature measurements of both surface structure and the surface electron-phonon coupling (SEPC) constant, λ_S, to connect atomic-scale surface structure with its effect on λ_S and thus superconductivity. We measured the λ_S and *in situ* high temperature atomic-scale structure of the unreconstructed, metallic Nb(100) surface. The thermal attenuation of specular reflectivity gave a λ_S of 0.50 ± 0.08, and He diffraction confirmed the unreconstructed metallic Nb(100) surface. These results make the first λ_S measured for the unreconstructed, metallic Nb(100) surface and any Nb surface. We find that SEPC, T_C, superconducting gap, and superheating field at operational temperatures are significantly reduced at the Nb(100) surface relative to the bulk Nb. While the Nb surface in SRF cavities is oxidized, this begins to build a needed, fundamental understanding of the effects of the surface on superconducting properties, and from there we can begin to understand the changes to the surface by oxides, carbon impurities, N doping, Sn alloying, and other SRF cavity preparations. These measurements are the beginning of a fundamental understanding of atomic-scale surface structure's effect on EPC and superconductivity in Nb, enabling SRF cavity surfaces by design.

Chapter 6

Distinguishing the Roles of Atomic-Scale Surface Structure and Chemical Composition in Electron-Phonon Coupling of the Nb(100) Surface Oxide Reconstruction

Chapter 6 is adapted with permission from **Thompson, C. J.**; Van Duinen, M. F.; Mendez, C.; Willson, S. A.; Do, V; Arias, T. A.; Sibener, S. J. Distinguishing the Roles of Atomic-Scale Surface Structure and Chemical Composition in Electron Phonon Coupling of the Nb(100) Surface Oxide Reconstruction. *J. Phys. Chem. C* 128, 25, 10714-10722 (2024) with the permission of AIP Publishing. Copyright 2024 The Journal of Physical Chemistry C.[174]

The (3×1)-O/Nb(100) surface λ_S was measured to be 0.20 ± 0.06 and its atomic-scale surface structure confirmed. These results were supported by consistency between measured helium atom scattering Debye-Waller factors and *ab initio* density-functional theory predictions. The λ_S measured for the (3×1)-O surface reconstruction is further diminished from the metallic, unreconstructed Nb(100) value and the reported bulk Nb λ values. Furthermore, varying subsurface O has no significant effect on the λ_S of the (3×1)-O reconstruction. While the metallic, unreconstructed Nb(100) surface is significantly affected by accumulated subsurface C and O, the (3×1)-O reconstruction stabilizes its λ_S against the effects of subsurface O. Due to the low λ_S, a negligible critical temperature (T_C) ≤ 6.2E-3 K was estimated, indicating that at operational temperatures of ~2 K, the (3×1)-O/Nb(100) reconstruction is not superconducting alone. However, the proximity effect indicates that a thin normal metal in contact with a superconductor exhibits some superconducting properties while the superconductor's properties

are diminished. These results contain the first measurement of (3×1)-O/Nb(100) λ_S , distinguish the effects of surface structure and chemical composition on λ_S, and indicate that the (3×1)-O/Nb(100) surface has diminished superconducting properties relative to the unreconstructed, metallic Nb(100) and the Nb bulk.

6.1 Introduction

Niobium is the standard material for superconducting radio frequency cavities in high energy particle accelerators. Nb found its ubiquitous use and extensive study in SRF cavities due to both its normal and superconducting state properties.[6,121,123,175] For example, Nb's relatively high ductility enables facile shaping of optimal cavity geometries for relatively high quality (Q) factors and accelerating fields.[6,124,175] Additionally, pure Nb has a relatively high thermal conductivity facilitating sufficient cooling, essential to enter and maintain Nb's superconducting state.[6,121] Nb's superconducting state's relatively high critical temperature (T_C) and low RF surface resistance (R_s) drives high Q factors at attainable operating temperatures.[6,123] The superconducting state's capability of repelling magnetic fields contains accelerating RF fields. In fact, the RF field only penetrates up to ~100 nm in Nb SRF cavities, thus RF field energy losses occur along the SRF cavity's surface.[6,125] The Nb's SRF cavity's RF surface resistance determines the magnitudes of the energy losses.[6,16] These losses heat the SRF cavity, in turn requiring more cooling to maintain the optimal operational temperatures and driving up costs of operation.[7,176] Experimental and theoretical studies have documented and studied mechanisms in which even local hot spots from inhomogeneities, defects, and topographical variations can heat and quench entire SRF cavities.[17,124,128,131,176–178] Thus, optimal preparation of Nb SRF cavity surfaces are required to prepare energetically efficient SRF cavities and keep costs of operation from being prohibitively high. In other words, the relationship between atomic-scale surface

structure and the resulting superconducting properties at the surface is critical in improving and developing next generation SRF cavity materials.

Extensive study of Nb and Nb SRF cavities has pushed their performance to their fundamental limits of operation. Thus, the SRF community has begun developing new materials and cavity treatments to further reduce R_s, maximize the superheating field (H_{sh}), minimize power loss, and optimize overall performance.[17,124,126,127,179] In fact, defects, inhomogeneities, and impurities at the surfaces limit cavity quality factors and operating temperatures, limiting the implementation of promising new SRF cavity materials.[123,124,126,128,129,131,132] While well-studied, the formation and evolution of surface defects and compositional inhomogeneities remains a challenging part of SRF cavity treatment design and implementation. Such an understanding of the role of surface structure and chemical composition as well as their resulting effects on superconductivity at the surface remains elusive. This relationship is not well understood, and we have only just begun its elucidation with simultaneous *in situ* atomic scale surface structure and surface EPC measurements on the bare metallic Nb(100) surface.[120]

Conventional superconducting states form due to electron-phonon interactions that condense electrons into Cooper pairs.[8,10,16,133,180] The electron-phonon coupling (EPC) constant (λ) is a dimensionless constant that quantifies the effective strength of electron-phonon interactions in a material.[10,13] Furthermore, this constant determines many superconducting properties such as the critical temperature (T_C) and superconducting gap.[10,13,16] We have brought into effective action helium (He) atom scattering's (HAS) sensitivity to both *in situ* high-temperature surface structure and surface EPC (SEPC) constant (λ_S) to connect atomic-scale surface structure with its effect on λ_S and thus surface superconductivity. Previously, we have demonstrated this capability by measuring λ_S and atomic-scale surface structure simultaneously on the unreconstructed

Nb(100) surface and now set forth in this work the results of a similar study on the Nb(100) surface oxide reconstruction.[120]

Due to Nb's exceptional affinity for O and spontaneous O surface segregation, Nb surfaces exposed to air are reconstructed by a robust and complex oxide.[181–183] The Nb surface oxide system has been studied extensively with a variety of techniques and requires prohibitively high temperatures (<2400 K) to remove the O as sublimed NbO.[135,167,181–187] Upon exposure to air at ambient conditions, a ~5 nm pentoxide film spontaneously forms.[183,186] It has been shown through XPS that for both single crystal and polycrystalline Nb surfaces that the pentoxide film dissolves above 600 K in UHV conditions, forming a monolayer of NbO.[181,184,187] These conditions match those typical of Nb SRF cavity preparations and we expect the Nb surface to form the thermodynamic minimum of the system, a NbO monolayer. On the Nb(100) face, the NbO monolayer's most stable phase is the (3×1)-O superlattice reconstruction. In fact, this surface oxide reconstruction has been demonstrated with *in situ* high temperature helium diffraction and high temperature AES to be stable up to 1130 K in terms of structure, order, and composition.[29] In other words, the Nb(100) face under typical SRF cavity preparations (both those treating the native Nb surface and those that grow new materials on it) forms a stable NbO surface reconstruction. Furthermore, the synergy of HAS time of flight measurements and novel DFT calculations found that exceptionally strong Nb-Nb and Nb-O bonds make up the (3×1)-O ladder protrusions, exhibiting forces significantly larger in magnitude than any forces in the bulk Nb and unreconstructed Nb(100) surface. In other words, these atomic-scale ladder protrusions were identified as a key driving force for the (3×1)-O reconstruction's stability and is a significant barrier to incorporation or alloying of SRF cavity treatments.

While we have recently made the first measurement of surface EPC on any Nb surface, specifically the metallic, unreconstructed Nb(100) surface, EPC in bulk Nb has been studied thoroughly.[136,137,139–145,145,147] The λ of bulk Nb has been measured by electronic Raman scattering (1.15),[142] proximity electron tunneling spectroscopy (1.04 ± 0.06),[146,147] femtosecond pump-probe measurements (1.16 ± 0.11),[144] and calculated with McMillan's expression for T_C from accompanying measurements of appropriate normal-state parameters (0.92).[139] Recently, we measured the EPC of the bare metal surface to be 0.50 and used it to estimate benchmark superconducting properties, correlating atomic scale structure to speculative SRF cavity performance.[120] The diminished EPC at the surface of the unreconstructed metallic Nb(100) surface implies that even without O or reconstruction the presence of an interface approximately halves the λ. However, as established in literature, the state of a Nb(100) surface under SRF cavity preparation conditions readily forms the (3×1)-O surface oxide reconstruction on the Nb(100) face.[29,181,184,187] The effects of interstitial O on bulk Nb superconductivity have been investigated.[139,140] Note that interstitial O dissolved in the Nb lattice is distinct from an oxide reconstruction that forms a superlattice. DeSorbo reports[139] that below the solubility limit interstitial O atoms decreases T_C by 0.93 K per at.% O while Koch et al. reports[140] that increasing amounts of interstitial O not only decreases T_C, but also decreases the electronic coefficient of low-temperature-specific-heat capacity, electronic density of states at the Fermi level, and λ. Thus, notably O impacts bulk Nb's EPC via not just the phonons of Nb, but also via the electronic states.[140]

While the measurement of the bare metal λ yields new insight, this result cannot distinguish the effect of the interface from that of the surface oxide reconstruction on surface superconductivity. Thus, there remains a critical gap in the foundational knowledge of the atomic

scale surface structure and composition as well as its effects on SRF cavity performance. An important part of that gap is the correlation of structure and composition of the NbO surface oxide monolayer to the resulting surface superconducting properties.

Supersonic helium beams have been used to probe surfaces since the 1920's. Their lack of penetration into the bulk, chemical inertness, and remarkably narrow velocity distributions are sufficient to create a truly surface sensitive technique.[19,148,149] The de Broglie wavelength and narrow momentum distribution of He atoms are well matched to atomic-scale structure and allow for precise measurements.[5,188] Coincidentally, the momentum and energy of He atoms sufficiently resonate with surface phonons, making HAS uniquely suited to measure and resolve low-energy phonon modes at surfaces.[12,70,148,188] While helium atoms exchange energy with phonons, the helium atoms scatter off of the electron density.[20] Thus, inelastic helium-phonon scattering events are actually two concerted scattering events: helium-electron and electron-phonon. A theoretical description of this helium-electron-phonon scattering event has been developed for metals, semiconductors, topological insulators, 2D materials, and metallic films to show that the Debye-Waller (DW) factor is directly proportional to the SEPC (λ_S).[15,150,151,155–157,159,188–191] The derivation starts from the distorted-wave Born approximation, using second-order perturbation theory to define electron-phonon matrix elements, and adopting additional yet reasonable approximations.[15,159] The DW factor describes thermal attenuation of the scattered He intensity and does so as a multiplicative factor present in all scattering probabilities.[148,188] This DW factor originally came from neutron and x-ray scattering, accounting for motion of nuclei in the lattice from thermal excitation of phonons.[5,8,148] However, after being applied to helium atom scattering, the theory was developed and the role of the electron density elucidated.[150,188] Simply put, the thermal excitation of phonons at or near enough to the surface perturbs the surface

electron density, reducing the coherence of the scattered He and measured HAS intensity.[15,150,159,188]

The work presented herein provides the first measurement of λ of the (3×1)-O/Nb(100) surface oxide reconstruction. These results distinguish the effect of the surface oxide reconstruction from that of interstitial oxygen on Nb(100)'s surface superconductivity.[120] These finding begin to fill a critical gap in the foundational knowledge of the effect of atomic scale surface structure and composition on SRF cavity performance.

6.2 Experimental

Measurements and surface preparations were performed in a UHV scattering instrument. The instrument has been detailed elsewhere, but is summarized here.[29,70,160,161] The scattering instrument was made up of three main sections: a differentially pumped beam source, a sample chamber, and a differentially pumped, rotating detector. The sample surface was prepared and HAS, AES, and LEED measurements made *in situ* within the sample chamber. A supersonic atomic or molecular beam was created by expansion from a 15 μm nozzle that was cooled with a closed-cycle He refrigerator. A skimmer extracted the supersonic beam from the within the expansion, allowing the extracted portion of the expansion to continue into the second differentially pumped chamber. In the second differentially pumped chamber, the beam was pulse modulated with a mechanical chopper. The resulting supersonic beam was nearly monoenergetic ($\Delta v/v \leq 1\%$), making a ~4 mm beam spot size on a 1 cm sample, scattering into 2π steradians. A triply differentially pumped, computer-controlled, rotatable detector arm collected the scattered atoms or molecules with angular and temporal resolution. Once inside the detector, the probe atoms or molecules were ionized by electron bombardment between the differentially pumped detector regions, then mass selected using a quadrupole mass

spectrometer, and detected with an electron multiplier followed by pulse counting electronics. The flight path was 1.5277 m, the sum of the chopper-to-sample path of 0.4996 m and the sample to ionizer path of 1.0281 m. For our experiments we used a helium supersonic beam to probe the Nb(100) surface.

Diffraction scans were obtained by square-wave beam modulation, with a 50% duty cycle and a rotating the detector at 0.2° increments with fixed incident angle and energy, with an overall instrument angular resolution of 0.20°. The beam was characterized by time-of-flight (TOF) measurements made with a single-slit chopping, 1% duty cycle pattern. The Nb(100) crystal was mounted on a six-axis manipulator within the HAS instrument's sample chamber. This manipulator enables control over the incident angle, θ_i, azimuthal angle, ϕ, and tilt, χ, with respect to the scattering plane. Electron bombardment heating and a closed-cycle He refrigerator modulated the sample temperature within a range of 300 to 2300 K. Surface Preparation Laboratory (the Netherlands) provided the Nb(100) sample (99.99% purity, ~0.1° cut accuracy), which we then cleaned in the HAS instrument by cycles of annealing and flashing up to 1900 K, in addition to sputtering with 1 keV Ne^+ ions (3 μA maximum) and exposing to backfilled O at a surface temperature (T_S) of ~1200 K to remove surface C as desorbed CO. These temperatures were measured with a pyrometer. Impurities identified by *in situ* AES were C, B, S, and N; these were removed by the combination of annealing, flashing, sputtering, and 1200 K T_S exposure to O. We continued the cleaning cycles until only Nb and O was present on the surface in the appropriate ratio, as confirmed by AES, and until the surface was smooth enough for high-intensity He diffraction. Due to the annealing, flashing, sputtering and O exposure process described above, the surface oxide reconstructed (3×1)-O/Nb(100) surface formed naturally and spontaneously. The (3×1)-O/Nb(100) surface structure and cleanliness was confirmed with AES,

LEED, and helium diffraction. During data collection, the Nb sample was periodically flashed to about 1200 K to eliminate unwanted surface adsorbates. Debye-Waller data was obtained by aligning the crystal at each surface temperature and taking diffraction scans across the specular peak. Each Debye-Waller measurement consisted of varying surface temperature up and then down a chosen temperature range, aligning the crystal and taking diffraction scan over specular at each temperature. These measurements were taken from the lower limit, ~550 K, of the chosen temperature range to the upper limit, ~750 K, then immediately back down to the lower limit. The lower temperature limit was determined as the lowest temperature free of substantial background gas adsorption in the time it took to align and take a diffraction scan. The temperature during the Debye-Waller measurement heating the crystal was measured with a type K thermocouple attached to the plate holding the crystal.

The work function of the (3×1)-O/Nb(100) surface oxide reconstruction was calculated from ultraviolet photoelectron spectroscopy (UPS) measurements taken in a separate UHV chamber. The (3×1)-O structure was formed on a second Nb(100) single crystal, and the surface cleanliness was confirmed with AES. The UPS measurements were collected using a helium discharge lamp (Specs UVS 10/35) optimized for He I photon emission (21.22 eV) positioned 45° above the sample plane. The photoemission spectra were collected using a cylindrical mirror analyzer (Staib DESA 100). The low kinetic energy portion of the UPS spectrum was obtained by applying a negative voltage to the Nb(100) sample with an external DC source (Agilent E3612A).

6.3 Theoretical Background

To study the (3×1)-O/Nb(100) surface, we performed density-functional theory (DFT) calculations using open-source planewave software JDFTx.[162,163] We implemented ultrasoft

pseudopotentials,[192] using an effective temperature of 20 milli-Hartree and a Fermi function to determine electronic occupancies. The exchange-correlation energy was approximated using the Perdew-Burke-Ernzerhof functional (PBE).[165] Our calculations employed planewave cutoff energies of 20 Hartree and 100 Hartree for the electronic wavefunctions and density, respectively. We computed properties of a slab with six layers of niobium atoms and two layers of oxygen atoms along the surface-normal direction and truncated Coulomb potentials to increase the accuracy of calculated surface properties.[166] We calculated phonon properties using the finite-difference supercell method, perturbing atoms by 0.1 Bohrs to calculate the real space interatomic force constant matrix directly.[168] To improve the accuracy of the phonon modes calculated, we expanded the dynamical matrix by adding sub-matrices corresponding to the dynamical matrix calculated for Nb bulk. We added enough elements to the matrix to emulate a slab 10 layers deeper than the original one. Interatomic force constant matrices for the slab were evaluated in a 1×3×1 supercell with a *k*-space sampling density equal to the unit cell's sampling of 3×9×1 *k*-points. For the Nb bulk, we evaluated in a 4×4×4 supercell with *k*-space sampling density equal to the unit cell's sampling of the 12×12×12 *k*-points.

6.4 Results and Discussion

The (3×1)-O/Nb(100) surface oxide reconstruction was prepared and confirmed with HAS diffraction and AES in Figure 6.1(a) and Figure 6.1(b) respectively. Figure 6.1(a) contains a diffraction scan taken at 550 K along the <$\bar{1}$00>, $\overline{\Gamma X}$ azimuthal direction. Each peak occurs when the Von Laue condition holds true, or when

$$\Delta K = k_i\left(\sin\theta_i - \sin\theta_f\right) = G_{mn}, \tag{6.1}$$

where the surface-parallel component of the He wavevector k_i changes by ΔK; the initial and final scattering angles, relative to surface normal, are θ_i and θ_f, respectively; and G_{mn} is a linear combination of reciprocal surface lattice vectors.[8,148,188]

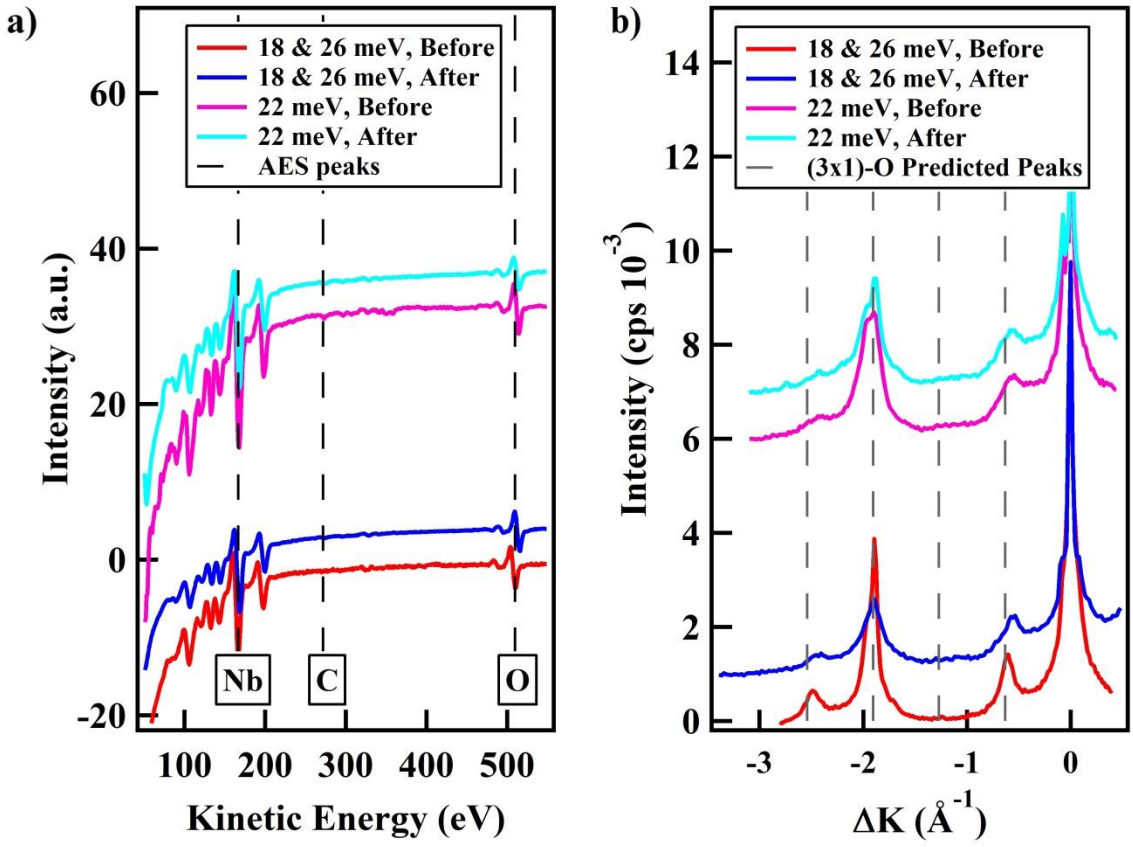

Figure 6.1: Representative (a) AES adjusted for scale and staggered for visual clarity as well as (b) He atom diffraction spectra along the <$\bar{1}$00> symmetry axis ; AES and diffraction spectra were taken before and after the DW measurements on (3x1)-O/Nb(100) surface. In panel (a), the primary Nb peak is evident at 167 eV, the secondary Nb peak at 192 eV, and the primary O (503 eV) peak is present in the appropriate range, O/Nb ~ 0.15 – 0.3, for the (3x1)-

Thermal attenuation occurs due to thermally excited phonons disturbing the electron density at the surface. This thermal attenuation is described by the following relation,

$$I(T_S) = I(0)e^{-2W(T_S)}, \tag{6.2}$$

where 2W is the DW factor. The traditional definition of the DW factor is

$$2W(T_S) = \langle \Delta k \cdot u(T_S) \rangle^2, \tag{6.3}$$

where Δk is the change in wavevector of the scattered He and u is mean squared displacement (MSD) of the surface atoms.[26] Recently, Manson et al. has derived a relationship between 2W and the surface EPC constant via reasonable approximations, yielding the direct proportionality for metal surfaces above the surface Debye temperature,

$$\lambda_{HAS} \cong -\frac{d \ln I_{00}}{k_B dT_S} \frac{\phi}{6Z} \frac{k_F^2}{k_{iz}^2}, \tag{6.4}$$

where I_{00} is the intensity of the specular reflection, ϕ is the work function, Z is the number of free electrons per atom, k_F is the Fermi wavevector, and k_{iz} is the surface perpendicular (z) component of the incident helium incident wavevector.[15,159] In a DW measurement, diffraction scans were taken over the specular peak up and down the temperature range, ~550 K to ~750 K, for three beam energies (Figure 2). These DW runs were taken immediately following and after confirmation of structure and composition with He diffraction and AES respectively, ensuring cleanliness.

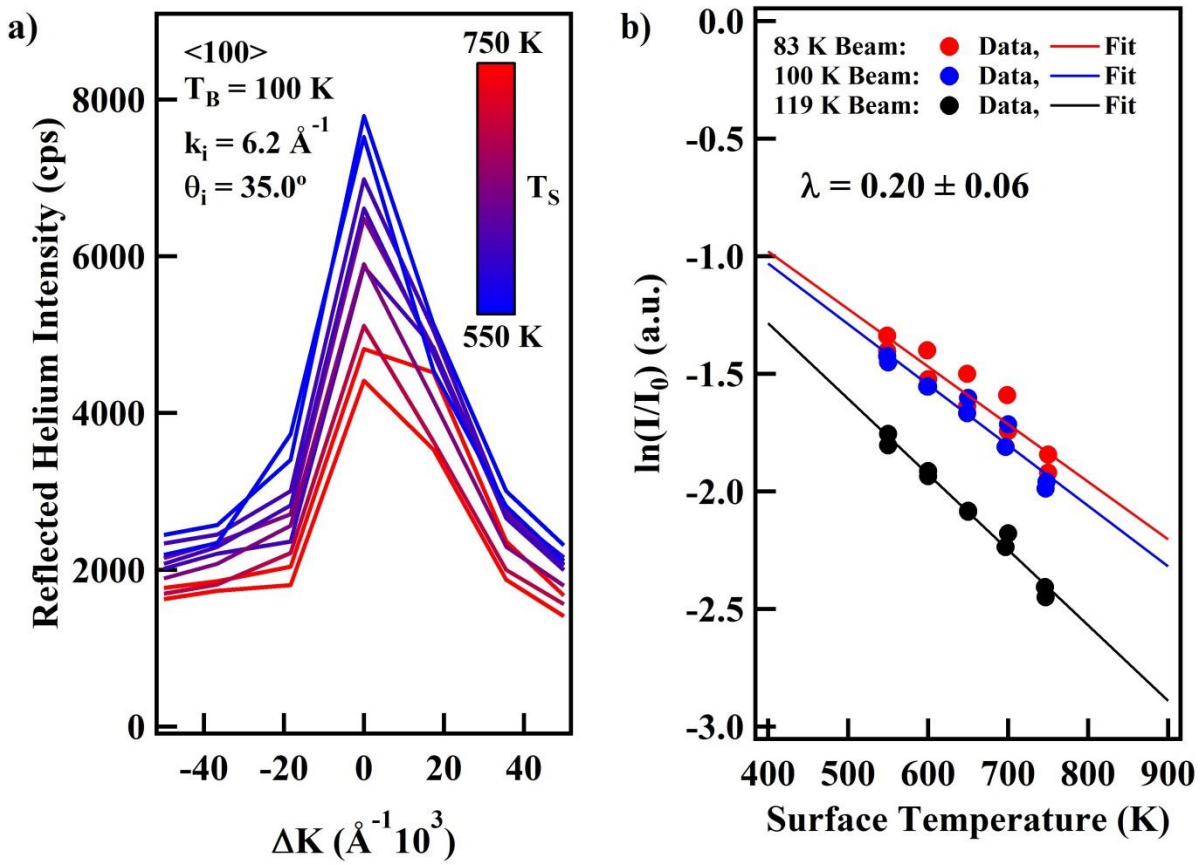

Figure 6.2: Representative thermal attenuation of the specular peak is observed in (a), where diffraction scans through the range were taken proceeding up the temperature range to 750 K and then back down to 550 K. The intensity values are taken from these specular reflections and plotted in (b). In (b) the ln of specular intensity is plotted versus surface temperature for three beam energies. A linear line is fit to the data, providing I_0 from the y-intercept fitting parameter. I_0 is the specular intensity at 0 K with a perfectly still surface. The fit also provides a slope fitting parameter that is equal to $\frac{d \ln I_{00}}{dT_S}$. From this slope and a work function from UPS, average number of free electrons per atom, and estimated Fermi wavevector, we calculate λ = 0.20 ± 0.06 for the (3x1)-O/Nb(100) surface reconstruction.

The beam energies we used were sufficiently low to require the so-called Beeby correction. The Beeby correction accounts for acceleration due to the attractive portion of the helium-surface potential well depth, D.[27] The Beeby approximation is commonly used to correct for this effect, taking into account the acceleration of the helium atom from the helium to surface potential before scattering. In the Beeby approximation, the potential well depth is added to the incident helium beam energy. This quantity can be related to the DW factor by expanding the traditional expression for the DW factor with standard kinematics. Upon substitution, restriction to specular scattering, and rearrangement, the relation,

$$\sigma = -\frac{d(2W)}{dT_S} = 4k_i^2 \frac{d\langle u_z^2 \rangle}{dT_S}\left[\cos^2\theta_i + \frac{D}{E_i}\right], \tag{6.5}$$

is obtained, where σ is the negative slope of a DW linear plot, k_i is the helium incident wavevector, θ_i is incident angle relative to surface normal, D is the helium-surface potential well depth, and E_i is the helium incident energy.[27] Thus, a fit of DW decay, σ, versus $k_i^2\cos^2\theta_i$ yields the helium-surface potential well depth and the first derivative of the mean-square displacement with respect to surface temperature. These diffraction scans and the corresponding plot of σ versus $k_i^2\cos^2\theta_i$ are in Figure 6.3.

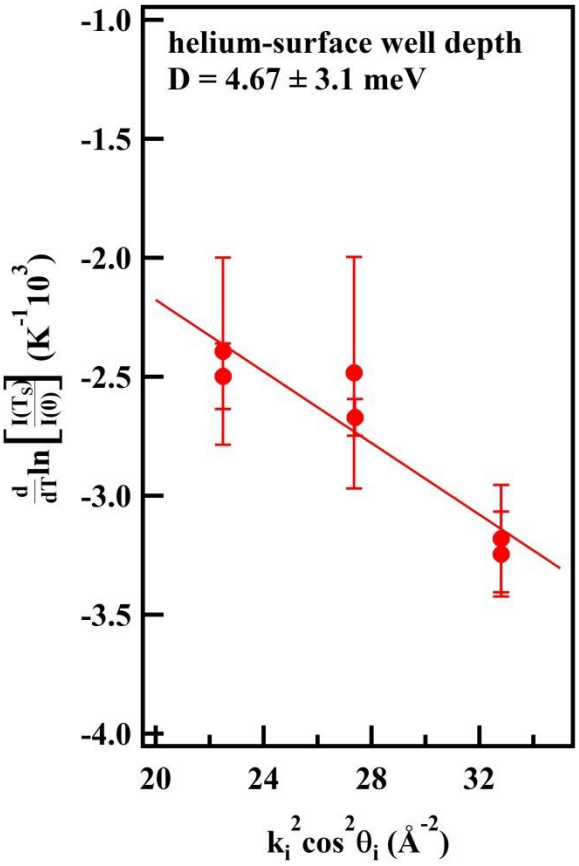

Figure 6.3: A plot of σ versus $k_i^2\cos^2\theta_i$ and its fit provides the helium-surface well depth, 4.7 meV, and the surface Debye temperature, 390 ± 10 K. Obtaining a value for the well depth, D, allows us to correct our incident beam energy in the so called Beeby correction. The surface Debye temperature verifies the DW measurements were made in the high temperature limit of Bose-Einstein phonon population function required for equation 6.3 to apply. Additionally, the Debye temperature is used in calculating the T_c from the measured λ from the McMillan equation.

From the fitting parameters, the helium to surface well depth of 4.7 meV was obtained, and a surface Debye temperature of 357 K was determined from the mean squared displacement with the Debye model.

Complementary DFT calculations of phonon modes provide theoretical MSD values. The HAS intensity-vs-temperature data can be converted into MSD_z-vs-temperature data using the traditional definition of the DW factor (eq. 6.2, 6.3) and the Beeby correction to correct the incident He wavevector.[27,193] The excellent agreement between HAS data and the complementary DFT calculations through the MSD_z can be seen in Figure 6.4.

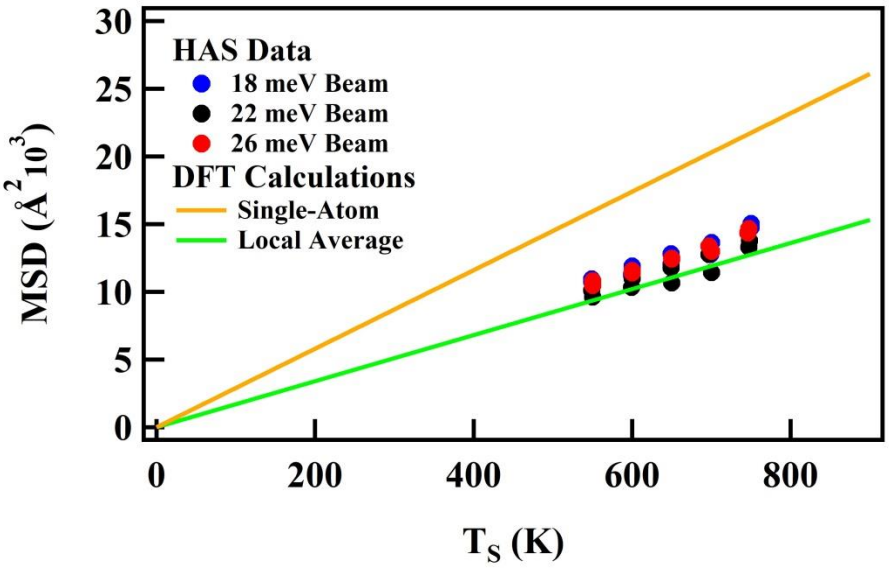

Figure 6.4: Comparison of HAS data and DFT via MSD_z (surface perpendicular portion of the MSD). Upper and lower bounds were calculated averaging over single atoms and local averaging in the unit-cell respectively. The local averaging takes the average over nearest and next nearest neighbors. This takes into account the finite volume of the He atom and the fact that it interacts with multiple surface atoms in a single impulsive scattering event. Thus, the apparent MSD_z calculated from local averaging has excellent agreement with the HAS data.

The lines in Figure 6.4 represent the *apparent* MSD_z calculated with

$$\langle (u_z^2)_a \rangle_T = \frac{1}{p^2} \left\langle \left(\sum_{\kappa=1}^{p} u_z(\kappa) \right)^2 \right\rangle_T, \tag{6.6}$$

where p is the number of atoms on the surface, and $u_z(\kappa)$ is the atomic displacement operator in the normal direction to the surface for the κ-th atom, calculated with

$$u_z(\kappa) = \sqrt{\frac{\hbar}{2Nm_\kappa}} \sum_{\boldsymbol{q}j} \frac{\widehat{a_{\boldsymbol{q}j}} + \widehat{a^\dagger_{-\boldsymbol{q}j}}}{\sqrt{\omega_{\boldsymbol{q}j}}} e^{z\kappa}_{\boldsymbol{q}j} e^{i\boldsymbol{q}\cdot\boldsymbol{r}(\kappa)}, \tag{6.7}$$

where the summation samples phonon modes j at wavevectors $\boldsymbol{q}$ throughout the surface's Brillouin zone. $e^{z\kappa}_{\boldsymbol{q}j}$ is the component of the phonon eigenvector corresponding to the normal displacement of the surface atom of mass m_κ, and the Bose factor $n(\omega_{\boldsymbol{q}j}) = a^\dagger_{-\boldsymbol{q}j} a_{\boldsymbol{q}j}$ weights the displacements of each sampled phonon mode at temperature T.[188]

Following a similar approach to that used for the metallic, unreconstructed Nb(100) surface[120], we considered the range of interaction of the electron density of the He atom compared to the electron density of the atoms on the surface, given the distance between them. The upper bound averages over single atoms in the unit cell, considering a shorter interaction range than expected. The lower bound in Figure 4 uses Equation 5 to average over nearest and next-to-nearest neighbors, which is often used in literature.[120,193]

Before we can use the DW slope to calculate λ, we must choose values for the (3×1)-O/Nb(100)'s work function, number of free electrons per atom, and Fermi wave vector. The (3×1)-O / Nb(100) work function was found to be 4.5 ± 3.8E-2 eV and was calculated by subtracting the width of the UPS spectra from the incident photon energy (21.22 eV) as shown in Fig. 6.5. The secondary electron cutoff (SECO) energy was obtained by calibrating the Fermi level using a Au reference sample.[184,194–196]

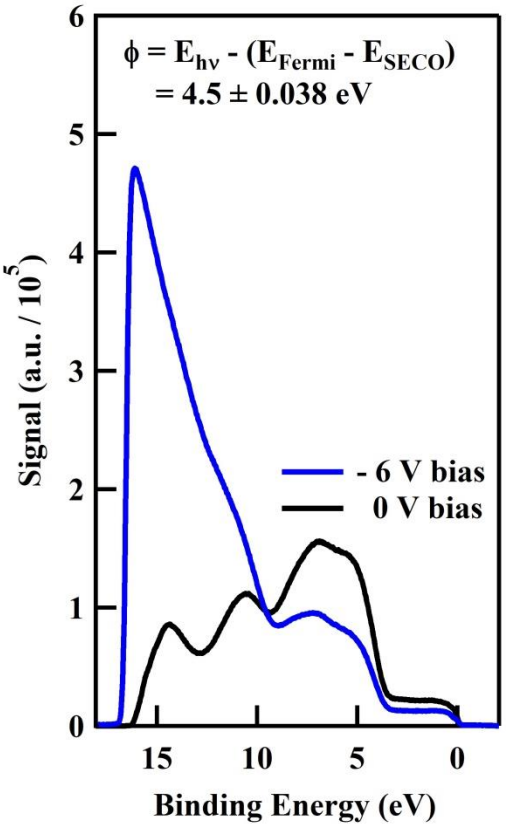

Figure 6.5: UPS spectra of the (3×1)-O / Nb(100) surface using a He I α photon (E_{hv}: 21.22 eV) with no external bias (black curve) and a -6 V bias (blue curve). The work function was calculated using the inset equation. ESECO of 16.74 eV was found by linearly fitting the SECO x-intercept for the UPS spectrum that was collected with a -6 V bias. The binding energy and fermi level was calibrated using a Au reference sample. The reported error for the work function was determined using the energy resolution of the analyzer used in the UPS measurements.

This fits well with literature that agrees that the work function of Nb, 3.99 eV,[8] generally increases with O impurities and oxide reconstructions, but O can have non-monotonic effects on the work function.[197,198] The number of free electrons per atom becomes a weighted average between the number of free electrons of Nb and O atoms in the (3×1)-O unit cell, yielding 2.7 free electrons per atom. The Fermi wave vector was calculated from the number of free electrons using the free electron model to calculate a Fermi wavevector of 0.89 $Å^{-1}$.[8] The DW slope and these chosen values of the work function, number of free electrons per atom, and the Fermi wave vector were used to calculate a λ of 0.20 ± 0.06 for the (3×1)-O/Nb(100) surface.

This is the first recorded value of λ for the (3×1)-O/Nb(100) surface oxide reconstruction. For reference and clarity, the recorded λ values for bulk Nb are 1.15, 1.04, 1.16, and 0.92, almost twice that of the unreconstructed, metallic Nb(100) surface, 0.50 ± 0.08.[120,136,137,139–145] While the interface even without O or reconstruction diminishes EPC, the (3×1)-O reconstruction further diminishes EPC.

Each preparation of the (3×1)-O has different amounts of subsurface oxygen. We can make a plot of measured (3×1)-O EPC versus AES O content to probe the effect of subsurface oxygen on the (3×1)-O reconstruction's EPC (Fig. 6.6).

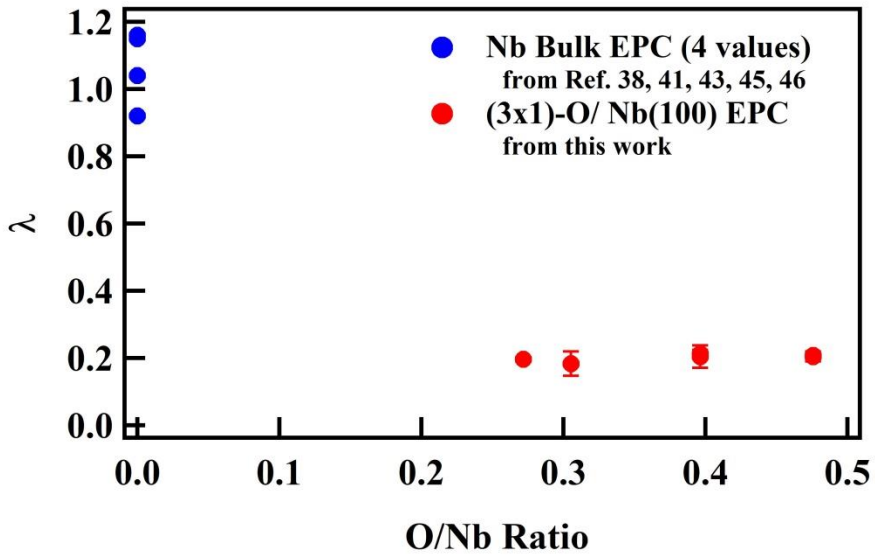

Figure 6.6: The EPC constants were extracted from the DW slopes plotted in Figure 6.2 (b) and plotted against O/Nb from AES. There is an apparent diminishing of λ_S with varying subsurface O. The amount of subsurface oxygen has no significant effect on the SEPC of the (3×1)-O reconstruction. These results show that while the (3×1)-O diminishes the SEPC of the metallic, unreconstructed Nb(100) surface, it also stabilizes the SEPC against the effects of subsurface O.

We find that the amount of subsurface oxygen has no significant effect on the SEPC of the (3×1)-O reconstruction. This is distinct from the effect of subsurface oxygen and carbon on the SEPC of the unreconstructed, metallic Nb(100).[120] The unreconstructed, metallic Nb(100) SEPC had a monotonic decrease with accumulation of subsurface O and C.[120] However, the (3×1)-O

surface oxide reconstruction is not only robust in terms of its high thermal stability and strong interatomic forces, but also in that its SEPC is not significantly altered by subsurface oxygen.[29,70] These results indicate that even if one got rid the problematic oxide[132] within an SRF cavity it would introduce a greater susceptibility to impurities.

To elucidate the significance of the (3×1)-O surface oxide reconstruction's diminished λ, we will estimate the critical temperature of this material. In fact, using the Dynes' version of McMillan's equation along with our measured λ and surface Debye temperature as well as the standard range (0.1 – 0.15) for the renormalized Coulomb repulsion, we find a $T_C \leq$ 6.2E-4 K.[13] We see that the surface oxide reconstruction significantly diminishes the T_C to the point that it is not a feasible superconductor on its own. However, the proximity effect occurs when a normal material and superconducting material are in contact with one another.[199–201] Cooper pairs leak into the normal state imparting some superconductivity, while the exodus of Cooper pairs from the superconducting material diminishes its superconducting properties.[202–204] Thus, the (3×1)-O/Nb(100) interface will diminish the superconductivity of the underlying bulk Nb while its own is increased. Additionally, neither the (3×1)-O superlattice nor the HAS probe depth approach the ~100 nm RF field penetration depth of Nb SRF cavities.[6,15,135,159] The (3×1)-O/Nb(100) does not quench superconductivity, but is expected significantly diminish the overall superconducting performance on the interface and in the underlying, near-surface bulk.

This continues to build a necessary, missing, fundamental understanding of the effects of the surface structure and composition on EPC and superconducting properties. Now we can begin to understand the changes to the surface by carbon impurities, N doping, Sn alloying, and other SRF cavity preparations. These results provide the first measurement of λ of the (3×1)-O/Nb(100) surface oxide reconstruction and distinguishes the effects of structure and

composition of the NbO monolayer surface oxide on the resulting surface superconducting properties.

6.5 Conclusion

The (3×1)-O/Nb(100) surface λ_S was measured to be 0.20 ± 0.06 and its atomic-scale surface structure confirmed, with our findings further supported by consistency between our measured HAS Debye-Waller factors and *ab initio* density-functional theory predictions. The λ_S measured for the (3×1)-O surface reconstruction is further diminished from the metallic, unreconstructed Nb(100) value and further from diminished the reported bulk Nb λ values. Furthermore, the amount of subsurface oxygen has no significant effect on the λ_S of the (3×1)-O reconstruction. Thus, while the metallic, unreconstructed Nb(100) surface is significantly affected by accumulated C and O, the (3×1)-O reconstruction stabilizes its λ_S against the effects of subsurface O. The significance of Nb(100)'s diminished EPC was further elucidated by estimating relevant superconducting properties from the measured λ_S, surface Debye temperature, known material parameters, and well-established equations. Due to the low λ_S, a negligible critical temperature (T_C) ≤ 6.2E-3 K was estimated using the McMillan equation. However, this indicates that at operational temperatures of ~2 K the (3×1)-O/Nb(100) reconstruction is not superconducting on its own. However, the proximity effect indicates that a thin normal metal on top of a superconductor exhibits some superconducting properties while the superconductor's properties are diminished. These results contain the first measurement of (3×1)-O/Nb(100) λ_S, distinguish the effects of surface structure and chemical composition on λ_S, and indicate that the (3×1)-O/Nb(100) surface has diminished superconducting properties relative to the unreconstructed, metallic Nb(100) and the Nb bulk.

Chapter 7

Conclusion and Future Directions

This thesis reports the first measurement of high temperature (3x1)-O/Nb(100) structure as well as its phonon dispersions and interatomic forces. Furthermore, it contains the first measurement of SEPC of the metallic, unreconstructed Nb(100) surface and the (3x1)-O/Nb(100) surface oxide reconstruction. In making these measurements, we have brought into effective action helium atom scattering's (HAS) unique capability for *in situ* high temperature measurements of surface structure, vibrational dynamics, and surface electron-phonon coupling (SEPC, λ_S).

These measurements began with the high temperature persistence of the (3x1)-O/Nb(100)'s structure, composition, and order under SRF cavity preparation conditions. A significant driving force for the (3x1)-O/Nb(100)'s thermal stability was elucidated with inelastic HAS TOF measurements and *ab initio* density-functional theory (DFT) calculations, revealing abnormally strong Nb-O and Nb-Nb bonds that make up the characteristic ladder structure. This means the ladder crests of the (3x1)-O/Nb(100) not only introduces new, relatively strong Nb-O interactions, but it significantly strengthens the Nb-Nb interactions. In this way the (3x1)-O/Nb(100) passivates and stabilizes the surface. These results demonstrate the significant role niobium oxides play in the optimization of growth strategies and coating procedures for next–-generation SRF materials.

Next the atomic-scale structure's effect on the superconductivity was investigated using HAS's sensitivity to EPC. HAS simultaneously measured the surface electron-phonon coupling (EPC, SEPC) constant (λ, λ_S) and *in situ* high temperature atomic-scale surface structure of the

unreconstructed, metallic Nb(100) surface as well as the (3x1)-O/Nb(100) oxide reconstruction. *Ab initio* DFT with local averaging agrees well with the HAS data. Furthermore, some variations in subsurface C and O and their effect on the SEPC are discussed. The Nb(100) surface λ_S is 0.50 ± 0.08 while that of the (3x1)-O/Nb(100) surface oxide reconstruction is λ_S is 0.20 ± 0.06. The λ_S measured for the Nb(100) surface is ~1/2 the reported bulk Nb λ values. These results indicate that the Nb(100) surface has decreased superconducting properties relative to the bulk. This study shows that these effects may be due also to the interface itself even without oxygen. Additionally, the λ_S measured for the (3×1)-O surface reconstruction is further diminished from the metallic, unreconstructed Nb(100) value and the reported bulk Nb λ values. Furthermore, varying subsurface O has no significant effect on the λ_S of the (3×1)-O reconstruction. While the metallic, unreconstructed Nb(100) surface is significantly affected by accumulated subsurface C and O, the (3×1)-O reconstruction stabilizes its λ_S against the effects of subsurface O.

While extensive study of potential SRF cavity treatments is underway, the results reported within this thesis have only just begun fundamental studies correlating atomic scale surface structure with changes in the superconducting state. We have already demonstrated the capability to correlate atomic scale surface structure and chemical composition with λ_S for both the unreconstructed, metallic Nb(100) surface and the (3x1)-O/Nb(100) surface oxide reconstruction. These are the first measurements of λ_S at any Nb surface. Furthermore, these results begin building a necessary foundational understanding of the effects of atomic scale surface structure on superconductivity. With this understanding in hand, we plan to investigate changes in atomic scale surface structure from doping, alloying, capping layers, and defects, revealing their effects on surface superconductivity. Furthermore they begin to build a fundamental understanding of the effects of the surface on superconducting properties. Now we

can begin to understand the changes to the surface by carbon impurities, N/Zr doping, Sn alloying, Ag/Zr capping layers and other SRF cavity preparations. These proposed measurements will build upon these results, enabling SRF cavity surfaces by design.

In ongoing work, the effects of various SRF cavity treatments are being replicated on the metallic Nb(100) surface and (3x1)-O/Nb(100) surface oxide reconstruction and then studied with HAS. HAS is especially suited to measure and quantify changes in lattice spacing, defects, disorder, surface reconstructions, grown alloys, and films. Furthermore, the HAS instrument allows precise control of the system. This ongoing work has started with N-doping a (3x1)-O/Nb(100) surface oxide reconstruction. To correlate atomic-scale surface structure and composition with its effect on λ_S, and ultimately benchmark superconducting properties, high resolution helium diffraction will obtain *in situ* high temperature atomic-scale structure, Auger Electron Spectroscopy (AES) will determine chemical composition, and thermal attenutation of helium reflectivity (Debye-Waller measurement) will measure λ_S. Furthermore these measurements will be made before and after treating pristine Nb material surfaces with alloying, doping, capping layers, and defects to mimic SRF cavity treatments. These treatments include Sn/Zr deposition, Zr/N doping, and controlled Zr/Au/Nb_3Sn film growth on Nb single crystals.

Appendix A

Copyright Attribution

Chapter 3 is an adapted version of the article, McMillan, A. A.; Graham, J. D.; Willson, S. A.; Farber, R. G.; **Thompson, C. J**.; Sibener, S. J. Persistence of the Nb(100) Surface Oxide Reconstruction at Elevated Temperatures. Superconductor Science and Technology 2020, 33, 105012, before peer review or editing, as submitted by A. A. McMillan to Superconductor Science and Technology. IOP Publishing Ltd is not responsible for any errors or omissions in this version of the manuscript or any version derived from it. The Version of Record is available online at https://iopscience.iop.org/article/10.1088/1361-6668/abaec0.[29]

Chapter 4 is reproduced from McMillan, A. A.; **Thompson, C. J.**; Kelley, M. M.; Graham, J. D.; Arias, T. A.; and Sibener, S. J. A Combined Helium Atom Scattering and Density-Functional Theory Study of the Nb(100) Surface Oxide Reconstruction: Phonon Band Structures and Vibrational Dynamics. *J. Chem. Phys.* 156, 124702 (2022) with the permission of AIP Publishing. Copyright 2022 The Journal of Chemical Physics.[70]

Chapter 5 is reproduced from **Thompson, C. J**; Van Duinen, M. F.; Kelley, M. M.; Arias, A. A.; Sibener, S. J. Correlating Electron-Phonon Coupling and *in situ* High Temperature Atomic-Scale Surface Structure at the Metallic Nb(100) Surface by Helium Atom Scattering and Density-Functional Theory. *J. Phys. Chem. C* 128, 14, 6149-6157 (2024) with the permission of AIP Publishing. Copyright 2024 The Journal of Physical Chemistry C.[120]

Chapter 6 is reproduced from **Thompson, C. J.**; Van Duinen, M. F.; Mendez, C.; Willson, S. A.; Do, V; Arias, T. A.; Sibener, S. J. Distinguishing the Roles of Atomic-Scale Surface Structure and Chemical Composition in Electron Phonon Coupling of the Nb(100) Surface Oxide Reconstruction. *J. Phys. Chem. C* 128, 25, 10714-10722 (2024) with the permission of AIP Publishing. Copyright 2024 The Journal of Physical Chemistry C.[174]

Bibliography

(1) Somorjai, G. A.; Li, Y. Impact of Surface Chemistry. *Proceedings of the National Academy of Sciences* **2011**, *108* (3), 917–924. https://doi.org/10.1073/pnas.1006669107.

(2) Benedek, G.; Toennies, J. P. *Atomic Scale Dynamics at Surfaces*; Springer Series in Surface Sciences; Springer-Verlag: Berlin, 2018; Vol. 63.

(3) *Atomic and Molecular Beam Methods, Vol. 1*; Scoles, G., Ed.; Oxford University Press: New York, 1988.

(4) *Atomic and Molecular Beam Methods, Vol. 2*; Scoles, G., Ed.; Oxford University Press: New York, 1992.

(5) *Helium Atom Scattering from Surfaces*; Ekkehard Hulpke, Ed.; Springer-Verlag: Berlin, 1992; Vol. 27.

(6) Padamsee, H.; Knobloch, J.; Hays, T. *RF Superconductivity for Accelerators*; Wiley Series in Beam Physics and Accelerator Technology; John Wiley & Sons, Inc.: Cornell University, Ithaca, New York, 1998.

(7) Porter, R.; Banerjee, N.; Liepe, M. Dynamic Temperature Mapping of Nb_3Sn Cavities. *Proceedings of the 20th International Conference on RF Superconductivity* **2022**, *SRF2021*, 5 pages, 1.518 MB. https://doi.org/10.18429/JACOW-SRF2021-SUPCAV003.

(8) Ashcroft, N. W.; Mermin, N. D. *Solid State Physics*; Brookes/Cole, a part of Cengage Learning, 1976.

(9) Charles Kittel. *Introduction to Solid State Physics*, Sixth Edition.; John Wiley & Sons, Inc., 1986.

(10) Grimvall, G. *The Electron-Phonon Interaction in Metals*; Series of Monographs on Selected Topics in Solid State Physics; North-Holland Publishing Company, 1981; Vol. 16.

(11) Henzler, M. LEED Studies of Surface Imperfections. *Applications of Surface Science* **1982**, *11–12*, 450–469. https://doi.org/10.1016/0378-5963(82)90092-7.

(12) Kress, W.; de Wette, F. W. *Surface Phonons*; Springer Series in Surface Sciences; Springer-Verlag: Berlin, 1991.

(13) Dynes, R. C. McMillan's Equation and the Tc of Superconductors. *Solid State Commun.* **1972**, *10* (7), 615–618.

(14) Manson, J. R.; Benedek, G.; Miret-Arte, S. Electron−Phonon Coupling Strength at Metal Surfaces Directly Determined from the Helium Atom Scattering Debye−Waller Factor. *J. Phys. Chem. Lett* **2016**, *7*, 32. https://doi.org/10.1021/acs.jpclett.6b00139.

(15) Manson, J. R.; Benedek, G.; Miret-Artés, S. Correction to "Electron–Phonon Coupling Strength at Metal Surfaces Directly Determined from the Helium Atom Scattering Debye–Waller Factor." *J. Phys. Chem. Lett.* **2016**, *7* (9), 1691–1691. https://doi.org/10.1021/acs.jpclett.6b00789.

(16) Tinkham, M. *Introduction to Superconductivity*; Robert E. Krieger Publishing Company, 1980.

(17) Liarte, D. B.; Posen, S.; Transtrum, M. K.; Catelani, G.; Liepe, M.; Sethna, J. P. Theoretical Estimates of Maximum Fields in Superconducting Resonant Radio Frequency Cavities: Stability Theory, Disorder, and Laminates. *Supercond. Sci. Technol.* **2017**, *30* (3), 033002. https://doi.org/10.1088/1361-6668/30/3/033002.

(18) Morse, M. Supersonic Beam Sources. In *Atomic, Molecular, and Optical Physics: Atoms and Molecules*; Experimental Methods in the Physical Sciences; Academic Press: Department of Chemistry, University of Utah, Salt Lake City, UT, 1996; Vol. 29B, pp 21–47.
(19) Estermann, I.; Stern, O. Beugung von Molekularstrahlen. *Z. Physik* **1930**, *61* (1), 95–125. https://doi.org/10.1007/BF01340293.
(20) Esbjerg, N.; Nørskov, J. K. Dependence of the He-Scattering Potential at Surfaces on the Surface-Electron-Density Profile. *Phys. Rev. Lett.* **1980**, *45* (10), 807–810. https://doi.org/10.1103/PhysRevLett.45.807.
(21) Farías, D.; Rieder, K.-H. Atomic Beam Diffraction from Solid Surfaces. *Reports on Progress in Physics* **1998**, *61* (12), 1575–1664. https://doi.org/10.1088/0034-4885/61/12/001.
(22) Holst, B.; Alexandrowicz, G.; Avidor, N.; Benedek, G.; Bracco, G.; Ernst, W. E.; Farías, D.; Jardine, A. P.; Lefmann, K.; Manson, J. R.; Marquardt, R.; Artés, S. M.; Sibener, S. J.; Wells, J. W.; Tamtögl, A.; Allison, W. Material Properties Particularly Suited to Be Measured with Helium Scattering: Selected Examples from 2D Materials, van Der Waals Heterostructures, Glassy Materials, Catalytic Substrates, Topological Insulators and Superconducting Radio Frequency Materials. *Physical Chemistry Chemical Physics* **2021**, *23* (13), 7653–7672. https://doi.org/10.1039/D0CP05833E.
(23) Benedek, G.; Toennies, J. P. *Atomic Scale Dynamics at Surfaces Theory and Experimental Studies with Helium Atom Scattering*; Springer Series in Surface Sciences; Springer-Verlag GmbH Germany, part of SPringer Nature, 2018; Vol. 63.
(24) Lapujoulade, J.; Lejay, Y.; Armand, G. The Thermal Attenuation of Coherent Elastic Scattering of Noble Gas from Metal Surfaces. *Surface Science* **1980**, *95*, 107–130.
(25) Comsa, G. Coherence Length and/or Transfer Width? *Surface Science* **1979**, *81*, 57–68.
(26) Levi, A. C.; Suhl, H. Quantum Theory of Atom-Surface Scattering: Debye-Waller Factor. *Surface Science* **1979**, *88* (1), 221–254. https://doi.org/10.1016/0039-6028(79)90577-6.
(27) Beeby, J. L. The Scattering of Helium Atoms from Surfaces. *J. Phys. C: Solid State Phys.* **1971**, *4* (18), L359. https://doi.org/10.1088/0022-3719/4/18/001.
(28) Hund, Z. M.; Nihill, K. J.; Campi, D.; Wong, K. T.; Lewis, N. S.; Bernasconi, M.; Benedek, G.; Sibener, S. J. Vibrational Dynamics and Band Structure of Methyl-Terminated Ge(111). *J. Chem. Phys.* **2015**, *143* (12), 124705. https://doi.org/10.1063/1.4931178.
(29) McMillan, A. A.; Graham, J. D.; Willson, S. A.; Farber, R. G.; Thompson, C. J.; Sibener, S. J. Persistence of the Nb(100) Surface Oxide Reconstruction at Elevated Temperatures. *Supercond. Sci. Technol.* **2020**, *33* (10), 105012. https://doi.org/10.1088/1361-6668/abaec0.
(30) Padamsee, H. The Science and Technology of Superconducting Cavities for Accelerators. *Superconductor Science and Technology*. 2001, pp R28–R51. https://doi.org/10.1088/0953-2048/14/4/202.
(31) Reece, C. E. Continuous Wave Superconducting Radio Frequency Electron Linac for Nuclear Physics Research. *Physical Review Accelerators and Beams*. 2016, p 124801. https://doi.org/10.1103/PhysRevAccelBeams.19.124801.
(32) Posen, S.; Hall, D. L. Nb3Sn Superconducting Radiofrequency Cavities: Fabrication, Results, Properties, and Prospects. *Superconductor Science and Technology*. 2017, p 033004. https://doi.org/10.1088/1361-6668/30/3/033004.

(33) Ford, D. C.; Cooley, L. D.; Seidman, D. N. Suppression of Hydride Precipitates in Niobium Superconducting Radio-Frequency Cavities. *Superconductor Science and Technology* **2013**, *26* (10), 105003. https://doi.org/10.1088/0953-2048/26/10/105003.
(34) Ma, Q.; Ryan, P.; Freeland, J. W.; Rosenberg, R. A. Thermal Effect on the Oxides on Nb(100) Studied by Synchrotron-Radiation x-Ray Photoelectron Spectroscopy. *Journal of Applied Physics* **2004**, *96* (12), 7675–7680. https://doi.org/10.1063/1.1809774.
(35) Posen, S.; Liepe, M. Advances in Development of Nb3Sn Superconducting Radio-Frequency Cavities. *Physical Review Special Topics - Accelerators and Beams* **2014**, *17* (11), 112001. https://doi.org/10.1103/PhysRevSTAB.17.112001.
(36) Romanenko, A.; Grassellino, A.; Barkov, F.; Ozelis, J. P. Effect of Mild Baking on Superconducting Niobium Cavities Investigated by Sequential Nanoremoval. *Physical Review Special Topics - Accelerators and Beams* **2013**, *16* (1), 012001. https://doi.org/10.1103/PhysRevSTAB.16.012001.
(37) Grassellino, A.; Romanenko, A.; Sergatskov, D.; Melnychuk, O.; Trenikhina, Y.; Crawford, A.; Rowe, A.; Wong, M.; Khabiboulline, T.; Barkov, F. Nitrogen and Argon Doping of Niobium for Superconducting Radio Frequency Cavities: A Pathway to Highly Efficient Accelerating Structures. *Superconductor Science and Technology* **2013**, *26* (10), 102001. https://doi.org/10.1088/0953-2048/26/10/102001.
(38) Grassellino, A.; Romanenko, A.; Trenikhina, Y.; Checchin, M.; Martinello, M.; Melnychuk, O. S.; Chandrasekaran, S.; Sergatskov, D. A.; Posen, S.; Crawford, A. C.; Aderhold, S.; Bice, D. Unprecedented Quality Factors at Accelerating Gradients up to 45 MVm-1 in Niobium Superconducting Resonators via Low Temperature Nitrogen Infusion. *Superconductor Science and Technology* **2017**, *30* (9), 094004. https://doi.org/10.1088/1361-6668/aa7afe.
(39) Lee, J.; Mao, Z.; He, K.; Sung, Z. H.; Spina, T.; Baik, S.-I.; Hall, D. L.; Liepe, M.; Seidman, D. N.; Posen, S. Grain-Boundary Structure and Segregation in Nb3Sn Coatings on Nb for High-Performance Superconducting Radiofrequency Cavity Applications. *Acta Materialia* **2020**, *188*, 155–165. https://doi.org/10.1016/j.actamat.2020.01.055.
(40) Becker, C.; Posen, S.; Groll, N.; Cook, R.; Schlepütz, C. M.; Hall, D. L.; Liepe, M.; Pellin, M.; Zasadzinski, J.; Proslier, T. Analysis of Nb3Sn Surface Layers for Superconducting Radio Frequency Cavity Applications. *Applied Physics Letters* **2015**, *106* (8), 082602. https://doi.org/10.1063/1.4913617.
(41) Trenikhina, Y.; Posen, S.; Romanenko, A.; Sardela, M.; Zuo, J.-M.; Hall, D. L.; Liepe, M. Performance-Defining Properties of Nb3Sn Coating in SRF Cavities. *Superconductor Science and Technology* **2018**, *31* (1), 015004. https://doi.org/10.1088/1361-6668/aa9694.
(42) Dickey, J. M.; Strongin, M.; Kammerer, O. F. Studies of Thin Films of Nb3Sn on Nb. *Journal of Applied Physics* **1971**, *42* (13), 5808–5820. https://doi.org/10.1063/1.1660015.
(43) Porter, R. D.; Arias, T.; Cueva, P.; Hall, D. L.; Liepe, M.; Maniscalco, J. T.; Muller, D. A.; Sitaraman, N. Next Generation Nb3Sn SRF Cavities for Linear Accelerators. *29th Linear Accelerator Conference* **2018**, 462–465. https://doi.org/10.18429/JACoW-LINAC2018-TUPO055.
(44) Kneisel, P.; Stoltz, O.; Halbritter, J. Measurements of Superconducting Nb3Sn Gavities in the GHz Range. *IEEE Transactions on Magnetics* **1979**, *15* (1), 21–24. https://doi.org/10.1109/TMAG.1979.1060193.

(45) Arnolds, G.; Proch, D. Measurement on a Nb3Sn Structure for Linear Accelerator Application. *IEEE Transactions on Magnetics* **1977**, *13* (1), 500–503. https://doi.org/10.1109/TMAG.1977.1059387.
(46) Posen, S.; Liepe, M. Stoichiometric Nb3Sn in First Samples Coated at Cornell. *15th Conference on RF Superconductivity* **2011**, 886–889.
(47) Farrell, H. H.; Isaacs, H. S.; Strongin, M. The Interaction of Oxygen and Nitrogen with the Niobium (100) Surface: II. Reaction Kinetics. *Surface Science* **1973**, *38*, 31–52.
(48) Farrell, H. H.; Strongin, M. The Interaction of Oxygen and Nitrogen with the Niobium (100) Surface: I. Morphology. *Surface Science* **1973**, *38*, 18–30.
(49) An, B.; Fukuyama, S.; Yokogawa, K.; Yoshimura, M. Surface Structures of Clean and Oxidized Nb(100) by LEED, AES, and STM. *Physical Review B* **2003**, *68* (11), 115423. https://doi.org/10.1103/PhysRevB.68.115423.
(50) Lindau, I.; Spicer, W. E. Oxidation of Nb as Studied by the Uv-Photoemission Technique. *Journal of Applied Physics* **1974**, *45* (9), 3720–3725. https://doi.org/10.1063/1.1663849.
(51) Wang, Y.; Wei, X.; Tian, Z.; Cao, Y.; Zhai, R.; Ushikubo, T.; Sato, K.; Zhuang, S. An AES, UPS and HREELS Study of the Oxidation and Reaction of Nb(110). *Surface Science* **1997**, *372*, L285–L290. https://doi.org/10.1016/S0039-6028(96)01253-8.
(52) Veit, R. D.; Kautz, N. A.; Farber, R. G.; Sibener, S. J. Oxygen Dissolution and Surface Oxide Reconstructions on Nb(100). *Surface Science* **2019**, *688*, 63–68. https://doi.org/10.1016/j.susc.2019.06.004.
(53) Uehara, Y.; Fujita, T.; Iwami, M.; Ushioda, S. Single NbO Nano-Crystal Formation on Low Temperature Annealed Nb(001) Surface. *Surface Science* **2001**, *472*, 59–62. https://doi.org/10.1016/S0039-6028(00)00922-5.
(54) Arfaoui, I.; Cousty, J.; Guillot, C. A Model of the NbOx≈1 Nanocrystals Tiling a Nb(110) Surface Annealed in UHV. *Surface Science* **2004**, *557*, 119–128. https://doi.org/10.1016/j.susc.2004.03.025.
(55) Musket, R. G.; McLean, W.; Colmenares, C. A.; Makowiecki, D. M.; Siekhaus, W. J. Preparation of Atomically Clean Surfaces of Selected Elements: A Review. *Applications of Surface Science* **1982**, *10* (2), 143–207. https://doi.org/10.1016/0378-5963(82)90142-8.
(56) Franchy, R.; Bartke, T. U.; Gassmann, P. The Interaction of Oxygen with Nb(110) at 300, 80 and 20 K. *Surface Science* **1996**, *366* (1), 60–70. https://doi.org/10.1016/0039-6028(96)00781-9.
(57) Pantel, R.; Bujor, M.; Bardolle, J. Continuous Measurement of Surface Potential Variations during Oxygen Adsorption on the (100), (110) and (111) Faces of Niobium Using Mirror Electron Microscope. *Surface Science* **1977**, *62* (2), 589–609. https://doi.org/10.1016/0039-6028(77)90103-0.
(58) Dawson, P. H.; Tam, W.-C. The Interaction of Oxygen with Polycrystalline Niobium Studied Using AES and Low-Energy SIMS. *Surface Science* **1979**, *81* (2), 464–478. https://doi.org/10.1016/0039-6028(79)90113-4.
(59) Usami, S.; Tominaga, N.; Nakajima, T. AES-LEED Study of Adsorption of Common Gases on the (100) Planes W and Nb. *Vacuum* **1976**, *27*, 11–16. https://doi.org/10.1016/0042-207x(76)90217-7.
(60) Hulpke, E.; Hüppauff, M.; Smilgies, D.-M.; Kulkarni, A. D.; de Wette, F. W. Lattice Dynamics of the Niobium (001) Surface. *Physical Review B* **1992**, *45* (4), 1820–1828. https://doi.org/10.1103/PhysRevB.45.1820.

(61) Hulpke, E. Introduction. In *Helium Atom Scattering from Surfaces*; Hulpke, E., Ed.; Springer Series in Surface Science; Springer-Verlag: Berlin, 1992; Vol. 27, pp 1–4. https://doi.org/10.1007/978-3-662-02774-5.
(62) Meyer, E.; Hug, H. J.; Bennewitz, R. *Scanning Probe Microscopy: The Lab on a Tip*; Advanced texts in physics; Springer-Verlag: Berlin, 2004. https://doi.org/10.1016/j.elspec.2004.02.002.
(63) Gans, B.; Knipp, P. A.; Koleske, D. D.; Sibener, S. J. Surface Dynamics of Ordered Cu3Au(001) Studied by Elastic and Inelastic Helium Atom Scattering. *Surface Science* **1992**, *264*, 81–94. https://doi.org/10.1016/0368-2048(90)80226-Z.
(64) Li, Y.; An, B.; Xu, X.; Fukuyama, S.; Yokogawa, K.; Yoshimura, M. Surface Structure of Niobium-Dioxide Overlayer on Niobium(100) Identified by Scanning Tunneling Microscopy. *Journal of Applied Physics* **2001**, *89* (9), 4772–4776. https://doi.org/10.1063/1.1364649.
(65) Engel, T.; Rieder, K.-H. Structural Studies of Surfaces with Atomic and Molecular Beam Diffraction. In *Structural Studies of Surfaces*; Springer Tracts in Modern Physics; Springer-Verlag: Berlin, 1982; Vol. 91, pp 55–180. https://doi.org/10.1007/bfb0041342.
(66) Lapujoulade, J.; Lejay, Y.; Armand, G. The Thermal Attentuation of Coherent Elastic Scattering of Noble Gas from Metal Surfaces. *Surface Science* **1980**, *95*, 107–130.
(67) Becker, J. S.; Brown, R. D.; Johansson, E.; Lewis, N. S.; Sibener, S. J. Helium Atom Diffraction Measurements of the Surface Structure and Vibrational Dynamics of CH3-Si(111) and CD3-Si(111) Surfaces. *Journal of Chemical Physics* **2010**, *133* (10), 104705. https://doi.org/10.1063/1.3483465.
(68) Veit, R. D.; Farber, R. G.; Sitaraman, N. S.; Arias, T. A.; Sibener, S. J. Suppression of Nano-Hydride Growth on Nb(100) Due to Nitrogen Doping. *Journal of Chemical Physics* **2020**, *152*, 214703. https://doi.org/10.1063/5.0007042.
(69) Davis, L. *Handbook of Auger Electron Spectroscopy*, 2nd ed.; Physical Electronics Industries: Eden Prairie, 1976.
(70) McMillan, A. A.; Thompson, C. J.; Kelley, M. M.; Graham, J. D.; Arias, T. A.; Sibener, S. J. A Combined Helium Atom Scattering and Density-Functional Theory Study of the Nb(100) Surface Oxide Reconstruction: Phonon Band Structures and Vibrational Dynamics. *J. Chem. Phys.* **2022**, *156* (12), 124702. https://doi.org/10.1063/5.0085653.
(71) Hamm, R. W.; Hamm, M. E. *Industrial Accelerators and Their Applications*; World Scientific: Singapore, 2012.
(72) Padamsee, H.; Shepard, K. W.; Sundelin, R. Physics and Accelerator Applications of RF Superconductivity. *Annual Review of Particle and Nuclear Science* **1993**, *43*, 635–686.
(73) Finnemore, D. K.; Stromberg, T. F.; Swenson, C. A. Superconducting Properties of High-Purity Niobium. *Physical Review* **1966**, *149* (1), 231–243.
(74) Padamsee, H.; Knobloch, J.; Hays, T. *RF Superconductivity for Accelerators*; Wiley-VCH: New York, 2008.
(75) Gerigk, F. Superconducting RF at CERN: Operation, Projects, and R&D. *IEEE Transactions on Applied Superconductivity* **2018**, *28* (4), 3500205. https://doi.org/10.1109/TASC.2018.2792528.
(76) Broemmelsiek, D.; Chase, B.; Edstrom, D.; Harms, E.; Leibfritz, J.; Nagaitsev, S.; Pischalnikov, Y.; Romanov, A.; Ruan, J.; Schappert, W.; Shiltsev, V.; Thurman-Keup, R.; Valishev, A. Record High-Gradient SRF Beam Acceleration at Fermilab. *New Journal of Physics* **2018**, *20*, 113018. https://doi.org/10.1088/1367-2630/aaec57.

(77) Dhakal, P.; Ciovati, G.; Kneisel, P.; Myneni, G. R. Enhancement in Quality Factor of SRF Niobium Cavities by Material Diffusion. *IEEE Transactions on Applied Superconductivity* **2015**, *25* (3), 3500104. https://doi.org/10.1109/TASC.2014.2359640.
(78) Arfaoui, I.; Guillot, C.; Cousty, J.; Antoine, C. Evidence for a Large Enrichment of Interstitial Oxygen Atoms in the Nanometer-Thick Metal Layer at the NbO/Nb (110) Interface. *Journal of Applied Physics* **2002**, *91* (11), 9319–9323. https://doi.org/10.1063/1.1473699.
(79) Grundner, M.; Halbritter, J. XPS and AES Studies on Oxide Growth and Oxide Coatings on Niobium. *Journal of Applied Physics* **1980**, *51*, 397–405. https://doi.org/10.1063/1.327386.
(80) Sürgers, C.; Schöck, M.; Löhneysen, H. V. Oxygen-Induced Surface Structure of Nb(110). *Surface Science* **2001**, *471* (1–3), 209–218. https://doi.org/10.1016/S0039-6028(00)00908-0.
(81) Li, Y.; An, B.; Fukuyama, S.; Yokogawa, K.; Yoshimura, M. Surface Oxidation of a Nb(100) Single Crystal by Scanning Tunneling Microscopy. In *Materials Characterization*; 2002; Vol. 48, pp 163–167. https://doi.org/10.1016/S1044-5803(02)00204-8.
(82) McMillan, A. A.; Graham, J. D.; Willson, S. A.; Farber, R. G.; Thompson, C. J.; Sibener, S. J. Persistence of the Nb(100) Surface Oxide Reconstruction at Elevated Temperatures. *Superconductor Science and Technology* **2020**, *33*, 105012.
(83) Estermann, I.; Stern, O. Beugung von Molekularstrahlen. *Zeitschrift f{ü}r Physik* **1930**, *61* (1–2), 95–125. https://doi.org/10.1007/BF01340293.
(84) Toennies, J. P. Helium Atom Scattering: A Gentle and Uniquely Sensitive Probe of Surface Structure and Dynamics. *Journal of Physics: Condensed Matter* **1993**, *5*, A25–A40.
(85) Benedek, G.; Toennies, J. P. Helium Atom Scattering Spectroscopy of Surface Phonons: Genesis and Achievements. *Surface Science* **1994**, *299/300*, 587–611.
(86) Dederichs, P. H.; Schober, H. R.; Sellmyer, D. J. *Phonon States of Elements. Electron States and Fermi Surfaces of Alloys*; Hellwege, K.-H., Olsen, J. L., Eds.; Landolt-Börnstein - Group III Condensed Matter 13A; Springer-Verlag: Berlin Heidelberg, 1981. https://doi.org/10.1007/B19988.
(87) Nakagawa, Y.; Woods, A. D. B. Lattice Dynamics of Niobium. *Physical Review Letters* **1963**, *11* (6), 271–274.
(88) Sharp, R. I. The Lattice Dynamics of Niobium I. Measurements of the Phonon Frequencies. *Journal of Physics C: Solid State Physics* **1969**, *2* (3), 421–431. https://doi.org/10.1088/0022-3719/2/3/306.
(89) Sharp, R. I. The Lattice Dynamics of Niobium II. Kohn Anomalies in Niobium. *Journal of Physics C: Solid State Physics* **1969**, *2* (3), 432–443. https://doi.org/10.1088/0022-3719/2/3/307.
(90) Geerlings, P.; De Proft, F.; Langenaeker, W. Conceptual Density Functional Theory. *Chemical Reviews* **2003**, *103* (5), 1874. https://doi.org/10.1021/CR990029P.
(91) Koleske, D. D.; Sibener, S. J. Generation of Pseudorandom Sequences for Use in Cross-correlation Modulation. *Review of Scientific Instruments* **1992**, *63* (8), 3855. https://doi.org/10.1063/1.1143282.
(92) King, B. R.; Patel, H. C.; Gulino, D. A.; Tatarchuk, B. J. Kinetic Measurements of Oxygen Dissolution into Niobium Substrates: In Situ X-Ray Photoelectron Spectroscopy

Studies. *Thin Solid Films* **1990**, *192* (2), 351–369. https://doi.org/10.1016/0040-6090(90)90079-S.
(93) Daccà, A.; Gemme, G.; Mattera, L.; Parodi, R. XPS Analysis of the Surface Composition of Niobium for Superconducting RF Cavities. *Applied Surface Science* **1998**, *126* (3–4), 219–230. https://doi.org/10.1016/S0169-4332(97)00790-3.
(94) Oechsner, H.; Gibers, J.; Füßer, H. J.; Darlinski, A. Phase Transition and Oxide Dissolution Processes in Vacuum-Annealed Anodic Nb2O5/Nb Systems. *Thin Solid Films* **1985**, *124*, 199–210.
(95) Payne, M. C.; Teter, M. P.; Allan, D. C.; Arias, T. A.; Joannopoulos, J. D. Iterative Minimization Techniques for Ab Initio Total-Energy Calculations: Molecular Dynamics and Conjugate Gradients. *Reviews of Modern Physics* **1992**, *64*, 1045–1097.
(96) Sundararaman, R.; Letchworth-Weaver, K.; Schwarz, K. A.; Gunceler, D.; Ozhabes, Y.; Arias, T. A. JDFTx: Software for Joint Density-Functional Theory. *SoftwareX* **2017**, *6*, 278–284. https://doi.org/10.1016/J.SOFTX.2017.10.006.
(97) Perdew, J. P.; Ruzsinszky, A.; Csonka, G. I.; Vydrov, O. A.; Scuseria, G. E.; Constantin, L. A.; Zhou, X.; Burke, K. Restoring the Density-Gradient Expansion for Exchange in Solids and Surfaces. *Physical Review Letters* **2008**, *100*, 136406. https://doi.org/10.1103/PhysRevLett.100.136406.
(98) Garrity, K. F.; Bennett, J. W.; Rabe, K. M.; Vanderbilt, D. Pseudopotentials for High-Throughput DFT Calculations. *Computational Materials Science* **2014**, *81*, 446–452. https://doi.org/10.1016/j.commatsci.2013.08.053.
(99) Brown, A. M.; Sundararaman, R.; Narang, P.; Goddard III, W. A.; Atwater, H. A. Nonradiative Plasmon Decay and Hot Carrier Dynamics: Effects of Phonons, Surfaces, and Geometry. *ACS Nano* **2016**, *10* (1), 957–966. https://doi.org/10.1021/ACSNANO.5B06199.
(100) Marzari, N.; Vanderbilt, D. Maximally Localized Generalized Wannier Functions for Composite Energy Bands. *Physical Review B* **1997**, *56*, 12847–12865.
(101) González-Pedreros, G. I.; Camargo-Martínez, J. A.; Mesa, F. Cooper Pairs Distribution Function for BCC Niobium under Pressure from First-Principles. *Scientific Reports* **2021**, *11*, 7646. https://doi.org/10.1038/s41598-021-87028-x.
(102) Eliashberg, G. M. Interactions between Electrons and Lattice Vibrations in a Superconductor. *Soviet Physics JETP* **1960**, *11* (3), 696–702.
(103) Brown, A. M.; Sundararaman, R.; Narang, P.; Goddard III, W. A.; Atwater, H. A. Ab Initio Phonon Coupling and Optical Response of Hot Electrons in Plasmonic Metals. *Physical Review B* **2016**, *94*, 075120. https://doi.org/10.1103/PhysRevB.94.075120.
(104) Allen, P. B. Neutron Spectroscopy of Superconductors. *Physical Review B* **1972**, *6*, 2577–2579.
(105) Giustino, F.; Cohen, M. L.; Louie, S. G. Electron-Phonon Interaction Using Wannier Functions. *Physical Review B* **2007**, *76*, 165108. https://doi.org/10.1103/PhysRevB.76.165108.
(106) Butler, W. H.; Pinski, I. J.; Allen, P. B. Phonon Linewidths and Electron-Phonon Interaction in Nb. *Physical Review B* **1979**, *19* (7), 3708–3721.
(107) Sklyadneva, I. Y.; Benedek, G.; Chulkov, E. V; Echenique, P. M.; Heid, R.; Bohnen, K. P.; Toennies, J. P. Mode-Selected Electron-Phonon Coupling in Superconducting Pb Nanofilms Determined from He Atom Scattering. *Physical Review Letters* **2011**, *107* (9), 1–4. https://doi.org/10.1103/PhysRevLett.107.095502.

(108) Tamtögl, A.; Kraus, P.; Mayrhofer-Reinhartshuber, M.; Campi, D.; Bernasconi, M.; Benedek, G.; Ernst, W. E. Surface and Subsurface Phonons of Bi(111) Measured with Helium Atom Scattering. *Physical Review B* **2013**, *87* (3), 35410. https://doi.org/10.1103/PhysRevB.87.035410.
(109) Benedek, G.; Bernasconi, M.; Bohnen, K. P.; Campi, D.; Chulkov, E. V; Echenique, P. M.; Heid, R.; Sklyadneva, I. Y.; Toennies, J. P. Unveiling Mode-Selected Electron-Phonon Interactions in Metal Films by Helium Atom Scattering. *Physical Chemistry Chemical Physics* **2014**, *16* (16), 7159–7172. https://doi.org/10.1039/c3cp54834a.
(110) Hofmann, P.; Sklyadneva, I. Y.; Rienks, E. D. L.; Chulkov, E. V. Electron-Phonon Coupling at Surfaces and Interfaces. *New Journal of Physics* **2009**, *11*, 125005. https://doi.org/10.1088/1367-2630/11/12/125005.
(111) Sklyadneva, I. Y.; Benedek, G.; Chulkov, E. V; Echenique, P. M.; Heid, R.; Bohnen, K. P.; Toennies, J. P. Mode-Selected Electron-Phonon Coupling in Superconducting Pb Nanofilms Determined from He Atom Scattering. *Physical Review Letters* **2011**, *107* (9), 1–4. https://doi.org/10.1103/PhysRevLett.107.095502.
(112) Bortolani, V.; Franchini, A.; Garcia, N.; Nizzoli, F.; Santoro, G. Calculation of Potential Cutoff for One-Phonon Atom-Surface Scattering. *Physical Review B* **1983**, *28*, 7358–7361.
(113) Benedek, G.; Bernasconi, M.; Chis, V.; Chulkov, E.; Echenique, P. M.; Hellsing, B.; Toennies, J. P. Theory of Surface Phonons at Metal Surfaces: Recent Advances. *Journal of Physics: Condensed Matter* **2010**, *22*, 084020. https://doi.org/10.1088/0953-8984/22/8/084020.
(114) Kröger, J. Electron-Phonon Coupling at Metal Surfaces. *Reports on Progress in Physics* **2006**, *69*, 899–969. https://doi.org/10.1088/0034-4885/69/4/R02.
(115) Miyake, T.; Petek, H. Atomic Hydrogen Modification of Copper Surfaces Helium Atom Scattering. *Applied Surface Science* **1997**, *121–122*, 138–141.
(116) Van Der Veen, J. F.; Frenken, J. W. M. Dynamics and Melting of Surfaces. *Surface Science* **1986**, *178*, 382–395.
(117) Pluis, B.; Denier van der Gon, A. W.; Frenken, J. W. M.; van der Veen, J. F. Crystal-Face Dependence of Surface Melting. *Physical Review Letters* **1987**, *59* (23), 2678–2681.
(118) Charlesworth, J. P.; MacPhail, I.; Madsen, P. E. Experimental Work on the Niobium-Tin Constitution Diagram and Related Studies. *Journal of Materials Science* **1970**, *5*, 580–603.
(119) Farber, R. G.; Willson, S. A.; Sibener, S. J. Role of Nanoscale Surface Defects on Sn Adsorption and Diffusion Behavior on Oxidized Nb(100). *Journal of Vacuum Science & Technology A* **2021**, *39*, 063212. https://doi.org/10.1116/6.0001374.
(120) Thompson, C. J.; Van Duinen, M. F.; Kelley, M. M.; Arias, T. A.; Sibener, S. J. Correlating Electron–Phonon Coupling and In Situ High-Temperature Atomic-Scale Surface Structure at the Metallic Nb(100) Surface by Helium Atom Scattering and Density Functional Theory. *J. Phys. Chem. C* **2024**. https://doi.org/10.1021/acs.jpcc.4c00852.
(121) Padamsee, H.; Shepard, K. W.; Sundelin, R. Physics and Accelerator Applications of RF Superconductivity. *Annual Review of Nuclear and Particle Science* **1993**, *43* (1), 635–686. https://doi.org/10.1146/annurev.ns.43.120193.003223.
(122) Padamsee, H. The Science and Technology of Superconducting Cavities for Accelerators. *Supercond. Sci. Technol.* **2001**, *14* (4), R28. https://doi.org/10.1088/0953-2048/14/4/202.

(123) Posen, S.; Valles, N.; Liepe, M. Radio Frequency Magnetic Field Limits of Nb and Nb 3 Sn. *Phys. Rev. Lett.* **2015**, *115* (4), 047001. https://doi.org/10.1103/PhysRevLett.115.047001.
(124) Posen, S. Understanding And Overcoming Limitation Mechanisms In Nb3Sn Superconducting Rf Cavities, Cornell University, 2015. https://ecommons.cornell.edu/handle/1813/39470 (accessed 2022-10-02).
(125) Finnemore, D. K.; Stromberg, T. F.; Swenson, C. A. Superconducting Properties of High-Purity Niobium. *Phys. Rev.* **1966**, *149* (1), 231–243. https://doi.org/10.1103/PhysRev.149.231.
(126) Checchin, M.; Grassellino, A.; Martinello, M.; Melnychuk, O.; Posen, S.; Romanenko, A.; Sergatskov, D. *New Insight on Nitrogen Infusion Revealed by Successive Nanometric Material Removal*; FERMILAB-CONF-18-762-TD; Fermi National Accelerator Lab. (FNAL), Batavia, IL (United States), 2018; pp 2665–2667. https://doi.org/10.18429/JACoW-IPAC2018-WEPMK016.
(127) Grassellino, A.; Romanenko, A.; Sergatskov, D.; Melnychuk, O.; Trenikhina, Y.; Crawford, A.; Rowe, A.; Wong, M.; Khabiboulline, T.; Barkov, F. Nitrogen and Argon Doping of Niobium for Superconducting Radio Frequency Cavities: A Pathway to Highly Efficient Accelerating Structures. *Supercond. Sci. Technol.* **2013**, *26* (10), 102001. https://doi.org/10.1088/0953-2048/26/10/102001.
(128) Porter, R.; Arias, T.; Cueva, P.; Hall, D.; Liepe, M.; Maniscalco, J.; Muller, D.; Sitaraman, N. Next Generation Nb3Sn SRF Cavities for Linear Accelerators; JACOW Publishing, Geneva, Switzerland, 2019; pp 462–465. https://doi.org/10.18429/JACoW-LINAC2018-TUPO055.
(129) Ciovati, G.; Myneni, G.; Stevie, F.; Maheshwari, P.; Griffis, D. High Field Q Slope and the Baking Effect: Review of Recent Experimental Results and New Data on Nb Heat Treatments. *Phys. Rev. ST Accel. Beams* **2010**, *13* (2), 022002. https://doi.org/10.1103/PhysRevSTAB.13.022002.
(130) Sitaraman, N. S.; Sun, Z.; Francis, B. L.; Hire, A. C.; Oseroff, T.; Baraissov, Z.; Arias, T. A.; Hennig, R. G.; Liepe, M. U.; Muller, D. A.; Transtrum, M. K.; Center for Bright Beams. Enhanced Surface Superconductivity of Niobium by Zirconium Doping. *Phys. Rev. Applied* **2023**, *20* (1), 014064. https://doi.org/10.1103/PhysRevApplied.20.014064.
(131) Posen, S.; Hall, D. L. Nb3Sn Superconducting Radiofrequency Cavities: Fabrication, Results, Properties, and Prospects. *Supercond. Sci. Technol.* **2017**, *30* (3), 033004. https://doi.org/10.1088/1361-6668/30/3/033004.
(132) Romanenko, A.; Grassellino, A.; Barkov, F.; Ozelis, J. P. Effect of Mild Baking on Superconducting Niobium Cavities Investigated by Sequential Nanoremoval. *Phys. Rev. ST Accel. Beams* **2013**, *16* (1), 012001. https://doi.org/10.1103/PhysRevSTAB.16.012001.
(133) Bardeen, J.; Cooper, L. N.; Schrieffer, J. R. Theory of Superconductivity. *Phys. Rev.* **1957**, *108* (5), 1175–1204. https://doi.org/10.1103/PhysRev.108.1175.
(134) Hulpke, E.; Hüppauff, M.; Smilgies, D.-M.; Kulkarni, A. D.; de Wette, F. W. Lattice Dynamics of the Niobium (001) Surface. *Phys. Rev. B* **1992**, *45* (4), 1820–1828. https://doi.org/10.1103/PhysRevB.45.1820.
(135) An, B.; Fukuyama, S.; Yokogawa, K.; Yoshimura, M. Surface Structures of Clean and Oxidized Nb(100) by LEED, AES, and STM. *Phys. Rev. B* **2003**, *68* (11), 115423. https://doi.org/10.1103/PhysRevB.68.115423.

(136) Butler, W. H.; Smith, H. G.; Wakabayashi, N. Electron-Phonon Contribution to the Phonon Linewidth in Nb: Theory and Experiment. *Phys. Rev. Lett.* **1977**, *39* (16), 1004–1007. https://doi.org/10.1103/PhysRevLett.39.1004.
(137) Shapiro, S. M.; Shirane, G.; Axe, J. D. Measurements of the Electron-Phonon Interaction in Nb by Inelastic Neutron Scattering. *Phys. Rev. B* **1975**, *12* (11), 4899–4908. https://doi.org/10.1103/PhysRevB.12.4899.
(138) Kelley, M. M.; Sundararaman, R.; Arias, T. A. Fully Ab Initio Approach to Inelastic Atom-Surface Scattering. *Phys. Rev. Lett.* **2024**, *132* (1), 016203. https://doi.org/10.1103/PhysRevLett.132.016203.
(139) DeSorbo, W. Effect of Dissolved Gases on Some Superconducting Properties of Niobium. *Phys. Rev.* **1963**, *132* (1), 107–121. https://doi.org/10.1103/PhysRev.132.107.
(140) Koch, C. C.; Scarbrough, J. O.; Kroeger, D. M. Effects of Interstitial Oxygen on the Superconductivity of Niobium. *Phys. Rev. B* **1974**, *9* (3), 888–897. https://doi.org/10.1103/PhysRevB.9.888.
(141) Gupta, M. Electronic Properties and Electron-Phonon Coupling in Zirconium and Niobium Hydrides. *Phys. Rev. B* **1982**, *25* (2), 1027–1038. https://doi.org/10.1103/PhysRevB.25.1027.
(142) Ponosov, Yu. S.; Streltsov, S. V. Measurements of Raman Scattering by Electrons in Metals: The Effects of Electron-Phonon Coupling. *Phys. Rev. B* **2012**, *86* (4), 045138. https://doi.org/10.1103/PhysRevB.86.045138.
(143) Aynajian, P.; Keller, T.; Boeri, L.; Shapiro, S. M.; Habicht, K.; Keimer, B. Energy Gaps and Kohn Anomalies in Elemental Superconductors. *Science* **2008**, *319* (5869), 1509–1512. https://doi.org/10.1126/science.1154115.
(144) Brorson, S. D.; Kazeroonian, A.; Moodera, J. S.; Face, D. W.; Cheng, T. K.; Ippen, E. P.; Dresselhaus, M. S.; Dresselhaus, G. Femtosecond Room-Temperature Measurement of the Electron-Phonon Coupling Constant γ in Metallic Superconductors. *Phys. Rev. Lett.* **1990**, *64* (18), 2172–2175. https://doi.org/10.1103/PhysRevLett.64.2172.
(145) Bennemann, K. H.; Garland, J. W.; Wolfe, H. C.; Douglass, D. H. Theory for Superconductivity in D-Band Metals; Rochester, New York (USA), 1972; pp 103–137. https://doi.org/10.1063/1.2946179.
(146) Wolf, E. L.; Zasadzinski, J.; Osmun, J. W.; Arnold, G. B. Proximity Electron Tunneling Spectroscopy I. Experiments on Nb. *J Low Temp Phys* **1980**, *40* (1), 19–50. https://doi.org/10.1007/BF00115980.
(147) Arnold, G. B.; Zasadzinski, J.; Osmun, J. W.; Wolf, E. L. Proximity Electron Tunneling Spectroscopy. II. Effects of the Induced N-Metal Pair Potential on Calculated S-Metal Properties. *J Low Temp Phys* **1980**, *40* (3), 225–246. https://doi.org/10.1007/BF00117117.
(148) Scoles, G.; Bassi, D.; Buck, U.; Laine, D. *Atomic and Molecular Beam Methods*; Oxford University Press, 1988; Vol. 1.
(149) Scoles, G.; Laine, D.; Valbusa, U. *Atomic and Molecular Beam Methods*; Oxford University Press, 1992; Vol. 2.
(150) Holst, B.; Alexandrowicz, G.; Avidor, N.; Benedek, G.; Bracco, G.; E. Ernst, W.; Farías, D.; P. Jardine, A.; Lefmann, K.; R. Manson, J.; Marquardt, R.; Miret Artés, S.; J. Sibener, S.; W. Wells, J.; Tamtögl, A.; Allison, W. Material Properties Particularly Suited to Be Measured with Helium Scattering: Selected Examples from 2D Materials, van Der Waals Heterostructures, Glassy Materials, Catalytic Substrates, Topological Insulators and

Superconducting Radio Frequency Materials. *Physical Chemistry Chemical Physics* **2021**, *23* (13), 7653–7672. https://doi.org/10.1039/D0CP05833E.
(151) Anemone, G.; Taleb, A. A.; Benedek, G.; Castellanos-Gomez, A.; Farías, D. Electron–Phonon Coupling Constant of 2H-MoS2(0001) from Helium-Atom Scattering. *J. Phys. Chem. C* **2019**, *123* (6), 3682–3686. https://doi.org/10.1021/acs.jpcc.8b12029.
(152) Anemone, G.; Garnica, M.; Zappia, M.; Aguilar, P. C.; Al Taleb, A.; Kuo, C.-N.; Lue, C. S.; Politano, A.; Benedek, G.; de Parga, A. L. V.; Miranda, R.; Farías, D. Experimental Determination of Surface Thermal Expansion and Electron–Phonon Coupling Constant of 1T-PtTe $_2$. *2D Mater.* **2020**, *7* (2), 025007. https://doi.org/10.1088/2053-1583/ab6268.
(153) Benedek, G.; R. Manson, J.; Miret-Artés, S. The Electron–Phonon Coupling Constant for Single-Layer Graphene on Metal Substrates Determined from He Atom Scattering. *Physical Chemistry Chemical Physics* **2021**, *23* (13), 7575–7585. https://doi.org/10.1039/D0CP04729E.
(154) Benedek, G.; Bernasconi, M.; Bohnen, K.-P.; Campi, D.; V. Chulkov, E.; M. Echenique, P.; Heid, R.; Yu. Sklyadneva, I.; P. Toennies, J. Unveiling Mode-Selected Electron–Phonon Interactions in Metal Films by Helium Atom Scattering. *Physical Chemistry Chemical Physics* **2014**, *16* (16), 7159–7172. https://doi.org/10.1039/C3CP54834A.
(155) Benedek, G.; Miret-Artés, S.; Manson, J. R.; Ruckhofer, A.; Ernst, W. E.; Tamtögl, A. Origin of the Electron–Phonon Interaction of Topological Semimetal Surfaces Measured with Helium Atom Scattering. *J. Phys. Chem. Lett.* **2020**, *11* (5), 1927–1933. https://doi.org/10.1021/acs.jpclett.9b03829.
(156) Benedek, G.; Manson, J. R.; Miret-Artés, S. The Electron–Phonon Interaction of Low-Dimensional and Multi-Dimensional Materials from He Atom Scattering. *Advanced Materials* **2020**, *32* (25), 2002072. https://doi.org/10.1002/adma.202002072.
(157) Tamtögl, A.; Kraus, P.; Avidor, N.; Bremholm, M.; Hedegaard, E. M. J.; Iversen, B. B.; Bianchi, M.; Hofmann, P.; Ellis, J.; Allison, W.; Benedek, G.; Ernst, W. E. Electron-Phonon Coupling and Surface Debye Temperature of Bi 2 Te 3 (111) from Helium Atom Scattering. *Phys. Rev. B* **2017**, *95* (19), 195401. https://doi.org/10.1103/PhysRevB.95.195401.
(158) Sklyadneva, I. Yu.; Benedek, G.; Chulkov, E. V.; Echenique, P. M.; Heid, R.; Bohnen, K.-P.; Toennies, J. P. Mode-Selected Electron-Phonon Coupling in Superconducting Pb Nanofilms Determined from He Atom Scattering. *Phys. Rev. Lett.* **2011**, *107* (9), 095502. https://doi.org/10.1103/PhysRevLett.107.095502.
(159) Manson, J. R.; Benedek, G.; Miret-Artés, S. Electron–Phonon Coupling Strength at Metal Surfaces Directly Determined from the Helium Atom Scattering Debye–Waller Factor. *J. Phys. Chem. Lett.* **2016**, *7* (6), 1016–1021. https://doi.org/10.1021/acs.jpclett.6b00139.
(160) Gans, B.; Knipp, P. A.; Koleske, D. D.; Sibener, S. J. Surface Dynamics of Ordered Cu3Au(001) Studied by Elastic and Inelastic Helium Atom Scattering. *Surface Science* **1992**, *264* (1), 81–94. https://doi.org/10.1016/0039-6028(92)90167-5.
(161) Niu, L.; Gaspar, D. J.; Sibener, S. J. Phonons Localized at Step Edges: A Route to Understanding Forces at Extended Surface Defects. *Science* **1995**, *268* (5212), 847–850.
(162) Payne, M. C.; Teter, M. P.; Allan, D. C.; Arias, T. A.; Joannopoulos, J. D. Iterative Minimization Techniques for Ab Initio Total-Energy Calculations: Molecular Dynamics and Conjugate Gradients. *Rev. Mod. Phys.* **1992**, *64* (4), 1045–1097. https://doi.org/10.1103/RevModPhys.64.1045.

(163) Sundararaman, R.; Letchworth-Weaver, K.; Schwarz, K. A.; Gunceler, D.; Ozhabes, Y.; Arias, T. A. JDFTx: Software for Joint Density-Functional Theory. *SoftwareX* **2017**, *6*, 278–284. https://doi.org/10.1016/j.softx.2017.10.006.
(164) Schlipf, M.; Gygi, F. Optimization Algorithm for the Generation of ONCV Pseudopotentials. *Comput. Phys. Commun.* **2015**, *196*, 36–44. https://doi.org/10.1016/j.cpc.2015.05.011.
(165) Perdew, J. P.; Ruzsinszky, A.; Csonka, G. I.; Vydrov, O. A.; Scuseria, G. E.; Constantin, L. A.; Zhou, X.; Burke, K. Restoring the Density-Gradient Expansion for Exchange in Solids and Surfaces. *Phys. Rev. Lett.* **2008**, *100* (13), 136406. https://doi.org/10.1103/PhysRevLett.100.136406.
(166) Sundararaman, R.; Arias, T. A. Regularization of the Coulomb Singularity in Exact Exchange by Wigner-Seitz Truncated Interactions: Towards Chemical Accuracy in Nontrivial Systems. *Phys. Rev. B* **2013**, *87* (16), 165122. https://doi.org/10.1103/PhysRevB.87.165122.
(167) Veit, R. D.; Kautz, N. A.; Farber, R. G.; Sibener, S. J. Oxygen Dissolution and Surface Oxide Reconstructions on Nb(100). *Surface Science* **2019**, *688*, 63–68. https://doi.org/10.1016/j.susc.2019.06.004.
(168) Brown, A. M.; Sundararaman, R.; Narang, P.; Goddard, W. A.; Atwater, H. A. Nonradiative Plasmon Decay and Hot Carrier Dynamics: Effects of Phonons, Surfaces, and Geometry. *ACS Nano* **2016**, *10* (1), 957–966. https://doi.org/10.1021/acsnano.5b06199.
(169) Miyake, T.; Oodake, I.; Petek, H. Lateral Thermal Expansion of Cu(110) Surface Studied with Helium Atom Scattering. *Surface Science* **1999**, *427–428*, 39–43. https://doi.org/10.1016/S0039-6028(99)00230-7.
(170) Farias, D.; Rieder, K.-H. Atomic Beam Diffraction from Solid Surfaces. *Rep. Prog. Phys.* **1998**, *61* (12), 1575. https://doi.org/10.1088/0034-4885/61/12/001.
(171) Lapujoulade, J.; Lejay, Y.; Armand, G. The Thermal Attenuation of Coherent Elastic Scattering of Noble Gas from Metal Surfaces. *Surface Science* **1980**, *95* (1), 107–130. https://doi.org/10.1016/0039-6028(80)90131-4.
(172) Transtrum, M. K.; Catelani, G.; Sethna, J. P. Superheating Field of Superconductors within Ginzburg-Landau Theory. *Phys. Rev. B* **2011**, *83* (9), 094505. https://doi.org/10.1103/PhysRevB.83.094505.
(173) Townsend, P.; Sutton, J. Investigation by Electron Tunneling of the Superconducting Energy Gaps in Nb, Ta, Sn, and Pb. *Phys. Rev.* **1962**, *128* (2), 591–595. https://doi.org/10.1103/PhysRev.128.591.
(174) Thompson, C. J.; Van Duinen, M.; Mendez, C.; Willson, S. A.; Do, V.; Arias, T. A.; Sibener, S. J. Distinguishing the Roles of Atomic-Scale Surface Structure and Chemical Composition in Electron Phonon Coupling of the Nb(100) Surface Oxide Reconstruction. *J. Phys. Chem. C* **2024**, *128* (25), 10714–10722. https://doi.org/10.1021/acs.jpcc.4c02430.
(175) Padamsee, H. The Science and Technology of Superconducting Cavities for Accelerators. *Supercond. Sci. Technol.* **2001**, *14* (4), R28–R51. https://doi.org/10.1088/0953-2048/14/4/202.
(176) Hall, D.; Cueva, P.; Liarte, D.; Liepe, M.; Muller, D.; Porter, R.; Sethna, J. Cavity Quench Studies in Nb3Sn Using Temperature Mapping and Surface Analysis of Cavity Cut-Outs. *Proceedings of the 18th Int. Conf. on RF Superconductivity* **2018**, *SRF2017*, 4 pages, 1.208 MB. https://doi.org/10.18429/JACOW-SRF2017-THPB041.

(177) Reece, C.; Angle, J.; Kelley, M.; Lechner, E.; Palczewski, A.; Stevie, F. Challenges to Reliable Production Nitrogen Doping of Nb for SRF Accelerating Cavities; JACOW Publishing, Geneva, Switzerland, 2022; pp 1311–1314. https://doi.org/10.18429/JACoW-IPAC2022-TUPOTK042.
(178) Ries, R.; Seiler, E.; Gömöry, F.; Medvids, A.; Onufrijevs, P.; Pira, C.; Chyhyrynets, E.; Malyshev, O. B.; Valizadeh, R. Surface Quality Characterization of Thin Nb Films for Superconducting Radiofrequency Cavities. *Supercond. Sci. Technol.* **2022**, *35* (7), 075010. https://doi.org/10.1088/1361-6668/ac7261.
(179) Sitaraman, N. S.; Sun, Z.; Francis, B.; Hire, A. C.; Oseroff, T.; Baraissov, Z.; Arias, T. A.; Hennig, R.; Liepe, M. U.; Muller, D. A.; Transtrum, M. K. Theory of Nb-Zr Alloy Superconductivity and First Experimental Demonstration for Superconducting Radio-Frequency Cavity Applications. arXiv August 22, 2022. http://arxiv.org/abs/2208.10678 (accessed 2022-10-01).
(180) Bardeen, J.; Cooper, L. N.; Schrieffer, J. R. Microscopic Theory of Superconductivity. *Phys. Rev.* **1957**, *106* (1), 162–164. https://doi.org/10.1103/PhysRev.106.162.
(181) Farrell, H. H.; Isaacs, H. S.; Strongin, M. The Interaction of Oxygen and Nitrogen with the Niobium (100) Surface: II. Reaction Kinetics. *Surface Science* **1973**, *38* (1), 31–52. https://doi.org/10.1016/0039-6028(73)90272-0.
(182) Dawson, P. H.; Wing-Cheung Tam. The Interaction of Oxygen with Polycrystalldve Niobium Studied Using Aes and Low-Energy Sims. *Surface Science* **1979**, *81* (2), 464–478. https://doi.org/10.1016/0039-6028(79)90113-4.
(183) Grundner, M.; Halbritter, J. XPS and AES Studies on Oxide Growth and Oxide Coatings on Niobium. *Journal of Applied Physics* **1980**, *51* (1), 397–405. https://doi.org/10.1063/1.327386.
(184) Hu, Z. P.; Li, Y. P.; Ji, M. R.; Wu, J. X. The Interaction of Oxygen with Niobium Studied by XPS and UPS. *Solid State Communications* **1989**, *71* (10), 849–852. https://doi.org/10.1016/0038-1098(89)90210-X.
(185) Rieder, K. H. On the Interaction of Oxygen with Nb(110) and Nb(750). *Applications of Surface Science* **1980**, *4* (2), 183–195. https://doi.org/10.1016/0378-5963(80)90127-0.
(186) Lindau, I.; Spicer, W. E. Oxidation of Nb as Studied by the Uv-photoemission Technique. *Journal of Applied Physics* **1974**, *45* (9), 3720–3725. https://doi.org/10.1063/1.1663849.
(187) Arfaoui, I.; Cousty, J.; Guillot, C. A Model of the NbOx≈1 Nanocrystals Tiling a Nb(110) Surface Annealed in UHV. *Surface Science* **2004**, *557* (1), 119–128. https://doi.org/10.1016/j.susc.2004.03.025.
(188) Benedek, G.; Toennies, J. P. *Atomic Scale Dynamics at Surfaces: Theory and Experimental Studies with Helium Atom Scattering*; Springer Series in Surface Sciences; Springer: Berlin, Heidelberg, 2018; Vol. 63. https://doi.org/10.1007/978-3-662-56443-1.
(189) Luo, N. S.; Ruggerone, P.; Toennies, J. P.; Benedek, G. Electron-Phonon Coupling at Metal Surfaces Probed by Helium Atom Scattering. *Phys. Scr.* **1993**, *T49B*, 584–592. https://doi.org/10.1088/0031-8949/1993/T49B/036.
(190) Benedek, G.; Manson, J. R.; Miret-Artés, S. The Electron–Phonon Coupling Constant for Single-Layer Graphene on Metal Substrates Determined from He Atom Scattering. *Phys. Chem. Chem. Phys.* **2021**, *23* (13), 7575–7585. https://doi.org/10.1039/D0CP04729E.
(191) Benedek, G.; Miret-Artés, S.; Toennies, J. P.; Manson, J. R. Electron–Phonon Coupling Constant of Metallic Overlayers from Specular He Atom Scattering. *J. Phys. Chem. Lett.* **2018**, *9* (1), 76–83. https://doi.org/10.1021/acs.jpclett.7b03047.

(192) Garrity, K. F.; Bennett, J. W.; Rabe, K. M.; Vanderbilt, D. Pseudopotentials for High-Throughput DFT Calculations. *Computational Materials Science* **2014**, *81*, 446–452. https://doi.org/10.1016/j.commatsci.2013.08.053.
(193) Armand, G.; Lapujoulade, J.; Lejay, Y. The Debye-Waller Factor in Helium Scattering by a Crystalline Surface. *Surface Science* **1977**, *63*, 143–152.
(194) Kim, J. W.; Kim, A. Absolute Work Function Measurement by Using Photoelectron Spectroscopy. *Current Applied Physics* **2021**, *31*, 52–59. https://doi.org/10.1016/j.cap.2021.07.018.
(195) Erbudak, M.; Gubanov, V. A.; Kurmaev, E. Z. The Electronic Structure of NbO: Theory and Experiment. *Journal of Physics and Chemistry of Solids* **1978**, *39* (11), 1157–1161. https://doi.org/10.1016/0022-3697(78)90089-6.
(196) Lo, W.-S.; Chen, H.-H.; Chien, T.-S.; Tsan, C.-C.; Fang, B.-S. OXIDATION OF Nb(001) STUDIED BY HIGH-RESOLUTION CORE-LEVEL PHOTOEMISSION. *Surf. Rev. Lett.* **1997**, *04* (04), 651–654. https://doi.org/10.1142/S0218625X9700064X.
(197) Wu, A.; Chen, L.; Chu, Q.; Guo, H.; He, Y.; Li, Y.; Pan, F.; Yang, L.; Zhang, S.; Zhao, H. Investigation on Depth Profiling of Niobium Surface Composition and Work Function of SRF Cavities. *Proceedings of the 18th Int. Conf. on RF Superconductivity* **2018**, *SRF2017*, 4 pages, 1.642 MB. https://doi.org/10.18429/JACOW-SRF2017-THPB024.
(198) Daccà, A.; Gemme, G.; Mattera, L.; Parodi, R. XPS Analysis of the Surface Composition of Niobium for Superconducting RF Cavities. *Applied Surface Science* **1998**, *126* (3), 219–230. https://doi.org/10.1016/S0169-4332(97)00790-3.
(199) Kircher, C. J. Superconducting Proximity Effect of Nb. *Phys. Rev.* **1968**, *168* (2), 437–441. https://doi.org/10.1103/PhysRev.168.437.
(200) Kim, J.; Doh, Y.-J.; Char, K.; Doh, H.; Choi, H.-Y. Proximity Effect in Nb／Au／Co Fe Trilayers. *Phys. Rev. B* **2005**, *71* (21), 214519. https://doi.org/10.1103/PhysRevB.71.214519.
(201) Chiodi, F.; Duvauchelle, J.-E.; Marcenat, C.; Débarre, D.; Lefloch, F. Proximity-Induced Superconductivity in All-Silicon Superconductor /Normal-Metal Junctions. *Phys. Rev. B* **2017**, *96* (2), 024503. https://doi.org/10.1103/PhysRevB.96.024503.
(202) Gurevich, A.; Kubo, T. Surface Impedance and Optimum Surface Resistance of a Superconductor with an Imperfect Surface. *Phys. Rev. B* **2017**, *96* (18), 184515. https://doi.org/10.1103/PhysRevB.96.184515.
(203) Belzig, W.; Wilhelm, F. K.; Bruder, C.; Schön, G.; Zaikin, A. D. Quasiclassical Green's Function Approach to Mesoscopic Superconductivity. *Superlattices and Microstructures* **1999**, *25* (5–6), 1251–1288. https://doi.org/10.1006/spmi.1999.0710.
(204) Nambu, Y. Quasi-Particles and Gauge Invariance in the Theory of Superconductivity. *Phys. Rev.* **1960**, *117* (3), 648–663. https://doi.org/10.1103/PhysRev.117.648.